

AUG 08 2005

REPORT DOCUMENTATION PAGE			Form Approved OMB No. 0704-0188	
Public reporting burden for this collection of information is estimated to average 1 hour per response, including the time for reviewing instructions, searching existing data sources, gathering and maintaining the data needed, and completing and reviewing the collection of information. Send comments regarding this burden estimate or any other aspect of this collection of information, including suggestions for reducing this burden, to Washington Headquarters Services, Directorate for Information Operations and Reports, 1215 Jefferson Davis Highway, Suite 1204, Arlington, VA 22202-4302, and to the Office of Management and Budget, Paperwork Reduction Project (0704-0188), Washington, DC 20503.				
1. AGENCY USE ONLY (Leave blank)	2. REPORT DATE 5.Aug.05	3. REPORT TYPE AND DATES COVERED DISSERTATION		
4. TITLE AND SUBTITLE CORRECTING FOR PRECIPITATION EFFECTS IN SATELLITE-BASED PASSIVE MICROWAVE TROPICAL CYCLONE INTENSITY ESTIMATES.			5. FUNDING NUMBERS	
6. AUTHOR(S) CAPT WACKER ROBERT S				
7. PERFORMING ORGANIZATION NAME(S) AND ADDRESS(ES) UNIVERSITY OF WISCONSIN MADISON			8. PERFORMING ORGANIZATION REPORT NUMBER  CI04-1153	
9. SPONSORING/MONITORING AGENCY NAME(S) AND ADDRESS(ES) THE DEPARTMENT OF THE AIR FORCE AFIT/CIA, BLDG 125 2950 P STREET WPAFB OH 45433			10. SPONSORING/MONITORING AGENCY REPORT NUMBER	
11. SUPPLEMENTARY NOTES				
12a. DISTRIBUTION AVAILABILITY STATEMENT Unlimited distribution In Accordance With AFI 35-205/AFIT Sup 1			12b. DISTRIBUTION CODE	
13. ABSTRACT (Maximum 200 words)				
<b>DISTRIBUTION STATEMENT A</b> Approved for Public Release Distribution Unlimited				
14. SUBJECT TERMS			15. NUMBER OF PAGES 146	
			16. PRICE CODE	
17. SECURITY CLASSIFICATION OF REPORT	18. SECURITY CLASSIFICATION OF THIS PAGE	19. SECURITY CLASSIFICATION OF ABSTRACT	20. LIMITATION OF ABSTRACT	

**CORRECTING FOR PRECIPITATION EFFECTS IN SATELLITE-BASED  
PASSIVE MICROWAVE TROPICAL CYCLONE INTENSITY ESTIMATES**

by

Robert S. Wacker

A dissertation submitted in partial fulfillment of the  
requirements for the degree of

Doctor of Philosophy

(Atmospheric and Oceanic Sciences)

at the

UNIVERSITY OF WISCONSIN-MADISON

2005

20050815 048

**Abstract**

Accurate tropical cyclone (TC) intensity estimates are best achieved from satellite observations. The Advanced Microwave Sounding Unit (AMSU) has operated since 1998 on polar-orbiting environmental satellites and is able to measure the warm temperature anomaly in the upper troposphere above a TC's center. Through hydrostatic equilibrium, this warm anomaly is roughly proportional to the TC's sea-level pressure anomaly. Based on this principle, the Cooperative Institute for Meteorological Satellite Studies (CIMSS) provides near real-time AMSU-based estimates of TC minimum sea-level pressure (MSLP) to forecast centers worldwide. These estimates are as accurate as the benchmark Dvorak technique, but are subject to error caused by precipitation effects (primarily brightness temperature reduction by scattering) on the AMSU 55 GHz channels sensitive to upper-tropospheric temperature.

Simulated AMSU brightness temperatures (TB's) are produced by a polarized reverse Monte Carlo radiative transfer model using representative TC precipitation profiles. Results suggest that precipitation depression of high-frequency window channel TB's is correlated with depression of sounding channel TB's and can be used to correct for scattering effects on the AMSU channels used in TC intensity estimates. Analysis of AMSU data over the tropical oceans confirms this, and forms the basis for an empirical scattering correction using AMSU 31 and 89 GHz TB's. This scattering correction reduces CIMSS TC MSLP algorithm RMS error by 10% in a 7-year, 497 observation sample.

## Abstract

Accurate tropical cyclone (TC) intensity estimates are best achieved from satellite observations. The Advanced Microwave Sounding Unit (AMSU) has operated since 1998 on polar-orbiting environmental satellites and is able to measure the warm temperature anomaly in the upper troposphere above a TC's center. Through hydrostatic equilibrium, this warm anomaly is roughly proportional to the TC's sea-level pressure anomaly. Based on this principle, the Cooperative Institute for Meteorological Satellite Studies (CIMSS) provides near real-time AMSU-based estimates of TC minimum sea-level pressure (MSLP) to forecast centers worldwide. These estimates are as accurate as the benchmark Dvorak technique, but are subject to error caused by precipitation effects (primarily brightness temperature reduction by scattering) on the AMSU 55 GHz channels sensitive to upper-tropospheric temperature.

Simulated AMSU brightness temperatures (TB's) are produced by a polarized reverse Monte Carlo radiative transfer model using representative TC precipitation profiles. Results suggest that precipitation depression of high-frequency window channel TB's is correlated with depression of sounding channel TB's and can be used to correct for scattering effects on the AMSU channels used in TC intensity estimates. Analysis of AMSU data over the tropical oceans confirms this, and forms the basis for an empirical scattering correction using AMSU 31 and 89 GHz TB's. This scattering correction reduces CIMSS TC MSLP algorithm RMS error by 10% in a 7-year, 497 observation sample.

## Acknowledgments

No significant task can be accomplished alone, and I am deeply indebted to the people who made this work, and all I learned from it, possible.

Five organizations enabled me to attend graduate school: First, the Fannie and John Hertz Foundation provided me a fellowship for graduate studies, and was gracious to grant me a leave of absence to accommodate my commitment to the Air Force. Second, I appreciate the U.S. Air Force Academy Physics Department selecting me to attend graduate school and join the faculty; I am especially grateful to Maj. Kurt Brueske, who alerted me to the opportunity. I thank the Cooperative Institute for Meteorological Satellite Studies and the UW-Madison Atmospheric and Oceanic Sciences Department for accepting me as a student. Finally, the Office of Naval Research funds the CIMSS' tropical cyclone research project within which I have worked these past three years. I hope my future efforts are worthy of the faith all these organizations have placed in me.

As I've discovered in previous Air Force assignments, the greatest satisfaction comes not from the work itself, but in whose company it's done. It's been a privilege working with CIMSS' Tropical Cyclone Research Group, the other CIMSS and AOS graduate students, and the Air Force ROTC staff members and cadets here at UW.

I'm indebted to a number of individuals for technical assistance with this work. Maj. Rich Henning, of the Air Force Reserve's 53rd Weather Reconnaissance Squadron, supplied the bulk of the aircraft reconnaissance data I used in Chapter 6. Jason Otkin and Derek Posselt of CIMSS supplied output from their Hurricane Bonnie Mesoscale Model 5 simulation, which I

used in Chapter 4. Finally, as the "owner" of CIMSS' operational tropical cyclone intensity estimation algorithm, Derrick Herndon was a constant source of technical guidance and ideas.

I owe my committee members a debt of thanks for their encouragement, guidance, and feedback on my work. Most especially, I thank my committee chair, Prof. Grant Petty, for his willingness to discuss my work frequently and at length, despite enormous demands--frequent overseas travel and publishing a textbook chief among them--on his time. Likewise, I appreciate the guidance of Chris Velden, leader of the CIMSS Tropical Cyclone Research Group, and the guiding force behind all of this work.

Quite simply, I owe all of my success in life to my family. Each day I grow more thankful to my parents, ██████████ for their lifetime of love, guidance, discipline, and encouragement. ██████████ proved that at some point, little brothers can start showing their big brothers the way. The work in this dissertation pales in comparison to the quality--and importance--of the work in his. I'll always remember the devotion to faith and family of my grandfathers, ██████████ both of whom were called home near the end of this project. My two young sons, ██████████ show me each day that no matter how much we think we know, there is always much more to learn. They are a constant reminder of what is *truly* important. And finally, I am grateful to my loving wife, ██████████ who cheerfully tackles the difficult roles of mother and military spouse, all while living far from her native Okinawa. Thank you for "sticking with" me each day. *Anata no ai suru wa domo arigatou gozaimasu. Honto ni aishite imasu.*

The views expressed in this article are those of the author and do not reflect the official policy or position of the U.S. Air Force, Department of Defense, or the U.S. Government.

## Table of Contents

Abstract.....	i
Acknowledgments.....	ii
List of Figures.....	vii
List of Tables.....	xi
1. Introduction.....	1
2. Background.....	9
2.1. The Tropical Cyclone Warm Core.....	9
2.2. Microwave Radiative Transfer Overview.....	15
2.3. Previous Microwave Sounding Instruments and TC Intensity Techniques.....	25
2.4. The Advanced Microwave Sounding Unit.....	31
3. Precipitation Effects in the Microwave Spectrum.....	35
3.1. Mie Theory.....	35
3.2. Previous Microwave Precipitation Studies.....	45
3.3. A 1-d Conceptual Model for Precipitation Effects on AMSU Brightness Temperatures.....	51
3.4. Summary.....	59
4. Simulations of Precipitation Effects on AMSU-A and -B Channels.....	62
4.1. Model.....	63
4.2. Data and Methodology.....	64
4.3. Results.....	74
4.4. Discussion.....	84
5. Developing an Empirical Scattering Correction.....	85
5.1. Data and Methodology.....	86

5.1.1. AMSU-B to AMSU-A Convolution .....	87
5.1.2. Limb Correction.....	88
5.2. Results.....	91
5.3. Discussion.....	109
6. A Precipitation Correction for the CIMSS AMSU-based TC Intensity Estimation Algorithm .....	110
6.1. The Current CIMSS Operational TC Intensity Algorithm .....	110
6.2. Precipitation Correction Methodology .....	113
6.3. Validation data set.....	113
6.4. Cleaner TB7 or TB8 vs. MSLP Relationship from Scattering Correction .....	115
6.5. CIMSS Algorithm Performance Improvement.....	116
6.5. Another Approach Enabled by Scattering Correction .....	119
6.6. Discussion .....	120
7. Conclusions and Future Work .....	121
7.1. Summary .....	122
7.2. Future Work: Adaptation to SSMIS .....	125
Appendix: A Polarized Reverse Monte Carlo Radiative Transfer Model .....	128
A.1. Motivation.....	128
A.2. Previous Monte Carlo Models .....	129
A.3. Key Assumptions and Approximations .....	131
A.4. Methodology .....	133
A.4.1. Meteorological Profile Generation.....	133
A.4.2. Mie Property Generation.....	134
A.4.3. Extinction Profile Generation .....	135

A.4.4. Phase Function Generation .....	135
A.4.5. Reverse Monte Carlo Radiative Transfer.....	137
A.5. Future Work.....	137
References.....	139

## List of Figures

1.1. Comparison of TC track and intensity forecast accuracy trends .....	2
2.1. Radial-vertical cross-section of TC tangential wind.....	11
2.2. The TC secondary circulation.....	12
2.3. Schematic TC eye and eyewall circulation.....	13
2.4. Vertical cross-section of temperature anomaly for Hurricane Cleo, 18 Aug 1958 .....	13
2.5. Air density, optical depth, transmittance, and weighting function for an example atmosphere .....	20
2.6. Microwave transmittance spectrum .....	22
2.7. Surface reflectivity and emissivity.....	23
2.8. Radial-vertical cross-section of composite typhoon and AMSU-A weighting functions at nadir and edge of scan .....	26
2.9. SCAMS 55.45 GHz <i>T<sub>B</sub></i> anomaly observed by Kidder et al. (1978) for Typhoon June and MSLP vs. SCAMS 55.45 GHz <i>T<sub>B</sub></i> anomaly.....	27
2.10. 250 hPa retrieved temperature field and $T_{250}$ Laplacian vs. <i>MSLP</i> .....	28
2.11. AMSU-A raw and retrieved anomaly vs. <i>MSLP</i> for the Atlantic and Eastern Pacific basins for the 2000 TC season.....	28
2.12. AMSU-A radial <i>T<sub>B</sub></i> gradient by channel and estimated vs. aircraft-reconnaissance measured $V_{max}$ .....	29
2.13. Non-corrected vs. scattering-corrected temperature anomaly, surface pressure, and tangential wind .....	30
2.14. NOAA-KLM series polar-orbiting spacecraft .....	31
2.15. AMSU-A temperature sounding weighting functions at near-nadir and edge of scan .....	33
3.1. Mie properties for liquid water, ice, graupel, and melting graupel at 23.8 GHz (AMSU-A channel 1).....	37
3.2. Same as Figure 3.1., but for 183.31 GHz (AMSU-B channels 18-20).....	38
3.3. Complex indices of refraction across the microwave spectrum for pure liquid, pure ice, melting graupel, and low-density graupel .....	38

3.4. Extinction coefficient, single-scatter albedo, and asymmetry parameter for various rain precipitation densities.....	43
3.5. Same as Figure 3.4., but for snow.....	43
3.6. Same as Figures 3.4 and 3.5, but for graupel.....	44
3.7. Geometry of the 1-D plane-parallel conceptual model for hydrometeor effects on AMSU window and sounding channel <i>TB</i> 's.....	52
3.8. Modeled <i>TB89</i> and <i>TB150</i> vs. <i>TB31</i> .....	58
3.9. Modeled <i>TB55</i> depression vs. <i>TB89</i> and <i>TB150</i> depression for the 10 cases summarized in Table 3.1. ....	59
4.1. Meteorological profiles and window channel weighting functions for simulation case 4 ...	67
4.2. Same as Figure 4.1., but for case 8 .....	68
4.3. Same as Figure 4.1., but for case 9 .....	68
4.4. Column integrated cloud liquid water, rain, and graupel for MM5 simulation of Hurricane Bonnie at 1200 UTC 25 Aug 1998 and 1200 UTC 26 Aug 1998.....	71
4.5. Same as Figure 4.1., but for case 11 .....	72
4.6. Same as Figure 4.1., but for case 15 .....	73
4.7. Simulated AMSU-A and -B high-frequency window channel vs. AMSU-A low-frequency window channel <i>TB</i> 's.....	75
4.8. Simulated AMSU-B moisture channel vs. AMSU-A low frequency window channel <i>TB</i> 's.....	76
4.9. Correlation between high-frequency window/moisture channel scattering <i>TB</i> depression and temperature sounding channel scattering <i>TB</i> depression .....	79
4.10. Simulated sounding channel scattering <i>TB</i> depression vs. window channel scattering <i>TB</i> depression.....	80
4.11. Simulated sounding channel scattering <i>TB</i> depression vs. moisture channel scattering <i>TB</i> depression.....	81
4.12. Leading EOF of simulated window and moisture channel $\Delta TB$ .....	83
4.13. Simulated sounding channel $\Delta TB$ vs. the leading principal component of window/moisture channel $\Delta TB$ .....	83

5.1. AMSU-A window channel brightness temperatures from NOAA-16 on 01 Jan 03 .....	90
5.2. AMSU-A temperature sounding channels, NOAA-16, 01 Jan 03 .....	92
5.3. AMSU-B window channels convolved to AMSU-A resolution, NOAA-16, 01 Jan 03 .....	93
5.4. AMSU-B moisture sounding channels convolved to AMSU-A resolution, NOAA-16, 01 Jan 03.....	94
5.5. AMSU-A <i>TB15</i> and AMSU-B <i>TB17</i> through <i>TB20</i> vs. AMSU-A <i>TB2</i> for all tropical ocean scenes .....	96
5.6. Same as Figure 5.5., but for 2003 Atlantic TC scenes.....	97
5.7: Limb-corrected <i>TB8</i> and <i>TB7</i> vs. <i>TB15</i> scattering depression and <i>TB19</i> scattering depression.....	99
5.8. Sounding channel $\Delta TB$ vs. $\Delta TB15$ and $\Delta TB19$ for 2003 Atlantic TC scenes .....	100
5.9: Tropical Rainfall Measuring Mission (TRMM) Precipitation Radar (PR) cumulative reflectivity profiles. ....	102
5.10: Conceptual diagram of ambient environment modulation of sounding channel scattering <i>TB</i> depression.....	103
5.11: Hurricane Ivan 1904 UTC 19 Sep 04 precipitation correction example .....	106
5.12. Channel 7 and 8 scattering correction effect on environmental TB, warm TB, and $\Delta TB$ for 497 Atlantic TC cases from 1998-2004 .....	107
5.13. Non-corrected vs. scattering-corrected <i>TB7</i> and <i>TB8</i> anomaly correlation with TC <i>MSLP</i> .....	108
6.1. CIMSS AMSU-based TC intensity estimation algorithm flowchart .....	111
6.2. Improvement in single-channel size-bias corrected <i>MSLP</i> estimates after precipitation correction is applied to AMSU <i>TB7</i> and <i>TB8</i> .....	115
6.3. Comparison of CIMSS TC intensity algorithm performance before and after precipitation correction .....	117
6.4. TC radius of maximum wind vs. <i>MSLP</i> .....	118
6.5. Precipitation correction improvement in a TC intensity estimation technique using a vertically-integrated <i>TB</i> anomaly employing channels 5-8.....	120

A.1. Example extinction coefficient and single-scatter albedo profiles for AMSU-A channel 8 for the profile from Chapter 4 case 9 .....	134
A.2. Example phase function for AMSU-A channel 2 and AMSU-B channel 18 for a model level with large graupel content .....	135
A.3. Flowchart for reverse Monte Carlo radiative transfer model.....	136

**List of Tables**

2.1. TC intensity categorization .....	9
2.2. AMSU-A and -B instrument characteristics .....	34
3.1. Modeled brightness temperatures at 31, 55, 89, and 150 GHz .....	57
4.1. Simulation cases.....	66
5.1. AMSU-A limb-corrected temperature sounding channel scattering depression correlation with window/moisture channel depression .....	99
5.2. Sounding $\Delta TB$ vs. window/moisture maximum $\Delta TB$ slope for near-TC cases and general tropical cases .....	104
5.3. Comparison of $TB7$ and $TB8$ anomaly correlation with TC $MSLP$ .....	105
6.1. Sounding channel $TB$ vs. $\Delta TB15$ precipitation correction slopes .....	113
6.2. Comparison of RMSE, average mean error, and bias of CIMSS TC intensity estimates with and without precipitation correction .....	117
6.3. Comparison of size-bias RMSE improvement on non-corrected and precipitation- corrected AMSU TC intensity estimates.....	118
6.4. RMSE, AME, and bias by TC intensity.....	119

## 1. Introduction

Tropical cyclones are among the most deadly and damaging of natural phenomena. In extreme cases, such as the Bangladesh Typhoon of 1970, they have killed 300,000 people (WMO Tropical Cyclone Programme 2000). In the Western world, timely warnings, mass communication, and efficient transportation make loss of life much smaller. However, rapid development along vulnerable coastlines has caused a different problem: exponentially increasing damage costs. Hurricane Andrew, the costliest natural disaster to strike the U.S., caused \$25 billion of damage to south Florida in 1992 (Rappaport 1993). U.S. hurricane damage in a typical year approaches \$5 billion (Pielke and Landsea 1998). Evacuation costs alone can be staggering, often estimated at near \$1 million per mile of affected coastline (Whitehead 2000).

With a large number of bases and deployed forces in the tropical Western Pacific and Indian Ocean, as well as the Southeast United States, the Department of Defense (DoD) is extremely vulnerable as well to fatalities, damage, and disrupted operations caused by TC's. To minimize the risk of damage to critical ships, aircraft, and hardware, commanders are forced to evacuate them from installations in the path of a TC, costing several hundred thousand dollars--and several days of lost training--per occurrence per installation (Dumas and Tibbetts 2004).

Because of these significant impacts, affected nations maintain TC forecast and warning centers. The U.S. National Hurricane Center (NHC) and Central Pacific Hurricane Center join counterparts from Japan, Australia, Fiji, India, and France to form the World Meteorological Organization's network of Regional Specialized Meteorological Centers (RSMC's), each having official TC warning responsibility for a portion of the tropical oceans. DoD also maintains the Joint Typhoon Warning Center (JTWC) at Pearl Harbor, Hawaii, with responsibility for timely

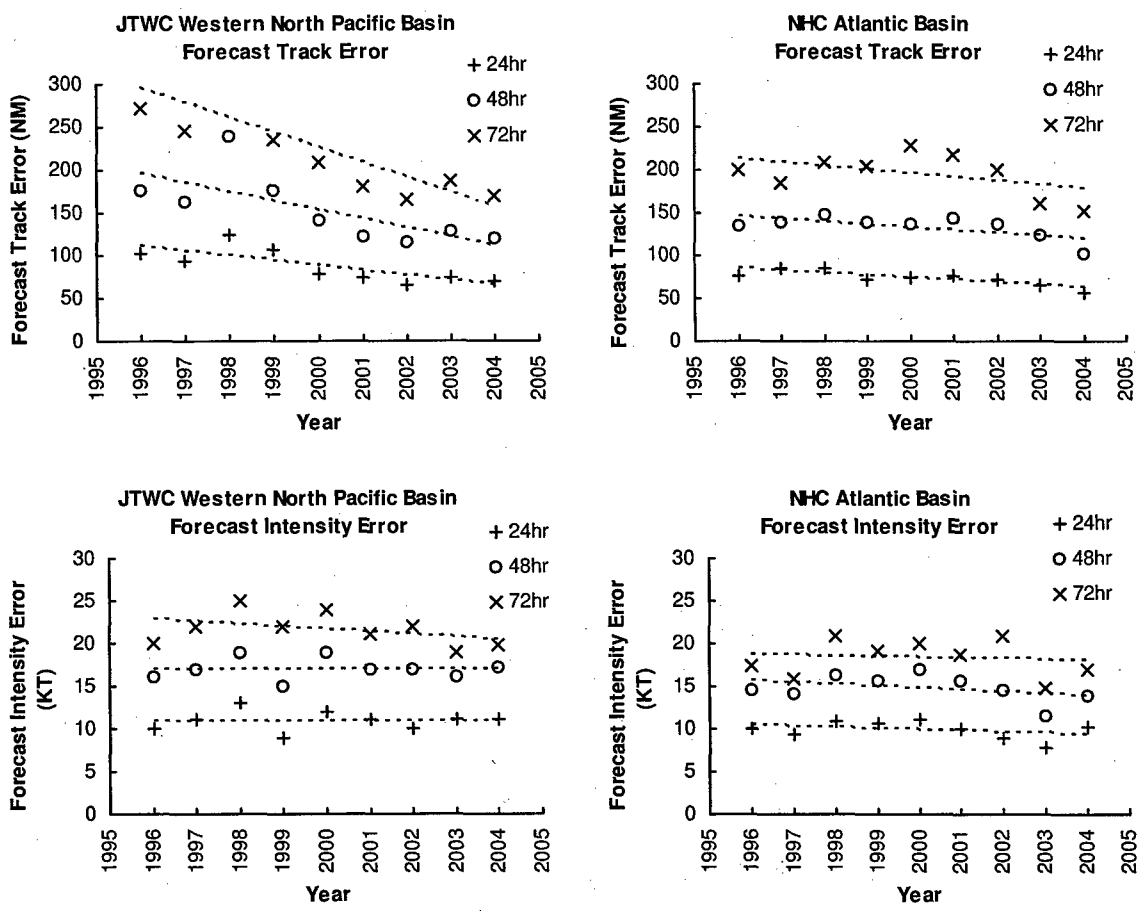


Figure 1.1: Comparison of TC track (top row) and intensity (bottom row) forecast accuracy trends. Joint Typhoon Warning Center Western North Pacific basin performance is in the left column; National Hurricane Center Atlantic basin is in the right column; 24-, 48-, and 72-hour forecast accuracies are depicted (from <http://www.nhc.noaa.gov/verification/> and <http://www.npmoc.navy.mil/jtwc/climostats/Statclimo.html>).

TC forecast and warning support to U.S. Government assets throughout the Pacific and Indian Oceans (USCINCPAC Inst 3140.1X).

Accurately predicting TC effects requires correctly forecasting storm track, maximum sustained wind speed ( $V_{max}$ ), and spatial wind distribution. Numerical weather prediction (NWP) model improvements and focused research focus have produced impressive recent gains in track forecast performance. But as shown in Figure 1.1., intensity (in the form of  $V_{max}$ ) forecast

performance has improved little over the past decade. Accordingly, research emphasis has shifted somewhat in recent years, increasing effort devoted to accurate TC intensity and wind field structure forecasts.

TC warning centers utilize a suite of NWP models, statistical aids, and empirical rules when formulating their official TC track and intensity forecasts. At present, the best intensity forecast tools are statistical, using multiple regression to predict future intensity from a selection of current TC parameters (DeMaria and Kaplan 1999; Knaff et al. 2003). For intensity forecasts out to 72 hours, the leading predictors used by the statistical models are  $V_{max}$  and its 12-hour trend. Accurate intensity forecasts, therefore, depend critically upon accurate current intensity observations.

Tropical cyclone winds are driven by the strong horizontal pressure gradient between the environment and the low pressure at the storm's center, so TC intensity can be described by either  $V_{max}$  or the minimum sea-level pressure (*MSLP*) at storm center. Neither measure is entirely satisfactory, though. A single maximum wind speed value is not representative of the highly asymmetric 3-d wind distribution caused by storm motion, shear, eddy-scale variability, and variations in storm size. While *MSLP* gives a first-order estimate of the maximum storm wind, it does not describe the fine-scale variability in the horizontal pressure *gradient*, which is responsible for the maximum sustained wind. Several attempts have been made to rectify these definitions of intensity through development of empirical wind-pressure relationships or standard radial distributions of wind and pressure (Atkinson and Holliday 1977; Holland 1980). To first-order, these relationships provide a conversion between  $V_{max}$  and *MSLP* as measures of intensity. For the purposes of this study, *MSLP* will be used for intensity, since it is more readily observed

by aircraft reconnaissance than the highly-localized  $V_{max}$ .

Forecasters and researchers use three primary means to measure *MSLP*. The most desirable is in situ measurement via aircraft reconnaissance. Since the end of World War II, the U.S. Air Force, U.S. Navy, and National Oceanographic and Atmospheric Administration (NOAA) have performed this mission in the Western North Pacific (WNP), Central Pacific (CP), Eastern Pacific (EP), and Atlantic basins (Weatherford and Gray 1988; Martin and Gray 1993). Aircraft, such as the WC-130H/J and WP-3D currently in use, have the endurance and speed to reach storms up to 1000 miles out to sea. Once there, these aircraft can loiter long enough to locate the storm's center and penetrate it multiple times, measuring wind and temperature aloft and deploying dropsondes to collect vertical profiles of wind, temperature, pressure, and humidity (Hock and Franklin 1999). Unfortunately, reconnaissance operations are currently limited to the western part of the Atlantic basin, with occasional CP and EP missions.

In the absence of reconnaissance, the only in situ wind and pressure observations come from manned or automated weather stations, ships, and buoys. Given the vast size of the tropical ocean basins, the relatively small size of a TC, and instrument uncertainty (or damage) caused by the extremely high winds and rough seas, the number of usable in situ surface observations of TC intensity is extremely small.

With the relative sparsity of in situ surface and aircraft reconnaissance observations, TC forecasters have come to rely most heavily on the third source of TC observations: weather satellites. Shortly after the introduction of operational geostationary weather satellites, Dvorak (1973; 1975) developed an empirical technique for estimating intensity using TC features in visible satellite imagery. This technique, expanded to incorporate features observed in enhanced

infrared (IR) imagery (Dvorak 1984), has become the standard for operational TC intensity estimates. It employs pattern matching, identification of maximum and minimum cloud temperatures, and measurements of the degree of spiral band curvature, along with intensity change rules and constraints to produce a current intensity on a numeric scale ranging from 0.5 to 8.0. Analysts at the RSMC's, JTWC, the NOAA National Environmental Satellite Data and Information Service Satellite Analysis Branch, and the Air Force Weather Agency use the Dvorak technique to produce operational MSLP estimates with root mean square error (RMSE) of approximately 10 hPa (Olander et al. 2004). An automated version of the Dvorak technique developed by the University of Wisconsin-Madison's Cooperative Institute for Meteorological Satellite Studies (CIMSS) achieves similar results (Olander et al. 2004). The excellent performance of both the manual and automated Dvorak techniques, combined with the excellent update frequency (hourly or half-hourly) of geostationary imagery, justifies their widespread operational use. However, the Dvorak technique has shortcomings. The manual technique is labor-intensive, requiring a highly trained and experienced satellite analyst. Its rules, combined with the ambiguities of imagery interpretation, can introduce considerable subjectivity. Dvorak's constraints on intensity change rates cause estimates to lag rapid TC intensity changes (Velden et al. 1998). Finally, empirical techniques such as this are conditioned to mean events and often perform poorly in extreme cases. A more physical and more objective remotely sensed TC intensity estimation technique would therefore complement the Dvorak techniques in operational use.

Passive and active microwave instruments on polar-orbiting weather satellites offer some alternatives. The thick cirrus cloud that often canopies the center of TC's is nearly transparent at

microwave frequencies (3 to 300 GHz). Rain emits strongly at the lower end of this frequency band, while frozen precipitation scatters strongly at the high end. This makes the convective clouds in TC spiral bands and eyewalls very distinct in imagery from passive microwave imagers like the Special Sensor Microwave Imager (SSM/I), Tropical Rainfall Measuring Mission (TRMM) Microwave Imager (TMI), and Advanced Microwave Scanning Radiometer (AMSR). This enables highly accurate TC position fixes in cases where IR imagery would have difficulties (Alliss et al. 1993). Passive microwave imagers can also infer sea surface wind speed from the increasing microwave emissivity of the wind-roughened ocean surface. Active microwave scatterometers like the SeaWinds instrument are able to do the same via ocean-surface radar reflectivity, as well as infer wind direction by observing surface reflectivity from different angles (Katsaros et al. 2001; Yueh et al. 2003). Both types of instrument can give a large-scale picture of TC wind field structure, but their relatively coarse spatial resolution and constraints on the maximum wind measurable by these techniques prevent either active radar or passive imagers from accurately estimating  $V_{max}$ , and neither type is capable of estimating *MSLP*.

Polar-orbiting passive microwave temperature sounding instruments, however, are well-suited to estimating *MSLP*. Hydrostatic equilibrium relates surface pressure to the temperature of the column of air above. From the temperature difference between columns in the ambient environment and at the TC center, we can infer the *MSLP* difference from the ambient sea-level pressure. Kidder et al. (1978) first demonstrated this principle using an experimental microwave temperature sounder. At CIMSS, Velden and Smith (1983), Velden (1989), and Velden et al. (1991) expanded on the idea using the Microwave Sounding Unit (MSU), the first-generation operational instrument. Today, both CIMSS and the Cooperative Institute for Research in the

Atmosphere (CIRA) produce real-time TC intensity estimates using the Advanced Microwave Sounding Unit (AMSU) (Brueske and Velden 2003; DeMuth et al. 2004). This type of intensity estimate is completely automated and objective and can achieve accuracies superior to operational Dvorak intensity estimates (Herndon et al. 2004). While microwave sounding instrument TC intensity estimation techniques are promising, they have their own shortcomings: The AMSU instrument is carried on NOAA Polar-orbiting Operational Environmental Satellite (POES) spacecraft. There are currently 3 operational POES spacecraft, which limits data refresh to 4-6 hours, compared to an hour or less for IR imagery from geostationary satellites. While geostationary satellites transmit instrument data to ground processing centers nearly instantaneously, polar-orbiting spacecraft store data for playback to ground stations once per orbit. Frequently, though, polar-orbiters may go 2 or 3 orbits between playbacks, making data unavailable for up to five hours after it was collected. (The National Polar-orbiting Operational Environmental Satellite System, NPOESS, plans to improve this situation by using a distributed worldwide network of ground stations when it becomes operational after 2010) The coarse instrument resolution of microwave temperature sounding instruments (AMSU-A ranges from 48 to 150 km) causes it to sub-sample the relatively small TC warm core. The effect is currently addressed at CIMSS using ancillary estimates of TC size (Herndon et al. 2004). And finally, large liquid and frozen hydrometeors in the concentrated cumulonimbus convection near storm center can scatter upwelling microwave radiation, decreasing the accuracy with which temperature sounding instruments can measure the TC's warm core magnitude and estimate its MSLP. *The purpose of this study is to foster better TC intensity forecasts by improving the accuracy of CIMSS' microwave TC intensity estimates through quantifying and correcting for*

*these precipitation effects.*

Chapter 2 of this dissertation introduces background information on the tropical cyclone warm core, passive microwave temperature sounding, existing microwave TC intensity estimation techniques, and the technical details of the AMSU-A and -B instruments. Chapter 3 discusses how precipitation affects microwave radiative transfer and introduces a conceptual framework for estimating precipitation effects on AMSU sounding channels. Chapter 4 presents results from numerical simulations of precipitation effects on AMSU sounding channels. Details of the Reverse Monte Carlo radiative transfer model developed for this purpose are contained in the Appendix. Chapter 5 analyzes AMSU observations of tropical convective precipitation and discusses an empirical method for correcting its effect on temperature sounding channels. Chapter 6 applies this correction to the CIMSS AMSU TC intensity estimation technique and validates its performance. Chapter 7 presents concluding discussion and outlines a future application.

## 2. Background

Before Chapter 3 discusses precipitation effects on microwave radiative transfer, Chapter 2 summarizes four key areas of background. Section 2.1 discusses the tropical cyclone (TC) warm core and its relation to the TC's minimum sea-level pressure (*MSLP*). Section 2.2 outlines microwave radiative transfer and temperature sounding principles. Section 2.3 reviews previous efforts to remotely sense TC *MSLP* or maximum sustained wind ( $V_{max}$ ) via the TC's warm core using microwave sounding instruments. Finally, Section 2.4 presents the detailed characteristics of the Advanced Microwave Sounding Unit (AMSU).

### 2.1. The Tropical Cyclone Warm Core

TC's are long-lived oceanic warm-core cyclonic circulations that extend vertically through the full depth of the troposphere and radially for hundreds of km. Their energy source is latent and sensible heat transferred from ocean to atmosphere by evaporation and conduction, then transported to the upper troposphere by vertical motion in organized deep convection (Emanuel 2003; Simpson et al. 1997). The weakest TC's, with sustained winds of less than 35 kt (or *MSLP* greater than about 1005 hPa) are called tropical depressions. Tropical storms have sustained winds of at least 35 kt but less than 65 kt (*MSLP* between 1005 and 987 hPa). Storms

Table 2.1: TC Intensity Categorization

	Sustained Wind (kt)	MSLP (hPa)
Tropical depression	<35	>1005
Tropical storm	35-64	987-1005
Cat 1 Hurricane	65-82	975-987
Cat 2 Hurricane	83-95	965-975
Cat 3 Hurricane	96-113	950-965
Cat 4 Hurricane	114-135	925-950
Cat 5 Hurricane	>135	<925

with sustained winds of 65 kt or greater ( $MSLP < 987$  hPa) are called--depending on ocean basin--hurricanes (Atlantic, Eastern Pacific, and Central Pacific basins), typhoons (Western North Pacific basin), or tropical cyclones (Indian Ocean and Southern Hemisphere). The Saffir-Simpson scale subdivides hurricanes into five categories according to increasing sustained wind (Table 2.1).

TC genesis is still poorly understood because of the scarcity of in situ observations of nascent storms and the difficulty in parameterizing or explicitly modeling the convective-scale processes crucial to storm formation (Ooyama 1982; Tripoli 1992). TC's occur preferentially in regions with clusters of tropical mesoscale convective systems (MCS's), such as tropical easterly waves (the most common Atlantic basin TC progenitor) or the monsoon trough (the source of most WNP TC's) (Nakayama 2001; Lander 1994).

These MCS's contain multiple organized convective cells, each of which undergoes a formative, mature, and dissipative stage (Leary and Houze 1979; Leary and Houze 1979b). Strong upward transport of latent and sensible heat characterizes the formative and mature stages. Dissipating convective cells leave behind anvil cirrus cloud where ice crystals settle, melt upon reaching the freezing level, and fall as stratiform rain. Latent heat release in the convective columns warms the upper troposphere, while subsidence in the stratiform rain beneath the anvil brings cool, dry air from the mid-troposphere down to the surface (Zipser 1969). The warming aloft and cooling near the surface stretch the air column, create a potential vorticity anomaly, and help to generate a vortex. The heat carried aloft in the convective plumes creates an environment neutrally stable with respect to moist convection. Due to the neutral stability, the Rossby radius of deformation is small in this environment, so gravity waves cannot

efficiently carry away this heat (Simpson et al. 1997). The rotation of the developing vortex also helps by confining the heat released to within a small radius near the circulation center. Through hydrostatic balance, this trapped upper-tropospheric warm air creates a radial surface pressure gradient conducive to low-level convergence.

Further development, and later, steady-state intensity, is maintained by cooperative interaction between the primary (azimuthal) and secondary (radial and vertical) circulations. The primary circulation consists of cyclonic low-level inflow and anticyclonic upper-level outflow (except near the core of the circulation, where the strong convective updrafts carry cyclonic rotation all the way to top of troposphere). The radius where the strongest cyclonic circulation

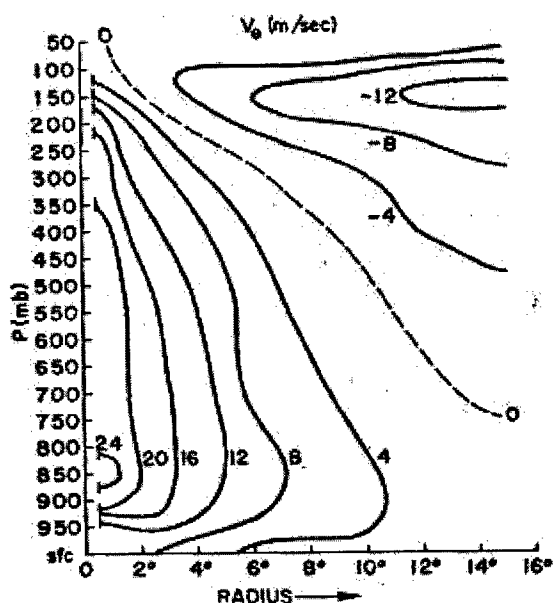


Figure 2.1: Radial-vertical cross-section of tangential wind from 18,000 composited rawinsonde observations of 248 WNP storms from 1961-1970. The cyclonic circulation increases toward smaller radii and is maximized at the top of the boundary layer, while the anticyclonic circulation increases with height and radius. From Frank (1977).

occurs is in the eyewall, the ring of convection that forms at a radius of tens of km from the circulation center. The level of strongest cyclonic circulation is near the top of the frictional boundary layer at around 850 hPa. The azimuthal circulation weakens with increasing radius due to the weakening horizontal pressure gradient. It decreases downward from the top of the boundary layer due to surface friction. It also decreases upward from the boundary layer--and eventually reverses to become anticyclonic at large radii in the upper troposphere--due to the

decreasing radial pressure gradient with increasing height (Frank 1977; Emanuel 2003). Figure 2.1 is a radial-vertical cross-section of tangential wind from a composite of WNP typhoons.

The secondary circulation flows

radially inward in the boundary layer, upward in the eyewall and convective spiral bands, and outward in the upper troposphere. The inward flow within the boundary layer is caused by frictional convergence of the cyclonic low-level primary circulation. On this leg, an air parcel's angular momentum decreases. Sensible heat flux from the ocean keeps the parcel's temperature nearly equal to the sea surface temperature, while latent heat flux, in the form of moisture evaporated from the ocean surface, increases its equivalent potential temperature,  $\theta_e$ . When the parcel reaches the eyewall (or a spiral band), convergence forces it upward (Emanuel 1988; 2003). Condensation produces prolific ( $\sim 100 \text{ mm hr}^{-1}$ ) rainfall. Upon reaching the upper troposphere, the bulk of the ascending mass turns and flows radially outward in the anticyclonic outflow. The warm outflowing parcels aloft radiate longwave infrared (IR) radiation to space, reducing their  $\theta_e$  and causing them to descend. When the subsiding parcels reach the mixed layer beneath the trade inversion, they descend moist adiabatically to the surface, where they start the cycle over again. Figure 2.2 depicts the TC secondary circulation.

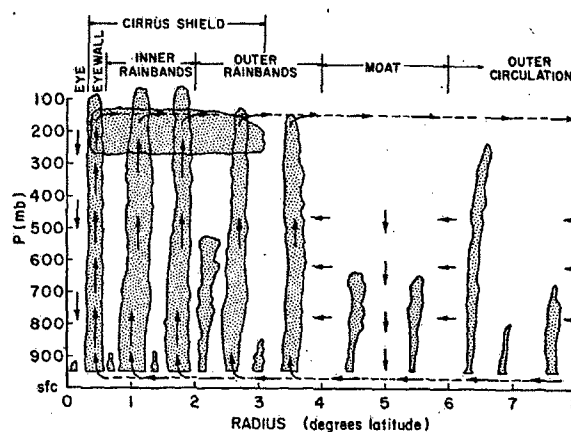


Figure 2.2: The TC secondary circulation, consisting of: 1) ascent in the eyewall and spiral band cumulus convection; 2) radial outflow where longwave IR radiation reduces  $\theta_e$ ; 3) moist adiabatic descent through the moist cloud layer; 4) radial inflow in the boundary layer where sensible and latent heat flux increase  $\theta_e$ ; and 5) forced dry descent within the eye. From Frank (1977).

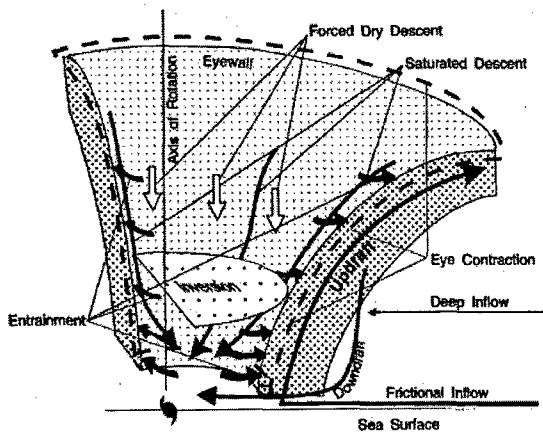


Figure 2.3: Schematic TC eye and eyewall circulation. Forced dry descent creates the TC's warm core. From Willoughby 1988.

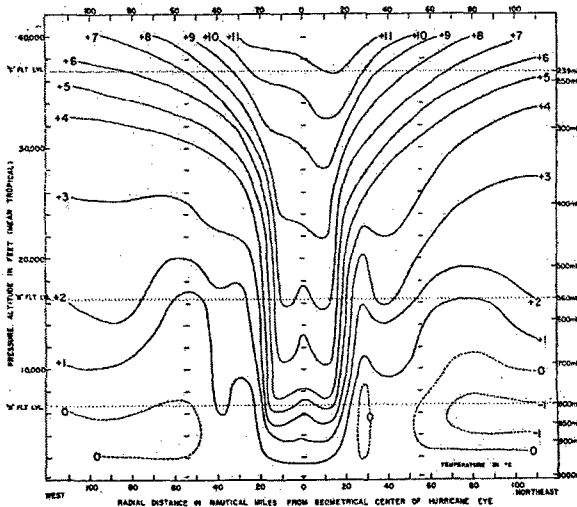


Figure 2.4: Vertical cross-section of temperature anomaly for Hurricane Cleo, 18 Aug 1958. This cross-section was measured by simultaneous penetrations by three research aircraft flying at the levels indicated by dotted lines. Cleo's MSLP was approximately 972 hPa at the time. From La Seur and Hawkins 1963.

Some of the rising air reaching the top of the upward branch of the secondary circulation is inertially confined within the eyewall, creating a convergent region in the upper troposphere above the core of the TC.

This upper-level convergence into the storm's core, in concert with entrainment of lower-level air out of the eye and into the eyewall convection, creates weak subsidence in the core. This clears the eye of clouds in upper

and mid levels and adiabatically warms the subsiding air (Willoughby 1998). Figure 2.3 is a schematic of the eyewall secondary

circulation and Figure 2.4 is a radial cross-section of the strong warming created by the adiabatic descent as observed by research aircraft penetrations of Category 2 Hurricane Cleo (1958).

Since vertical accelerations are small everywhere except in the convective updrafts, hydrostatic equilibrium (where a parcel's buoyancy balances its weight) holds and the

change in pressure over a vertical distance is the product of the local air density and gravitational acceleration:

$$\frac{dp}{dz} = -\rho g$$

Substituting for density using the ideal gas law,  $p(z) = \rho(z)RT(z)$ , and assuming a known height,  $z_{lid}$ , for a reference pressure surface,  $p_{lid}$ , we can integrate downward to determine the surface pressure,  $p_{sfc}$ . Using an average column temperature eliminates the integral:

$$\int_{p_{sfc}}^{p_{lid}} \frac{dp}{p(z)} = -\frac{g}{R} \int_0^{z_{lid}} \frac{dz}{T(z)}$$

$$p_{sfc} \approx p_{lid} \exp\left(\frac{gz_{lid}}{RT}\right)$$

If we choose a high enough  $z_{lid}$ , the height of the corresponding pressure surface,  $p_{lid}$ , will be undisturbed by the TC below and we can assume a constant  $p_{lid}$  and  $z_{lid}$  for both the TC and its environment (Kidder et al. 1978). Then we can determine the TC's *MSLP* and the environment's surface pressure  $p_{env}$  using the vertically averaged temperatures from the eye and the surrounding environment. Combining these expressions yields *MSLP* as a function of  $p_{env}$  and the TC's temperature anomaly:

$$MSLP \approx p_{lid} \exp\left(\frac{gz_{lid}}{RT_{TC}}\right), \quad p_{env} \approx p_{lid} \exp\left(\frac{gz_{lid}}{RT_{env}}\right)$$

$$MSLP \approx p_{env} \exp\left(\frac{-gz_{lid}(\overline{T_{TC}} - \overline{T_{env}})}{RT_{env} \overline{T_{TC}}}\right)$$

We can expand the exponential as a Taylor series:

$$MSLP = p_{env} \left( 1 - \frac{gz_{lid}}{RT_{env} T_{TC}} \Delta\bar{T} + \frac{\left( \frac{gz_{lid}}{RT_{env} T_{TC}} \right)^2 \Delta\bar{T}^2}{2} - \frac{\left( \frac{gz_{lid}}{RT_{env} T_{TC}} \right)^3 \Delta\bar{T}^3}{6} + \dots \right)$$

$p_{env}$  is approximately 1000 hPa,  $z_{lid}$  will be on the order of 15 km, and both the TC and environment vertically-averaged temperatures will be on the order of 250K (Velden and Smith 1983). With these scaling approximations, and assuming a maximum TC temperature anomaly on the order of 10K, the linear term of the Taylor series expansion contributes tens of hPa to the TC's *MSLP* deficit, and the quadratic term contributes on the order of 1 hPa. Higher order terms contribute negligible fractions of an hPa. So we obtain an approximate series solution for *MSLP* in terms of the TC warm core temperature anomaly:

$$MSLP \approx p_{env} - C_1 \Delta\bar{T} + C_2 \Delta\bar{T}^2$$

where

$$C_1 = p_{env} \frac{gz_{lid}}{RT_{TC} T_{env}} \approx 12 \text{ hPa K}^{-1}, \quad C_2 = \frac{p_{env}}{2} \left( \frac{gz_{lid}}{RT_{TC} T_{env}} \right)^2 \approx 5 \times 10^{-2} \text{ hPa K}^{-2}$$

## 2.2. Microwave Radiative Transfer Overview

Passive microwave radiometers, such as AMSU-A and -B, are good tools for measuring the TC warm core temperature anomaly. These instruments sense the radiation emitted by both Earth and atmosphere. Some of this radiation travels directly from the emitting source to the instrument, and at some frequencies, a significant fraction is reflected by the ocean surface, or scattered by precipitation in the atmosphere.

The fundamental quantity used in radiative transfer is radiant intensity, or radiance, the

amount of power incident on a unit surface area per interval of wavelength, traveling in a direction normal to the surface, and originating from a unit of solid angle. The units of radiance are  $W m^{-2} \mu m^{-1} sr^{-1}$  and the radiance emitted at wavelength  $\lambda$  by a blackbody at temperature  $T$  is given by the Planck function:

$$B(\lambda, T) = \frac{2hc^2}{\lambda^5 \left( \exp\left(\frac{hc}{k_B \lambda T}\right) - 1 \right)}, \quad \begin{array}{l} h = 6.626 \times 10^{-34} \text{ Js} \\ k_B = 1.381 \times 10^{-23} \text{ JK}^{-1} \\ c = 2.998 \times 10^8 \text{ ms}^{-1} \end{array}$$

The Planck radiance at all wavelengths increases with temperature and the peak of the Planck curve moves to shorter wavelengths with increasing temperature. The Planck curve for the sun, at about 6000 K, peaks in the visible portion of the spectrum, while the earth, at approximately 250 K, has a curve that peaks in the far-IR. So for terrestrial remote sensing problems in the visible and IR, the relationship between an object's temperature and its Planck radiance is highly non-linear. The microwave portion of the spectrum, occupying wavelengths between 1 mm and 10 cm (frequencies between 3 GHz and 300 GHz), is well into the long-wavelength tail of the Planck curve for emitters at terrestrial temperatures. For this part of the curve, the Rayleigh-Jeans approximation simplifies the Planck function and defines a nearly linear relationship between radiance and temperature at a given wavelength:

$$B(\lambda, T) \approx \frac{2ck_B T}{\lambda^4}$$

The brightness temperature,  $T_B$ , of a given emitter is the temperature of a blackbody emitting the same radiance. When the Rayleigh-Jeans approximation is valid, as it is in terrestrial microwave remote sensing applications,  $T_B$  can then be used interchangeably with radiance. An object's emissivity,  $\epsilon$ , is the ratio of its actual temperature to its brightness temperature, so that  $T_B = \epsilon T$ .

To understand how microwave radiation emitted by the earth and atmosphere travels upward through the atmosphere to a sensor in orbit, we begin with Beer's Law, which describes how the intensity at a given wavelength,  $I_\lambda$ , decreases as radiation travels a path between points  $s_1$  and  $s_2$  in a medium that absorbs but does not scatter:

$$I(s_2) = I(s_1) \exp\left(-\int_{s_1}^{s_2} \beta_a(s) ds\right)$$

$$\tau(s_1, s_2) = \int_{s_1}^{s_2} \beta_a(s) ds$$

$$t(s_1, s_2) = \exp(-\tau(s_1, s_2))$$

$\beta_a$  is the absorption coefficient of the medium and has units of inverse length. For an individual atmospheric constituent,  $\beta_a$  is the product of its density and its mass absorption coefficient,  $k_a$  (units of length<sup>2</sup> per mass), which is frequency-dependent. The absorption coefficient is additive, so  $\beta_a$  for a mixture of gases is the sum of all individual  $\beta_a$ 's.  $\tau(s_1, s_2)$  is the *optical thickness* between  $s_1$  and  $s_2$ , and  $t(s_1, s_2)$  is the *transmittance*, the fraction of radiation originating at  $s_1$  that reaches  $s_2$ . The *optical depth* at a height  $z$  in the atmosphere is the optical thickness from the top of the atmosphere vertically downward to  $z$ :

$$\tau(z) = \int_z^\infty \beta_a(z') dz'$$

If we define zenith angle,  $\theta$ , as the angle between vertical and the propagation direction of a beam, and further define  $\mu = \cos(\theta)$ , the transmittance between optical depth  $\tau(z)$  and the top of the atmosphere is:

$$t(z) = \exp\left(-\frac{\tau(z)}{\mu}\right)$$

While absorption will decrease a beam's intensity as it traverses a medium, thermal emission by the medium itself will add intensity (by Kirchhoff's law, absorption equals emission

in local thermodynamic equilibrium, so we can use the absorption coefficient in conjunction with the Planck function,  $B(\lambda, T)$ , to represent emission by the medium):

$$\frac{dI_\lambda}{ds} = -\beta_a(s)I_\lambda(s) + \beta_a(s)B(\lambda, T(s))$$

If we measure the optical thickness of the medium backward along the path of propagation from the sensor toward the point of emission, so that  $d\tau = -\beta_e ds$ , we can transform the radiative transfer equation from units of geometric length to units of optical thickness:

$$\frac{dI_\lambda}{d\tau} = I_\lambda(\tau) - B(\lambda, T(\tau)).$$

By multiplying each term by an integrating factor  $e^{-\tau}$  (e.g., Petty 2004) we can solve for intensity at the top of the atmosphere (TOA; where  $\tau = 0$ ) in terms of intensity originating at the surface (where  $\tau = \tau^*$ ):

$$\begin{aligned} e^{-\tau} \frac{dI_\lambda}{d\tau} &= I_\lambda(\tau)e^{-\tau} - B(\lambda, T(\tau))e^{-\tau} \\ \frac{d}{d\tau} (I_\lambda(\tau)e^{-\tau}) &= -B(\lambda, T(\tau))e^{-\tau} \\ \int_{\lambda(0)}^{\lambda(\tau^*)e^{-\tau^*}} d(I_\lambda(\tau')e^{-\tau'}) &= - \int_0^{\tau^*} B(\lambda, T(\tau'))e^{-\tau'} d\tau' \\ I_\lambda(\tau = \tau^*)e^{-\tau^*} - I_\lambda(\tau = 0) &= - \int_0^{\tau^*} B(\lambda, T(\tau'))e^{-\tau'} d\tau' \\ I_{TOA\lambda} &= I_{SFC\lambda}e^{-\tau^*} + \int_0^{\tau^*} B(\lambda, T(\tau'))e^{-\tau'} d\tau' \end{aligned}$$

Substituting transmittance,  $t = e^{-\tau}$  and  $dt = -e^{-\tau} d\tau$ , for optical depth as the vertical coordinate, and using the Rayleigh-Jeans approximation to exchange  $TB$  for  $I_\lambda$ :

$$TB_{TOA} = TB_{SFC}t^* + \int_0^{\tau^*} T(t')dt'$$

Here,  $t^*$  is the transmittance from the surface to the top of the atmosphere.

Air density decreases exponentially with altitude, with a scale height of  $H$ :

$$\rho(z) = \rho_0 \exp\left(-\frac{z}{H}\right)$$

So the transmittance from height  $z$  to the top of such an atmosphere is given by:

$$\begin{aligned}\beta_a(z) &= \rho_0 \exp\left(-\frac{z}{H}\right) k_a \\ \tau(z) &= \rho_0 k_a \int_z^\infty \exp\left(-\frac{z'}{H}\right) dz' \\ &= \rho_0 k_a H \exp\left(-\frac{z}{H}\right)\end{aligned}$$

$$t(z) = \exp\left[-\frac{\rho_0 k_a H}{\mu} \exp\left(-\frac{z}{H}\right)\right]$$

Using this expression for transmittance in an exponential atmosphere, we can transform to geometric height coordinates:

$$\begin{aligned}TB_{TOA} &= TB_{sfc} t^* + \int_0^\infty T(z) \frac{dt}{dz} dz \\ t(z) &= \exp\left[-\frac{\rho_0 k_a H}{\mu} \exp\left(-\frac{z}{H}\right)\right] \\ \frac{dt}{dz} &= \frac{\rho_0 k_a}{\mu} \exp\left[-\frac{\rho_0 k_a H}{\mu} \exp\left(-\frac{z}{H}\right) - \frac{z}{H}\right] = W(z) \\ TB_{TOA} &= TB_{sfc} t^* + \int_0^\infty T(z) W(z) dz\end{aligned}$$

Note that the surface brightness temperature,  $TB_{sfc}$ , consists not just of Planck emission from the surface itself, but also reflected downwelling atmospheric emission and cosmic background radiation. The downwelling atmospheric  $TB$  can be derived in a similar manner to the upwelling emission.

$W(z)$  is the *emission weighting function*, which describes the contribution of each layer's

temperature to the upwelling radiance at the

top of the atmosphere. Since  $W(z) = \frac{dt}{dz}$ ,

layers that contribute most to the upwelling

radiance are those where the transmittance to

the top of the atmosphere changes most

rapidly with height. In an exponential

atmosphere, the upper levels have such low

density that  $t(z)$  is near 1 and  $dt/dz = W(z) \approx 0$ .

Deeper in the atmosphere, the density may be

large enough that the atmosphere is opaque, so

$t(z)$  is near 0 and again  $dt/dz = W(z) \approx 0$ . The

layers with large  $W(z)$  are those which absorb

radiation from below, but whose own emitted radiation isn't absorbed as strongly by layers

above. Figure 2.5 depicts weighting functions for two different zenith angles at a fixed mass

absorption coefficient.

The shape of  $W(z)$  depends primarily on the mass absorption coefficient,  $k_a(\lambda)$ , and zenith angle, in the form of  $\mu$ .  $k_a(\lambda)$  has very fine-scale variability in the IR portion of the spectrum, with many intermixed vibrational transitions of  $O_2$ , water vapor (WV),  $CO_2$ ,  $O_3$ , and other constituents. Radiative transfer computations in these bands require careful handling of the multitude of overlapping bands. In the microwave, though, there are only 3 significant absorbing processes. The first is rotational absorption by molecular oxygen. This occurs for a broad band from 51-67 GHz and a narrow band at 118.75 GHz. Rotational absorption by water vapor also

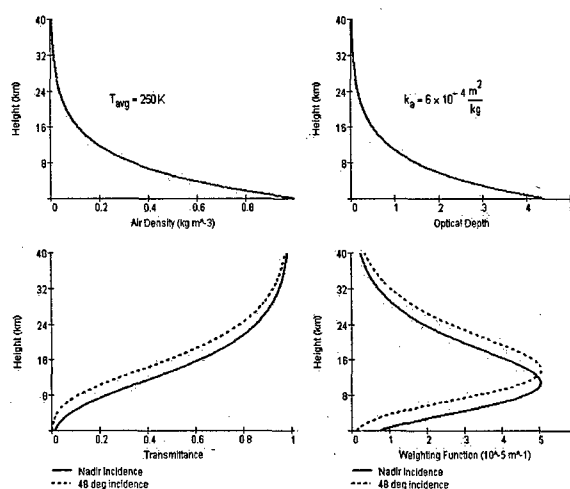


Figure 2.5: Air density (upper left), optical depth (upper right), transmittance (lower left), and weighting function (lower-right) for an atmosphere with a surface density of  $1.0 \text{ kg m}^{-3}$ , an average temperature of  $250 \text{ K}$ , and a mass absorption coefficient of  $.0006 \text{ m}^2 \text{ kg}^{-1}$ . Transmittance and weighting function are plotted for nadir incidence (solid curve) and  $48^\circ$  incidence (dashed curve).

contributes two absorption bands, a weak band at 22.24 GHz, and a strong one at 183.31 GHz (Rosenkranz 1993). The third process is continuum absorption by water vapor. The exact mechanism of WV continuum absorption is not well known, but may be caused either by the sum of overlapping tails of the multitude of pressure- and Doppler-broadened WV absorption bands from the IR spectrum, or may be caused by anomalous chains of WV molecules adhering to each other (Petty 2004). Whatever the specific mechanism, WV continuum absorption increases with increasing microwave frequency.

O<sub>2</sub> is a fixed atmospheric constituent. In the well-mixed lower and middle atmosphere, it comprises a constant 21% of air by volume. WV, on the other hand, makes up 0 to 2% of air by volume, but its concentration varies strongly in both the vertical and horizontal. The total absorption by both constituents is additive, so the net microwave absorption, particularly near the two WV rotation bands and at higher microwave frequencies where continuum absorption is strong, is dependent on the WV concentration. Figure 2.6 depicts the zenith microwave transmittance for polar, standard, and tropical atmospheres, illustrating the striking difference varying WV content can have on microwave transmittance.

Microwave sounding instruments make use of these absorption features in order to sample the vertical temperature and moisture profile. On the fringes of the O<sub>2</sub> and WV absorption bands,  $k_a$ --and therefore  $t(z)$ --change rapidly with frequency. Thus the weighting functions,  $W(z)$ , for frequencies on the edges of these bands will peak progressively higher in the atmosphere as frequency approaches the central frequency of the absorption band. Temperature sounding instruments typically use the 60 GHz O<sub>2</sub> band--with several channels closely spaced between 50-58 GHz--while moisture sounding instruments use the 183 GHz WV band. As

shown in Figure 2.6, the width and strength of the WV bands are strongly modulated by atmospheric WV concentration, so the shape of near-183 GHz weighting functions will depend strongly on humidity. More moisture decreases transmittance and causes  $W(z)$  to peak higher.

Transmittance depends on path length through the absorbing medium, so as scan angle increases away from nadir and the slant path through the atmosphere increases with it, transmittance will decrease and  $W(z)$  will peak higher. This effect, limb-darkening, can cause brightness temperatures to drop by as much as 10 K from nadir to a scan angle of  $45^\circ$ . For

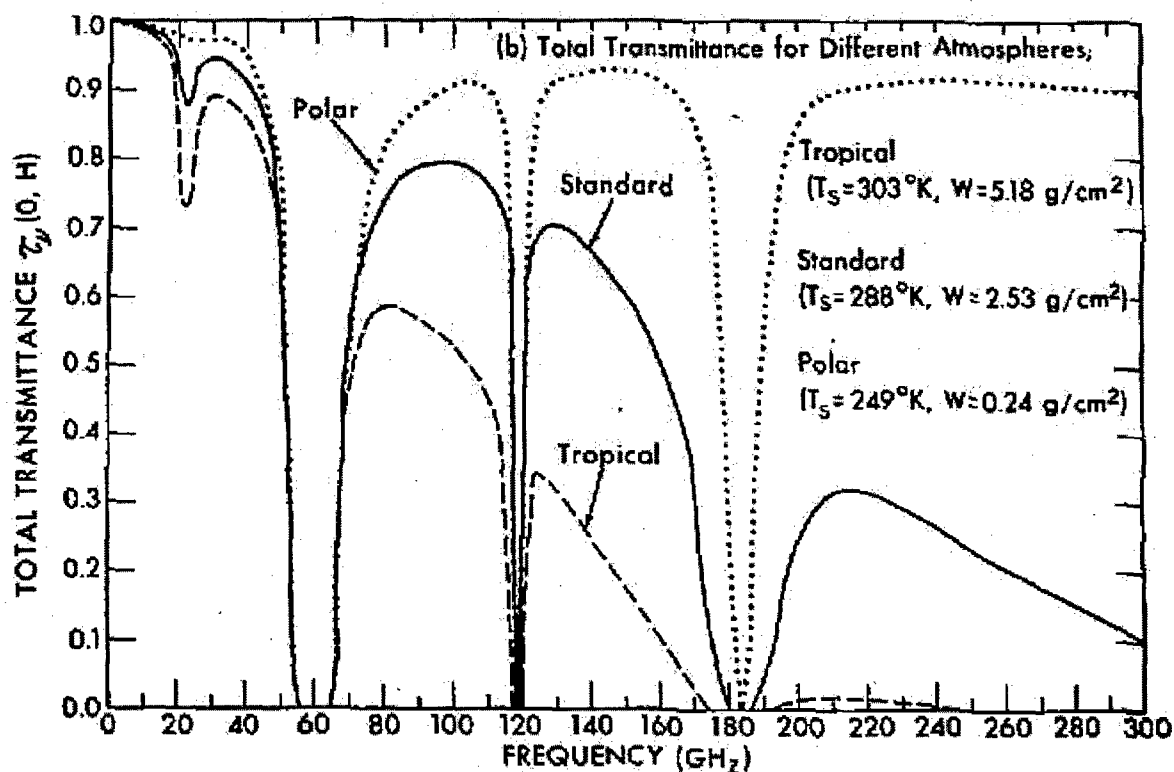


Figure 2.6: Microwave transmittance spectrum under varying water vapor concentrations. The 60 and 118 GHz  $\text{O}_2$  rotation bands are unchanged, due to the fixed  $\text{O}_2$  concentration. The weak 22 GHz and strong 183 GHz WV rotation bands, increase in intensity as WV increases. Most significant, though, is the marked increase in continuum absorption, which makes the atmosphere nearly opaque to frequencies above 170 GHz in the tropical atmosphere. From Grody (1976).

frequencies whose weighting functions contain a significant contribution from the stratosphere (where temperature increases with height) the limb effect *increases TB* instead.

At frequencies where the atmosphere has high transmittance, such as the "window" regions below 22 GHz, between 22 GHz and 50 GHz, between 70 GHz and 110 GHz, and between 125 GHz and 170 GHz, a downward looking instrument will be able to see through the (mostly) transparent atmosphere and will sense the upwelling brightness temperature from the surface. This has 3 components: thermal emission by the surface itself, reflected downward emission from the atmosphere, and reflected cosmic background radiation. The cosmic background emits at a blackbody temperature of 2.7 K, so for most purposes, it can be ignored compared with terrestrial emission sources, which all have blackbody temperatures of 100-300

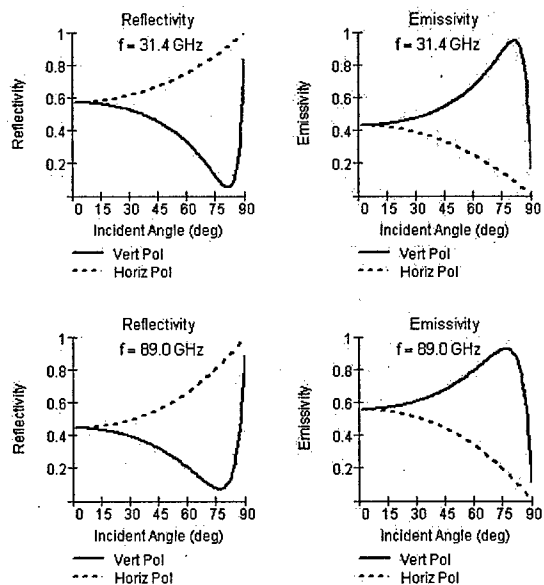


Figure 2.7: Surface reflectivity (left column) and emissivity (right column) for 31.4 GHz and 89.0 GHz window frequencies. Solid line is for vertical polarization; dashed line is for horizontal.

K. The downward atmospheric emission is computed in a manner identical to upward emission, but the weighting function in this case is computed by integrating upward from the surface to  $z$  instead of downward from TOA to  $z$ .

The reflection of downward atmospheric emission, thermal emission by the surface, and scattering by precipitation (discussed in Ch. 3) bring polarization into play for microwave remote sensing. At these frequencies, ocean surface emissivity is greater

for vertically-polarized radiation than for horizontal, so for window channels that can see to the surface, the observed *TB* will be polarized. The degree of polarization of sea-surface emission depends on scan angle, since the vertically- and horizontally-polarized emissivities have different scan-angle dependences. Vertically-polarized emissivity increases from its nadir value to a maximum at the Brewster angle, then decreases to 0 at 90° incidence, while horizontally-polarized emissivity decreases smoothly from its maximum at nadir (where  $\epsilon_h = \epsilon_v$ ) to 0 at 90° incidence. Both vertically- and horizontally-polarized emissivity increase with increasing frequency. Figure 2.7 depicts ocean surface emissivity,  $\epsilon$ , and reflectivity,  $r$ . By Kirchhoff's Law,  $r = 1 - \epsilon$ . The surface emissivity for window frequencies at scan angles of  $< 45^\circ$  ranges from around 0.45 to 0.75, so for clear scenes, the ocean surface brightness temperature will range from about 150 K to 225 K. Microwave land surface emissivity varies with vegetation type and soil moisture, but in general is much higher, and less polarized, than ocean-surface emissivity. Typical land *TB*'s are around 280 K.

Retrieving atmospheric temperature profiles from multi-channel microwave *TB*'s can be done statistically or physically. The statistical approach uses a large database of co-located rawinsonde and microwave observations segregated by latitude, surface type, and time of year. Regression analysis produces matrices containing coefficients relating each microwave *TB* to the temperature at each desired atmospheric level (Grody 1993; Goldberg 1999; Reale 2001). The physical approach is a data assimilation problem. A radiative transfer model (the forward model) predicts the expected TOA *TB*'s resulting from a first-guess temperature profile obtained from climatology or a numerical weather prediction model forecast. The temperature profile is iteratively adjusted using adjoint techniques to minimize a cost function, which quantifies both

the deviation of the derived profile from the first-guess and the discrepancy between predicted and observed *TB*'s (Chahine 1970; Smith 1970; Rodgers 1976).

### **2.3. Previous Microwave Sounding Instruments and TC Intensity Techniques**

Polar-orbiting passive microwave temperature sounding instruments have been in use for over three decades. The earliest, the Nimbus Experimental Microwave Spectrometer (NEMS), flew on the Nimbus-5 research mission in 1972. It sampled a single 200 km nadir-looking spot at three temperature sounding channels (53.65, 54.90, and 58.80 GHz). The Scanning Microwave Spectrometer (SCAMS) flew experimentally on Nimbus-6, launched in 1975. SCAMS sampled two window frequencies (22.235 and 31.65 GHz) and 3 temperature sounding frequencies (52.85, 53.85, and 55.45 GHz) in 13 fields of view (FOV) across each cross-track scan line, with resolution ranging from 145 km to 360 km. The first operational temperature sounder was the Microwave Sounding Unit (MSU), nine copies of which flew on NOAA-6, launched in 1979, through NOAA-14, whose instrument is still operational today. MSU employed 4 temperature sounding channels (50.30, 53.74, 54.96, and 57.95 GHz) with cross-track resolution ranging from 110 km to 270 km. The Special Sensor Microwave Temperature (SSMT) instrument, a contemporary of--and very similar to--the MSU, also flew on the Defense Meteorological Satellite Program (DMSP) polar-orbiting constellation beginning in 1979. The current generation sounding instrument is the Advanced Microwave Sounding Unit (AMSU), which first flew on NOAA-15 in 1998. A detailed discussion of the AMSU-A and -B instruments is contained in Section 2.4. Future MW temperature sounding instruments include the Special Sensor Microwave Imager/Sounder (SSMIS; more detailed discussion in Chapter 7),

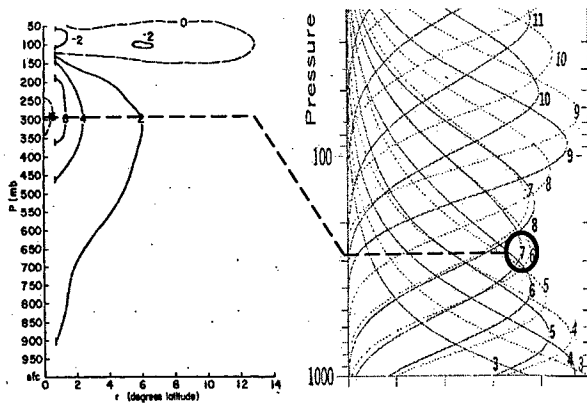


Figure 2.8: Radial-vertical cross-section (left) of composite typhoon from Frank (1977). AMSU-A weighting functions (right) at nadir (solid) and edge of scan (dashed) from Goldberg et al. (2001). AMSU-A Channel 7 matches most closely the level (approximately 300 hPa) where the TC warm anomaly is largest.

first launched on DMSP F16 in late 2003, but not yet operational, and the Conically-Scanning Microwave Imager/Sounder (CMIS), to fly on the National Polar-orbiting Operational Environmental Satellite System (NPOESS) constellation beginning around 2010.

As discussed in Section 2.1, the TC warm anomaly is strongest in the upper troposphere. Based on the microwave temperature sounding considerations in

Section 2.2, we expect microwave frequencies near 55 GHz to have weighting functions that peak near this level, as shown in Figure 2.8. Each generation of sounding instrument since SCAMS has included at least one channel near this frequency, affording maximum sensitivity to the TC warm core, and making them useful for estimating *MSLP* via the TC warm anomaly. Section 2.3 briefly discusses these previous efforts.

Kidder et al. (1978) were the first to estimate TC intensity using a microwave sounder. They derived a linear *MSLP* vs. *TB* anomaly relationship for an upper-tropospheric sounding channel (55.45 GHz), and obtained root mean square error of 15 hPa (Figure 2.9) for a set of 36 Western North Pacific TC observations. In a later paper (1980), the same authors derived similar relations for the radii of 30 kt and 50 kt sustained winds using *TB* gradients. They noted that poor spatial resolution and large instrument noise created the bulk of estimate uncertainty, but

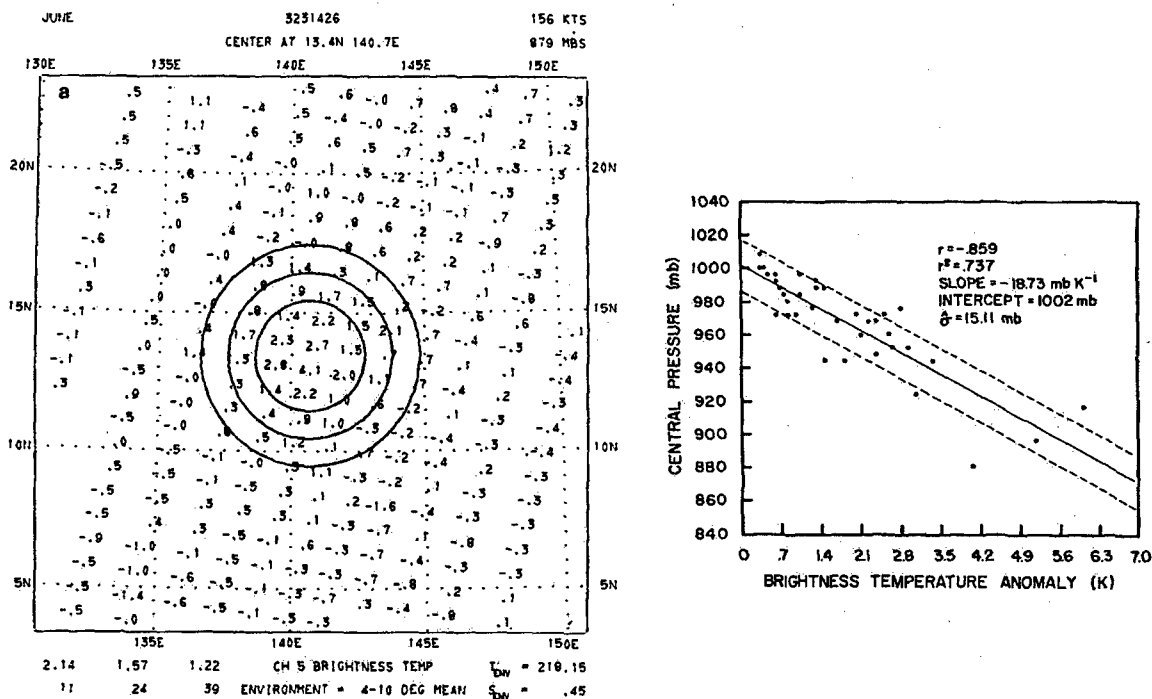


Figure 2.9: SCAMS 55.45 GHz TB anomaly observed by Kidder et al. (1978) for Typhoon June at 1426 UTC on 19 Nov 1975 (left) and MSLP vs. SCAMS 55.45 GHz TB anomaly (right).

also speculated that hydrometeor scattering might be a source of uncertainty.

Velden (1982), Velden and Smith (1983), and Velden et al. (1984) developed a similar technique using the Laplacian of the 250 hPa retrieved temperature field from the MSU. They placed more emphasis on precipitation scattering as a source of uncertainty, and manually edited fields-of-view (FOV) which were obviously affected (Figure 2.10). In subsequent studies, Velden (1989) and Velden et al. (1991) achieved RMSE of 8 and 14 hPa in the Atlantic and Northwest Pacific basins, respectively.

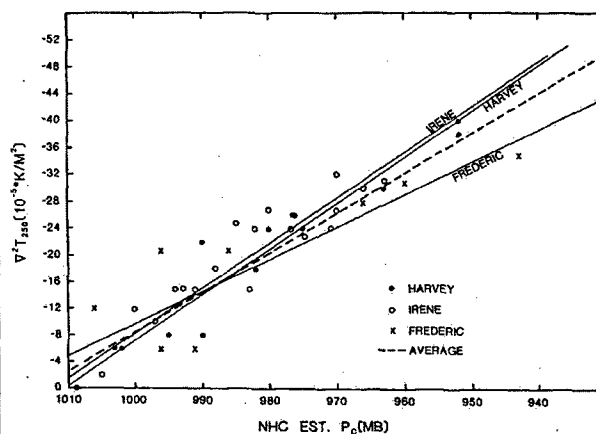
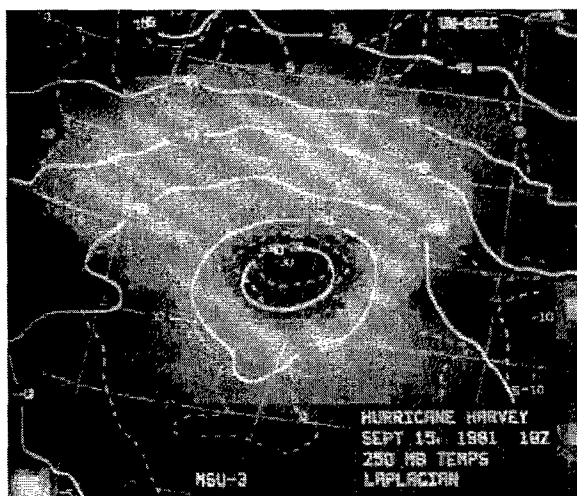


Figure 2.10: 250 hPa retrieved temperature field observed by Velden and Smith (1983) for Hurricane Harvey at 1800UTC on 15 Sep 1981 (left). Note the fields of view near storm center manually removed due to precipitation attenuation.  $T_{250}$  Laplacian vs.  $MSLP$  (right).

A significant leap in instrument capability came in 1998 with the launch of the first AMSU-A and -B suite on NOAA-15. Brueske (2001) and Brueske and Velden (2003) developed an  $MSLP$  estimation technique at CIMSS using AMSU-A channel 7 (54.94 GHz, sensitive to 250 hPa temperature)  $TB$  anomaly, along with Goldberg's (2001) correction for limb effects and Merrill's (1995; Van Burgel 1999) physically-based warm anomaly retrieval scheme. Brueske and Velden achieved 5 hPa RMSE, but for a small ( $n \approx 50$ ) sample (Figure 2.11), and established CIMSS' automated real-time intensity bulletins. Kabat (2002) added AMSU-A  $TB8$  (55.5 GHz, 150 hPa) anomaly as an intensity predictor, partly to improve performance in cases where  $TB7$  is attenuated

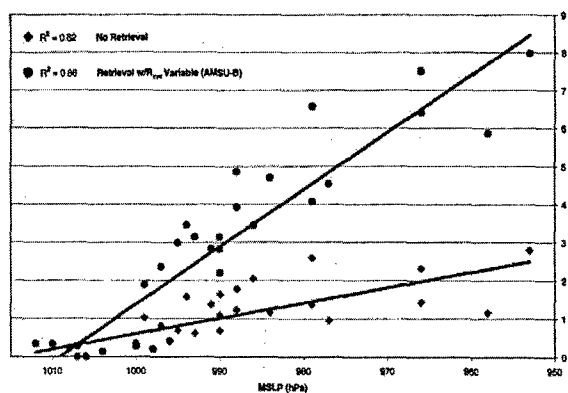


Figure 2.11: AMSU-A raw and retrieved  $TB7$  anomaly vs.  $MSLP$  for the Atlantic and East Pacific basins for the 2000 TC season (Brueske and Velden 2003).

by scattering. With the addition of corrections for sub-sampling and non-standard environmental pressure, current performance of the CIMSS AMSU-based method ranges from 6 hPa RMSE in the Atlantic to 10 hPa RMSE in the Indian Ocean (Herndon et al. 2004). *However, the CIMSS technique does not yet account for precipitation attenuation effects.*

Spencer and Braswell (2001) developed an AMSU-A  $V_{max}$  estimation technique using the radial gradient of AMSU-A TB8. They recognized the importance of hydrometeor scattering and accounted for it by including spatial gradients of both TB4 and an AMSU-A window channel scattering index (discussed in Chapter 3) among their predictors. They achieved  $5 \text{ m s}^{-1}$  (equivalent to about 10 hPa for strong storms or 5 hPa for weak storms) RMSE (Figure 2.12).

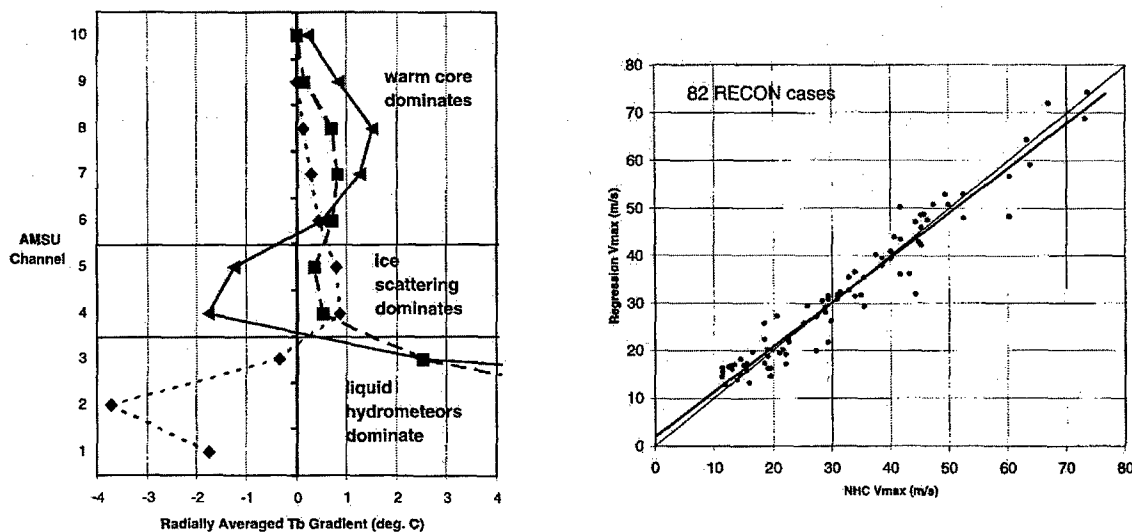


Fig. 2.12: (Left) AMSU-A radial TB gradient by channel for 3 different TC's. Positive TB gradient for TB6 through TB9 indicates the TC warm core while TB1 through TB5 are dominated by hydrometeor scattering effects. (Right) Estimated  $V_{max}$  vs. aircraft-reconnaissance measured  $V_{max}$ . From Spencer and Braswell (2001).

Zhu et al. (2002; 2004) and Demuth et al. (2004) use 3-D fields of AMSU-A retrieved temperatures to derive the corresponding 3-D pressure and wind fields using hydrostatic and gradient wind balance, with boundary conditions obtained from NWP analyses. Zhu et al. employed these temperature fields to improve NWP forecast initialization. Demuth et al. employed their fields to derive statistical TC intensity predictors, from which they produce real-time TC intensity estimates, complementing the estimates from CIMSS. Zhu et al. address precipitation effects with a physical retrieval scheme whose forward model accounts for emission and scattering. Demuth et al. use a statistical temperature retrieval, with a climatological first guess. They correct the *TB*'s used in the retrieval for precipitation effects using a two-step procedure: First, they use the linear relationship between AMSU-A cloud liquid water estimates (Weng et al. 2003) and *TB* depression to correct the instrument-resolution *TB* field. Second, they define gridded temperature fields more than 0.5 K colder than their neighbors as affected by ice

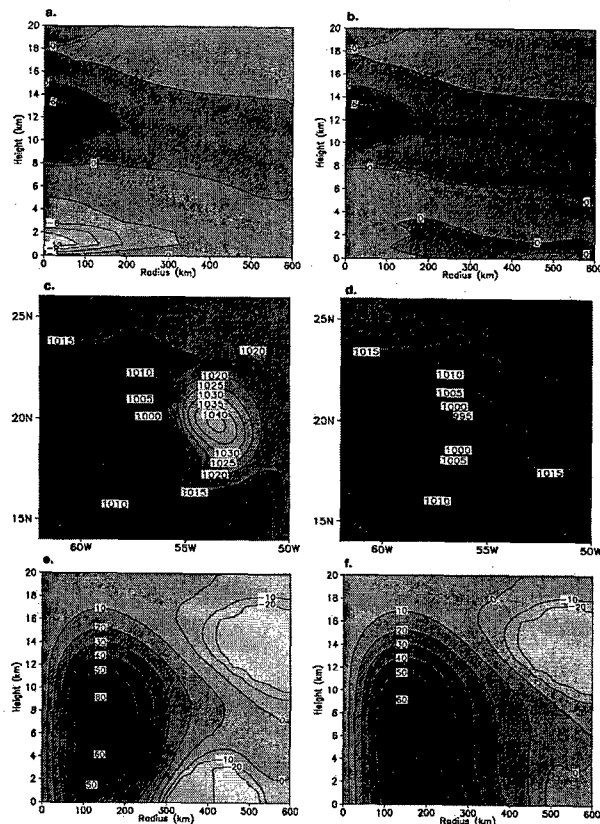


Figure 2.13: Non-scattering-corrected (left column) vs. scattering corrected (right column) radial-vertical cross-section of radially-averaged temperature anomaly (top row), surface pressure (middle row), and radial-vertical cross-section of radially-averaged tangential wind (bottom row). Anomalous cold lower-tropospheric sounding channel *TB*'s resulting from precipitation attenuation cause cold anomalies in the low-level retrieved temperature field, producing a spurious high pressure area and associated wind field perturbations. From DeMuth et al. 2004.

scattering, and correct those fields by smoothing (Figure 2.13). DeMuth et al. achieved 9 hPa RMSE.

## 2.4. The Advanced Microwave Sounding Unit

AMSU-A and -B are cross-track scanning microwave temperature and moisture sounding instruments, built to fly on the NOAA Advanced TIROS-N class of spacecraft that operate as the U.S.'s Polar-orbiting Operational Environmental Satellite (POES) constellation. Together with the High-resolution Infrared Sounder, HIRS/3, they comprise the Advanced TIROS Operational Vertical Sounder (ATOVS) system. The HIRS has finer vertical resolution, but since most clouds are opaque in the IR spectrum, it can only be used to produce temperature soundings in clear scenes. For microwave instruments like AMSU-A and -B, cirrus clouds are effectively transparent and other clouds are only weakly absorbing (discussed in more detail in Chapter 3). This enables AMSU-A to produce temperature under cloudy conditions, but with less vertical

resolution than HIRS clear soundings. The AMSU-B is used to produce humidity profiles.

AMSU-A itself consists of two separate modules. AMSU-A1 contains antennas measuring  $TB$ 's in the 50-60 GHz  $O_2$  band and the 89.0 GHz window frequency, while AMSU-A2 contains antennas for the 23.8 and 31.4 GHz window frequencies. Both AMSU-A and AMSU-B utilize parabolic

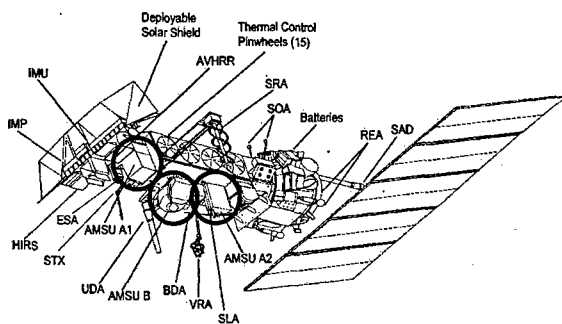


Figure 2.14: NOAA-KLM series polar-orbiting spacecraft. AMSU-A1, -A2, and -B units are circled on the Earth-facing side of the spacecraft. Image from [http://www.cira.colostate.edu/ramm/hillger/NOAA-K\\_sketch.gif](http://www.cira.colostate.edu/ramm/hillger/NOAA-K_sketch.gif).

reflectors, which are rotated  $360^\circ$  around an axis to reflect radiation into a detector. When viewing the earth, AMSU-A steps through 30 beam positions in 6 seconds, then sweeps past cold space and warm blackbody views in 2 seconds to provide cold and warm calibration limits. AMSU-B completes 3 scans for each AMSU-A scan, and sweeps continuously across the scan line, rather than stepping and staring. AMSU-A's half-power beam-width is  $3\frac{1}{3}^\circ$ , which from a nominal spacecraft altitude of 833 km, yields a nearly circular 48 km FOV for beam positions 15 and 16 ( $1\frac{2}{3}^\circ$  each side of nadir). The FOV grows to a 150 km x 80 km ellipse at beam positions 1 and 30 ( $48\frac{1}{3}^\circ$  each side of nadir). AMSU-B's half-power beam width is  $1.1^\circ$ , giving it 3 times finer horizontal resolution than AMSU-A. The total swath width of both instruments is approximately 2100 km.

The AMSU-A1, -A2, and -B detectors are sensitive to a single polarization--horizontal or vertical--but due to the rotation of their reflectors, the polarization plane of incoming radiation to which each is sensitive rotates with scan angle. The vertical polarization plane is defined by the local zenith direction and the instrument line of sight. The horizontal polarization plane is perpendicular to the vertical plane. Channels vertically-polarized (polarization angle of  $90^\circ$ ) at nadir (AMSU-A channels 1-4, 7, and 15; AMSU-B channels 16-19) have a polarization angle of  $(90^\circ - \theta)$  at scan angle  $\theta$ , while horizontally-polarized channels (AMSU-A channels 5, 6, and 8-14; AMSU-B channel 20) have a polarization angle of  $\theta$ .

The instrument measures antenna temperature, the total radiance detected by the reflector's main lobe and side lobes. This radiance includes components emitted by the earth and the cosmic background, and emitted or reflected by the spacecraft itself. Mo (1999) modeled these contributions and found they cause the antenna temperature to vary smoothly by 1-2 K

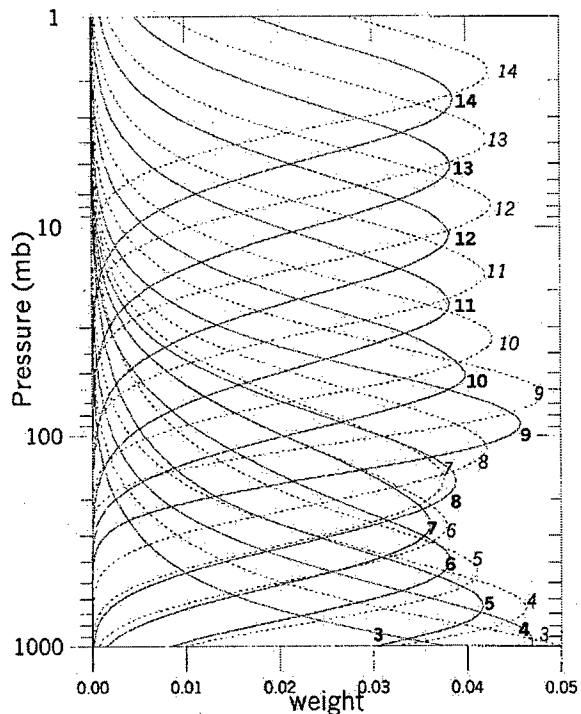


Figure 2.15: AMSU-A temperature sounding weighting functions at near-nadir (fields of view 15 and 16; solid curves) and edge of scan (fields of view 1 and 30; dashed curves). From Goldberg et al. 2001.

across the scan line. Removing the error introduced by the cold space and spacecraft contributions results in the brightness temperature.

The radiometric accuracy specification (expressed at noise-equivalent temperature uncertainty,  $NE\Delta T$ ) varies with channel, but in general becomes less stringent with increasing frequency. For AMSU-A tropospheric temperature sounding channels,  $NE\Delta T$  is 0.25

K.

Table 2.2 summarizes the frequencies, radiometric accuracy, polarizations, and primary operational application for each

AMSU-A and -B channel. Figure 2.15 depicts the weighting functions for each AMSU-A temperature sounding channel.

Table 2.2: AMSU-A and -B instrument characteristics

Channel	Frequency (GHz)	NE $\Delta$ T (K)	Pol	Application	
AMSU-A	1	23.8	.30	90° - $\theta$	Cloud liquid, precip
	2	31.4	.30	90° - $\theta$	Cloud liquid, precip
	3	50.3	.40	90° - $\theta$	Cloud liquid, precip
	4	52.8	.25	90° - $\theta$	Tropospheric (sfc) temp
	5	53.596	.25	$\theta$	Tropospheric (700 hPa) temp
	6	54.4	.25	$\theta$	Tropospheric (400 hPa) temp
	7	54.94	.25	90° - $\theta$	Tropospheric (250 hPa) temp
	8	55.5	.25	$\theta$	Tropospheric (150 hPa) temp
	9	57.290344	.25	$\theta$	
	10	57.290344 $\pm$ .217	.40	$\theta$	
	11	57.290344 $\pm$ .3222 $\pm$ .048	.40	$\theta$	Stratospheric temp
	12	57.290344 $\pm$ .3222 $\pm$ .022	.60	$\theta$	
	13	57.290344 $\pm$ .3222 $\pm$ .010	.80	$\theta$	
	14	57.290344 $\pm$ .3222 $\pm$ .0045	1.20	$\theta$	
	15	89.0	.50	90° - $\theta$	Cloud liquid, precip
AMSU-B	16	89.0	1.0	90° - $\theta$	Cloud liquid, precip
	17	150.0	1.0	90° - $\theta$	Ice scattering
	18	183.3 $\pm$ 1.0	1.1	90° - $\theta$	Upper tropospheric humidity
	19	183.3 $\pm$ 3.0	1.0	90° - $\theta$	Middle tropospheric humidity
	20	183.3 $\pm$ 7.0	1.2	$\theta$	Lower tropospheric humidity

Notes:

1. 90° polarization is vertical, 0° is horizontal
2.  $\theta$  indicates scan angle from nadir (ranges from 0° to 50°);
3. From NOAA/NESDIS NOAA-KLM Instrument Guide, 2000

### 3. Precipitation Effects in the Microwave Spectrum

The goal of this study is to correct for precipitation effects on AMSU-A sounding channel brightness temperatures. This chapter applies Mie scattering theory to hydrometeors and the microwave spectrum, examines previous studies of microwave precipitation effects, and presents a 1-dimensional conceptual model demonstrating the feasibility of the approach to precipitation correction developed in later chapters.

#### 3.1. Mie Theory

In order to understand how hydrometeors--liquid or frozen water suspended in the atmosphere--interact with microwave radiation, we need to understand the theory governing the interaction of electromagnetic waves and particles they encounter. When such an encounter occurs the incident wave can create dipole moments within its constituent molecules, which will in turn radiate their own electromagnetic fields. The resulting field within and outside the particle is the sum of the incident field and the re-radiated fields from all the dipoles comprising the particle. Some of the molecules within the particle will absorb energy without re-radiating, and interference among the fields from the dipoles that do radiate and the incident field will cause energy to be radiated preferentially in certain directions. So particles absorb some of the incident energy, and scatter the rest in directions different from the incident direction.

Lorentz, Mie, and Debye each arrived separately at similar analytical solutions for absorption and scattering in the special case of spherical symmetry (Bohren and Huffman 1983). Today, most refer to this solution as Mie theory. More complex particle shapes require a model of the individual dipoles in the particle and explicitly account for the interaction of each re-

radiated field. The discrete dipole approximation (Draine and Flatau 1994) and finite difference time domain technique (Liou 2002) are examples of numerical techniques now possible.

Mie theory begins with the vector wave equation, which satisfies Maxwell's equations, and governs the propagation of electromagnetic waves. The wave equation is transformed into spherical coordinates, and the appropriate boundary conditions for spherical geometry are applied. The solution for the resulting fields is obtained by separating variables so the solution has radial and zenith-angle components. Solutions are linear combinations of a series of spherical Bessel functions,  $a_n$  and  $b_n$ , and angle-dependent functions,  $\pi_n$  and  $\tau_n$ .  $\pi_n$  and  $\tau_n$  are functions of the scattering angle,  $\theta$ , between the incident and scattered direction.  $a_n$  and  $b_n$  are complex functions of the particle's refractive index and size parameter,  $x$ .  $x$  is non-dimensional and expresses the particle's radius,  $a$ , relative to the wavelength of the incident radiation:

$$x = \frac{2\pi a}{\lambda}$$

By summing the energy entering and leaving a volume surrounding the particle, expressions can be obtained for the extinction,  $C_e$ , and scattering,  $C_s$ , cross sections (units of area) of the particle. The corresponding scattering and extinction efficiencies,  $Q_s$ , and  $Q_e$ , are the ratio of these cross-sections to the particle's geometric cross-sectional area, and are defined in terms of the spherical Bessel functions:

$$Q_e = \frac{2}{x^2} \sum_{n=1}^{\infty} (2n+1) \operatorname{Re}(a_n + b_n)$$

$$Q_s = \frac{2}{x^2} \sum_{n=1}^{\infty} (2n+1) (|a_n|^2 + |b_n|^2)$$

The single-scatter albedo,  $\omega$ , is the ratio of the scattering efficiency to the extinction efficiency. The asymmetry parameter,  $g$ , is the expectation value of  $\cos(\theta)$ . Particles that scatter

isotropically will have  $g = 0$  (however,  $g$  can also be zero even for non-isotropic scattering); those that scatter preferentially in the forward direction will have values of  $g$  between 0 and 1, while those that scatter more radiation backward will have  $g$  between 0 and -1.  $g$  is also a series solution of the spherical Bessel functions (Bohren and Huffman 1983):

$$g = \frac{4}{Q_s x^2} \left[ \sum_n \frac{n(n+2)}{n+1} \operatorname{Re}(a_n a_{n+1}^* + b_n b_{n+1}^*) + \sum_n \frac{2n+1}{n(n+1)} \operatorname{Re}(a_n b_n^*) \right]$$

Collectively,  $Q_e$ ,  $\omega$ , and  $g$ , are referred to as a particle's Mie properties, as they describe how much incident radiation a particle extinguishes, what fraction of the extinguished radiation is scattered, and the degree to which it is forward- or back-scattered. Figures 3.1 and 3.2 depict Mie properties at the lowest and highest AMSU-A and -B frequencies for rain, snow, and two different densities of graupel.

The differing behavior of the curves for different hydrometeors results from the marked difference in refractive index between ice and water in the microwave portion of the spectrum. Ice has a very small imaginary component, which causes its  $Q_e$  and  $Q_s$  to be very nearly equal. Thus, ice mostly scatters microwave radiation, while absorbing very little ( $\omega \approx 1$ ). Water, on the other hand, has an imaginary component of the same order of magnitude as its real component, so it both

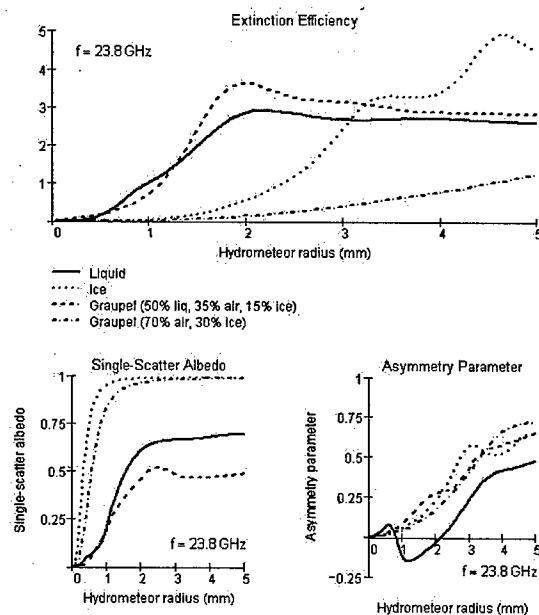


Figure 3.1: Mie properties for liquid water, ice, graupel, and melting graupel at 23.8 GHz (AMSU-A channel 1).

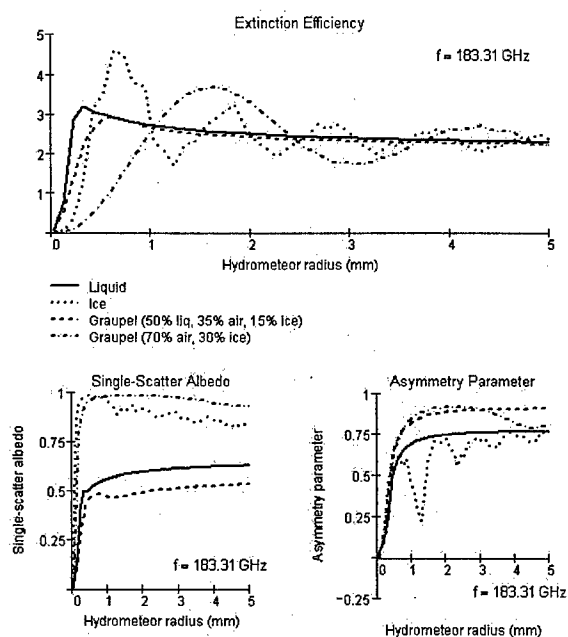


Figure 3.2: Same as Figure 3.1, but for 183.31 GHz (AMSU-B channels 18-20).

absorbs and scatters ( $\omega < 1$ ). Graupel is a type of hydrometeor composed of rimed snow particles, which may also contain water if in the process of melting. Determining the complex refractive index for this type of hydrometeor requires a dielectric mixing formula, such as that of Maxwell and Garnett or Bruggeman (used in this study) and the relative mass fraction of each substance in the particle. Figure 3.3 depicts the complex refractive index across the microwave

spectrum for pure water, pure ice, and two densities of graupel.

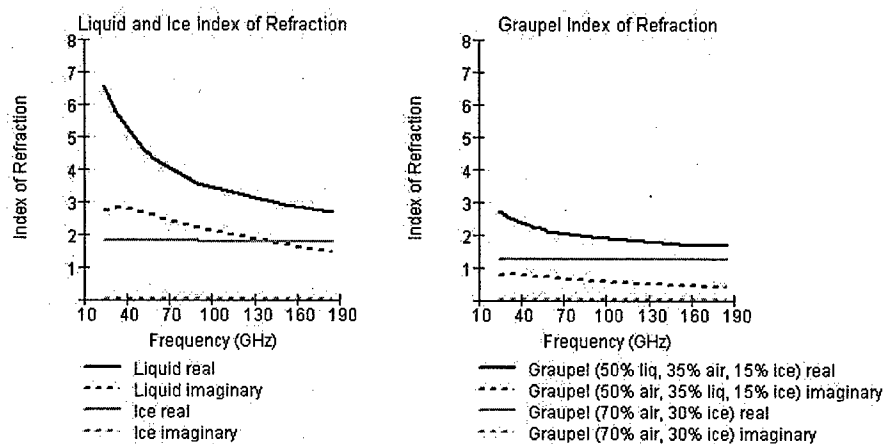


Figure 3.3: Complex indices of refraction across the microwave spectrum for pure liquid (black curves, left), pure ice (gray curves, left), melting graupel (black curves, right), and low-density graupel (gray curves, right).

The variation in each extinction curve with hydrometeor size falls into three broad regimes. For small particles whose size parameter is much less than unity,  $Q_e$  increases approximately in proportion to  $x$ , while  $\omega$  increases with  $x^3$ . This is the Rayleigh regime. In this regime, absorption depends not on particle size, but only on the total mass of absorbers present, as is the case with gaseous absorption. Cloud droplets have small enough size parameters in the microwave spectrum that scattering is negligible and absorption is approximately proportional to cloud liquid water density. For small precipitating drops and crystals, scattering starts to become significant, but in the Rayleigh regime, scattering is symmetric forward and backward and  $g \approx 0$ .

As the size parameter approaches unity (in the microwave spectrum, this includes hydrometeors with radii from 0.25 to 2 mm), scattering and extinction efficiencies peak. This is the Mie regime, which applies to large hydrometeors. The extinction efficiency in this regime is actually greater than 1 (it can in fact reach  $\sim 4$ ) due to diffraction of radiation missing, but passing close by, the particle. In the Mie regime, the asymmetry parameter approaches one as scattering becomes sharply forward-peaked.

Very large size parameters (greater than approximately  $10^4$ ) comprise the geometric optics regime, where a particle is so large compared to the incident wavelength that it no longer needs to be treated as a collection of individual dipoles. An incident beam can be traced through it as a ray, obeying Snell's laws for each reflection and refraction at the boundaries. In the geometric optics regime, scattering and extinction efficiencies approach and oscillate (due to interference) about limiting values. Extinction efficiencies exceeding unity and large forward scattering peaks in the Mie and geometric optics regimes are caused by diffraction slightly distorting the paths of photons that pass near, but do not contact, the particle.

The path traced out by an electromagnetic wave's electric field vector as it oscillates defines the wave's polarization. Maxwell's equations are satisfied by waves with linear or elliptical polarization. A beam of radiation may in turn be composed of waves with a preferred polarization or a collection of waves with random polarizations, in which case the beam is unpolarized. The polarization state can be described by the Stokes vector,  $I$ , which is composed of 4 scalar elements,  $I$ ,  $Q$ ,  $U$ , and  $V$ .  $I$  describes the total intensity of the beam;  $Q$  the intensity having vertical ( $Q > 0$ ) or horizontal ( $Q < 0$ ) polarization relative to the plane of scattering;  $U$  the intensity having  $\pm 45^\circ$  oblique polarization; and  $V$  the intensity with either right-hand or left-hand circular polarization. Each interaction the wave undergoes can be described by a Mueller matrix,  $M$ , which relates the scattered Stokes vector,  $I'$ , to the incident Stokes vector,  $I$ :

$$\begin{pmatrix} I' \\ Q' \\ U' \\ V' \end{pmatrix} = \frac{1}{k^2 r^2} \begin{bmatrix} S_{11} & S_{12} & S_{13} & S_{14} \\ S_{21} & S_{22} & S_{23} & S_{24} \\ S_{31} & S_{32} & S_{33} & S_{34} \\ S_{41} & S_{42} & S_{43} & S_{44} \end{bmatrix} \begin{pmatrix} I \\ Q \\ U \\ V \end{pmatrix}$$

In the special case of a spherical particle, the Mueller matrix becomes:

$$\begin{pmatrix} I' \\ Q' \\ U' \\ V' \end{pmatrix} = \frac{1}{k^2 r^2} \begin{bmatrix} S_{11}(\theta) & S_{12}(\theta) & 0 & 0 \\ S_{12}(\theta) & S_{11}(\theta) & 0 & 0 \\ 0 & 0 & S_{33}(\theta) & S_{34}(\theta) \\ 0 & 0 & -S_{34}(\theta) & S_{33}(\theta) \end{bmatrix} \begin{pmatrix} I \\ Q \\ U \\ V \end{pmatrix}$$

where  $S_{11}$ ,  $S_{12}$ ,  $S_{33}$ , and  $S_{34}$  are all functions of the scattering zenith angle,  $\theta$ , the spherical Bessel functions,  $a_n$  and  $b_n$ , and the angle-dependent functions,  $\pi_n$  and  $\tau_n$ . It is important to note here that scattering--even by spherical particles--can cause polarization (the polarization of sky light is an example).

The scattered intensity at a given scattering angle, as determined by the Mueller matrix, is related to the incident intensity by the phase function,  $P(\theta)$ . The phase function is in turn determined by elements  $S_{11}$  and  $S_{12}$ , as well as the intensity and degree of horizontal/vertical polarization of the incident beam. Since the computation of these matrix elements requires a series solution, computing them for all scattering angles can be computationally expensive. Instead, the asymmetry parameter can be used with one of a variety of approximate phase functions to predict scattered intensity vs. scattering angle. The most common of these is the Henyey-Greenstein phase function:

$$P_{HG}(\theta) = \frac{1 - g^2}{(1 + g^2 - 2g \cos(\theta))^2}$$

Chapter 2 dealt with one-dimensional radiative transfer in a non-scattering medium. For radiation traveling in a specified direction  $\Omega$  in a medium that does scatter (so that the extinction coefficient,  $\beta_e$ , equals the sum of the absorption,  $\beta_a$ , and scattering,  $\beta_s$ , coefficients), we need to use the general form of the radiative transfer equation:

$$\frac{dI(\Omega)}{ds} = -\beta_e I(\Omega) + \beta_a B(T) + \frac{\beta_s}{4\pi} \int_{4\pi} P(\Omega, \Omega') I(\Omega') d\Omega'$$

Using the definitions of the single-scatter albedo and optical path, this reduces to:

$$\frac{dI(\Omega)}{d\tau} = -I(\Omega) + (1 - \omega) B(T) + \frac{\omega}{4\pi} \int_{4\pi} P(\Omega, \Omega') I(\Omega') d\Omega'$$

So to compute the radiative properties of an atmospheric layer, we need to know three quantities: the extinction coefficient,  $\beta_e$ ; the single-scatter albedo,  $\omega$ , and the scattering phase function,  $P(\Omega, \Omega')$ , which relates the intensity scattered in direction  $\Omega$  that originated from direction  $\Omega'$ . We can approximate the phase function using  $g$ . Multiplying the extinction efficiency, cross-

sectional area, and number density of a given-size hydrometeor results in the extinction coefficient for that size particle. Summing the extinction coefficients for all sizes of the hydrometeor size distribution yields the total extinction coefficient. The same procedure yields the total scattering coefficient, and the ratio of these quantities produces the single-scatter albedo. The asymmetry parameter for a collection of particles is the sum of each size's asymmetry parameter, weighted by number density.

Since actual precipitation size distributions can vary widely, we arrive at the number density for each infinitesimal increment of liquid drop or ice crystal diameter,  $D$ , using empirically-derived drop size distribution models. The well-known Marshall-Palmer distribution for rain and graupel relates rain rate,  $R$ , to number density:

$$N(D) = N_0 e^{-\Lambda(R)D}, \quad N_0 = 0.08 \text{ cm}^{-4}, \quad \Lambda(R) = 41 \text{ cm}^{-1} \left( \frac{R}{\text{mm hr}^{-1}} \right)^{-0.21}$$

The Sekhon-Srivastava distribution is a commonly used, but less reliable, equivalent for snow:

$$N(D) = N_0(R) e^{-\Lambda(R)D}, \quad N_0(R) = 2.5 \times 10^{-2} \left( \frac{R}{\text{mm hr}^{-1}} \right)^{-0.94} \text{ cm}^{-4}, \quad \Lambda(R) = 22.9 \text{ cm}^{-1} \left( \frac{R}{\text{mm hr}^{-1}} \right)^{-0.45}$$

where, in this case,  $R$  is the rain-equivalent precipitation rate. Petty (2001a) introduced a modification to both distributions by dividing the exponential factor by  $2^\delta$ . This enables the effective particle diameter to be scaled up or down readily in order to produce more realistic extinction and scattering coefficients. In this study, as in Petty (2001a),  $\delta=2$  is employed for the snow size distribution. The rain rate can be derived from a given mass density of hydrometeors

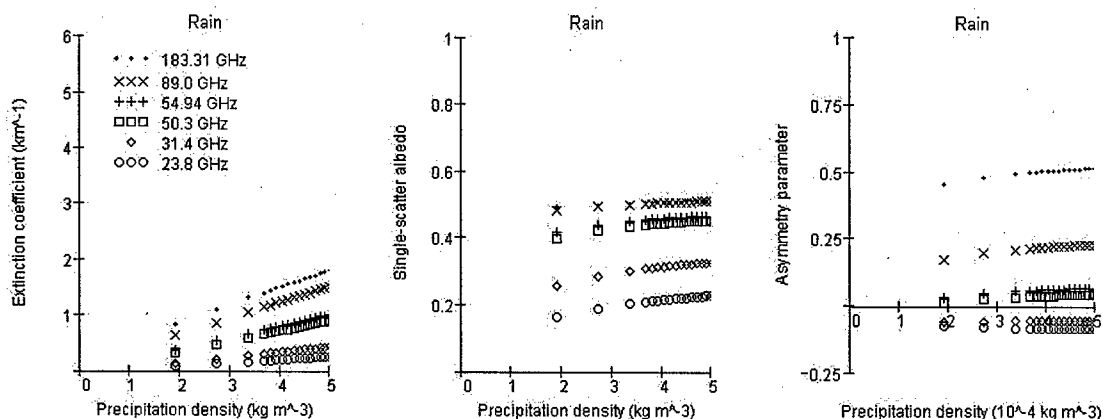


Figure 3.4: Extinction coefficient (km<sup>-1</sup>; left), single-scatter albedo (center), and asymmetry parameter (right) obtained from Mie calculations at AMSU-A and -B frequencies for various rain densities. Particle size distributions used in the calculations were obtained from a Marshall-Palmer distribution modified using the method of Petty (2001) to account for fall-speed variation with air density.

once the fall speed,  $u$  (a function of hydrometeor size), is known. Usually a power-law relation,  $u(D) = aD^b$ , is assumed.

Figures 3.4 through 3.6 depict the extinction coefficient, single-scatter albedo, and

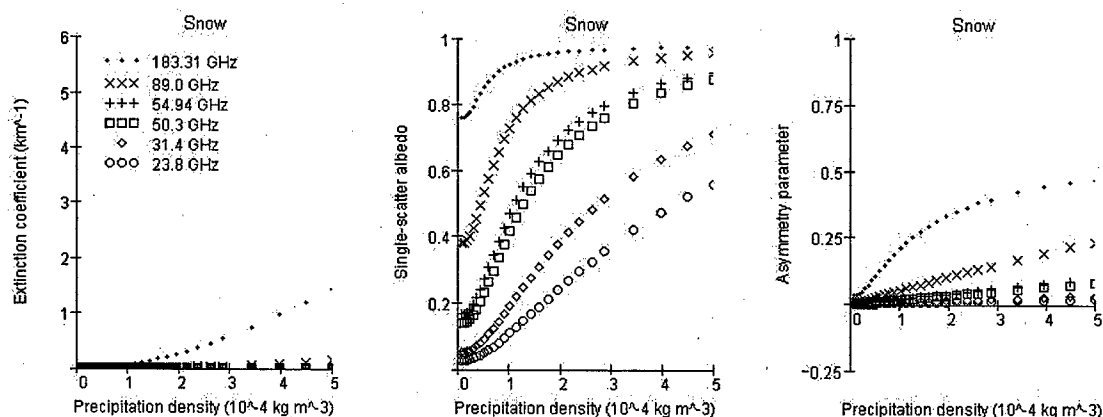


Figure 3.5: Same as Figure 3.4, but for snow (modeled as ice spheres). Particle size distributions derived from Sekhon-Srivastava size distribution, with reverse-exponential decay parameter scaling and fall-speed modifications from Petty (2001).

asymmetry parameter vs. precipitation density for rain, snow, and graupel at AMSU-A and -B frequencies. From these figures, we can see that rain extinction efficiency increases with frequency. Its single-scatter albedo does also, making it a moderate scatterer at high frequencies. At those frequencies, it scatters strongly in the forward direction ( $g \approx 0.5$ ); at temperature sounding frequencies it scatters isotropically, and at low frequencies it actually back-scatters slightly.

Snow extinction is much smaller than rain at all frequencies, and only becomes significant at high frequencies. Single-scatter albedo is larger than for rain, due to ice's very small imaginary index of refraction. Snow asymmetry parameters are between 0 and 0.5, so when snow scatters, it does so with a moderately-strong phase function forward peak.

Graupel's low density makes it considerably larger (nearly a factor of 2) for the same precipitation density. The larger geometric size increases its extinction coefficient relative to rain and, especially, snow. The larger particles scatter more strongly, and with a sharper forward peak ( $g$  reaching 0.8 for high frequencies).

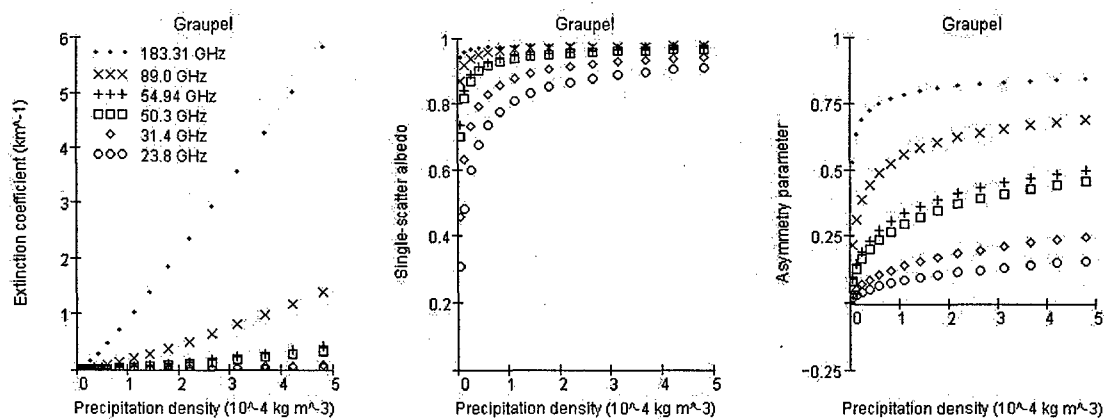


Figure 3.6: Same as Figures 3.4 and 3.5, but for graupel (70% air, 30% ice). Fall-speed modified Marshall-Palmer size distribution used for Mie calculations.

### 3.2. Previous Microwave Precipitation Studies

To date, the bulk of existing microwave precipitation research has been focused on quantifying surface precipitation rates or inferring precipitation profiles using microwave instruments.

The earliest work in this area occurred in the mid-1970's, after the first research microwave radiometers were flown. Grody (1976) noted that a pair of microwave frequencies located different distances from the 22 GHz WV absorption band could be used to determine the optical depth of water vapor and cloud liquid water present. He presented regression-based algorithms to retrieve total precipitable water and cloud liquid water using the Nimbus-E Microwave Spectrometer's 22.235 GHz and 31.40 GHz channels.

Wilheit et al. (1977) employed 19.35 GHz *TB*'s from the Electrically Scanning Microwave Radiometer (EMSR) to estimate surface rain rate. He used Mie theory as described above to model *TB19* of a raining oceanic cloud of varying thicknesses and with varying freezing levels, both with and without scattering. Using this information, he developed a relation between *TB19* and over-ocean surface rain rates (up to 20 mm hr<sup>-1</sup>) that was accurate to within a factor of two. A number of variations of this emission-based rain rate estimation technique have been developed for succeeding instruments.

Wu and Weinman in 1984 used the Nimbus-7 Scanning Multi-channel Microwave Radiometer to study ice scattering effects on 37 GHz *TB* and concluded that at this frequency and above, scattering effects become significant and could be used to infer surface rain rates. Spencer (1986) expanded on this, developing a scattering-based rain rate estimate which

compares dual-polarized  $TB_{37}$  to expected values from a non-raining cloudy or clear oceanic scene.

The introduction of the Special Sensor Microwave Imager (SSM/I), flown continuously by the Defense Meteorological Satellite Program (DMSP) constellation since 1987, enabled a great deal of groundbreaking work in precipitation measurement. SSM/I is a conically-scanning microwave radiometer with channels at 19, 22, 37, and 85 GHz. All channels are dual-polarized, except 22 GHz, which is vertically-polarized only. Instrument resolution varies from 70 km at 19 GHz to 16 km at 85 GHz. SSM/I was the first instrument to employ both low- and high-frequency window frequencies simultaneously, and led to a number of novel algorithms for retrieving water vapor, cloud liquid, precipitation, and ocean and land surface parameters.

Grody (1991) developed an empirical scattering index, which uses  $TB_{19V}$  and  $TB_{22V}$  to predict what  $TB_{85V}$  would be in the absence of scattering hydrometeors. He used the difference between predicted and actual  $TB_{85V}$  to classify precipitating scenes, but not to estimate rain rate. Liu and Curry (1992) followed a similar approach, but used both low-frequency (19 GHz) and high-frequency (85 GHz)  $TB$  differences as rain rate predictors. In his SSM/I rain rate algorithm, Petty (1994) used an 85 GHz scattering index,  $S$ , to determine a first-guess rain rate, then iteratively adjusted it until the predicted 19 and 37 GHz normalized polarization index,  $P$ , which measures rain cloud opacity, matches the observed values.

Bennartz and Petty (2001) sounded a cautionary note about scattering-based precipitation retrievals. They used SSM/I  $TB$ 's, coupled with varying ice particle size distributions, to predict radar reflectivity, which they compared with actual radar observations. The results indicate a strong dependence of  $TB$  on the assumed particle size distribution used in their Mie calculations.

The Tropical Rainfall Measuring Mission (TRMM) was launched in 1997, and continues to operate today. TRMM contains a microwave imager (TMI) nearly identical to SSMI, as well as an active microwave instrument, the precipitation radar (PR). Bauer (2001) used the new instrument, TMI, as well as a new approach to measuring precipitation: principal component analysis (PCA). PCA identifies patterns of covariance in multivariate datasets by computing the eigenvalues and eigenvectors of the data's covariance matrix. The eigenvectors span the observation space, and so each multi-variable observation can be reproduced by a linear combination of the eigenvectors. The coefficient corresponding to each eigenvector is its principal component (PC). The eigenvalue corresponding to each eigenvector represents the fraction of the data's variance explained by that eigenvector. Bauer related PC's, rather than a single channel or subset of channels, to rain rate, and--surprisingly--found that scattering effects on *TB85* reduced its usefulness in predicting rain rate; excluding *TB85* from the data set prior to PCA improved the correlation of the PC's with rain rate.

Petty (2001a) took a similar approach, using PCA with SSMI TB's to analyze tropical stratiform precipitation. He found that the first EOF, whose elements were all the same sign, corresponded to overall ice scattering intensity. The second EOF, with *TB19* and *TB22* deviations of opposite sign from *TB37* and *TB85*, represented the multi-channel rain signature (i.e. low-frequency rain emission and high-frequency ice scattering). The third EOF, dominated by *TB85* deviation, accounted for anomalously strong 85 GHz ice scattering. Interestingly, the magnitudes of the components of EOF1 follow a power-law relationship, allowing a frequency-dependent prediction of scattering attenuation.

A fourth form of rain retrieval capitalizes on recent strides in fine-scale numerical weather prediction (NWP) model resolution and microphysics. An NWP model is used to produce temperature, humidity, and precipitation fields at cloud or sub-cloud scales. The meteorological profile at each horizontal grid point is then used as input to a radiative transfer model, typically a 1-dimensional plane-parallel Eddington two-stream approximation, to compute upwelling microwave brightness temperatures. The grid-scale brightness temperature field is then convolved to the resolution of the instrument being simulated. The simulation results are stored, creating a library of brightness temperatures matching different precipitation profiles. These libraries form the basis for Bayesian precipitation profile retrievals, which infer the profiles from the library profiles best matching a set of observed brightness temperatures (Kummerow 1996). An extensive series of papers spanning the 1990's and first half of this decade have focused on optimal techniques for creating these "cloud-radiation databases," and improving NWP model microphysical assumptions to better match observed brightness temperatures (Mugnai et al. 1990; Smith et al. 1991; Mugnai et al. 1993; Smith et al. 1994; Panegrossi et al. 1998).

In the same vein, Panegrossi (2004) focused attention on mismatches between observed Tropical Rainfall Measuring Mission (TRMM) Microwave Imager (TMI) *TB*'s from Hurricane Bonnie (1998) and simulated *TB*'s from a University of Wisconsin Nonhydrostatic Modeling System (UW-NMS) simulation of the storm. She demonstrated that frozen hydrometeors can have strong scattering effects on 37 GHz brightness temperatures, and reduced simulated vs. observed discrepancies at this frequency by changing the model's hydrometeor categorization of low-density graupel (essentially rimed ice crystals) to snow, leaving the graupel category for

hail. She also showed that anomalously warm 85 GHz brightness temperatures could be caused by emission from supercooled water droplets lofted into the upper troposphere by deep cumulus convection and warm 10 GHz brightness temperatures by overly strong rain.

Just as SSMI and the TMI/PR combination each triggered a wave of rain rate and precipitation profile retrievals, the 1998 introduction of AMSU-A and -B, with a suite of window channels well-suited for cloud water and precipitation profiling, spawned a large body of work on microwave precipitation effects. Grody (1999) adapted his SSMI scattering index for AMSU-A use, using regression analysis to develop an expression for non-scattering  $TB_{89}$  using  $TB_{23}$  and  $TB_{31}$ . Grody then used an observed  $TB_{89}$  more than 9 K colder than the predicted value to distinguish areas of precipitation over both land and sea.

Ferraro et al. (2000) describe the algorithms developed for operational use at NESDIS. They quantify scattering by simply subtracting  $TB_{89}$  from  $TB_{23}$ . Scattering indices  $> 3$  K are associated with stratiform rain;  $> 40$  K with cumulonimbus convection. For each precipitation type, Ferraro et al. derive rain rate using a power law with different coefficients for each type of precipitation. A similar algorithm, with the benefit of AMSU-B's finer spatial resolution, uses  $TB_{89} - TB_{150}$  as the scattering index. Bennartz et al. (2002) took a similar approach, using AMSU-A  $TB_{89}$  or AMSU-B  $TB_{150}$  vs. AMSU-A  $TB_{23}$  to derive categorical mid-latitude precipitation. Weng et al. (2003) describe NESDIS' operational total precipitable water (TPW), and cloud liquid water algorithms, which capitalize on the larger continuum water vapor absorption with increasing frequency. Finally, Bennartz and Bauer (2003) compared the ice scattering signature at 85, 150, and 183 GHz to each frequency's sensitivity to surface and water vapor emission. They found 150 GHz to be the optimal frequency for characterizing scattering.

It is less sensitive to surface emission than 85 GHz and, while 183 GHz channels are very sensitive to scattering (Burns et al. 1997), 150 GHz is less sensitive than 183 GHz to emission by variable water vapor content.

While the need for accurate precipitation rate and profile retrievals has motivated the large body of work studying precipitation effects on window frequencies, comparatively little has been done to study how precipitation affects AMSU-A temperature sounding channels (*TB4* through *TB14*; 52.8 to 57.29 GHz). Reale (2001) and Greenwald et al. (2004) recognize that scattering can affect sounding channel TB's and point out that current global NWP model data assimilation schemes reject radiances from precipitating AMSU-A fields of view. Such fields of view are identified by cloud liquid water content  $> 0.2$  mm. Li and Weng (2002) found that scattering *TB* depression in the lowest tropospheric sounding channels (AMSU-A channels 4 and 5, with weighting functions that peak at the surface and near 700 hPa respectively) is well-correlated with ice water path (IWP) and somewhat correlated with liquid water path (LWP).

A known temperature profile is a necessary precursor to retrieving moisture profiles using the 183 GHz AMSU-B channels (*TB18* through *TB20*), since the water vapor content dictates what level each channel peaks at, but the temperature near that level dictates what the actual 183 GHz *TB* will be. As a first step, then, in their humidity profile retrieval algorithm, Chen and Staelin (2003) required temperatures from AMSU-A channels 4 through 8. Recognizing that channels 4 and 5 could be strongly affected (several K) by precipitation attenuation, they devised a scheme to predict *TB4* and *TB5* precipitation-related perturbations at AMSU-B resolution using the strong scattering sensitivity of AMSU-B *TB19* and *TB20*. They then corrected *TB4* and *TB5* using a regression relation with the *TB19* and *TB20* perturbations.

Most recently, Bauer and Mugnai (2003) capitalized on precipitation attenuation of sounding channels to develop a precipitation profile algorithm employing 60 and 118 GHz TB from an aircraft-mounted microwave radiometer. Their Bayesian approach uses a profile library developed from a numerical simulation of Hurricane Bonnie (1998) and 60 and 118 GHz TB's predicted using a two-stream Eddington radiative transfer model. The retrieval is based on the differential scattering susceptibility of 60 and 118 GHz channels that peak at nearly the same level.

### 3.3. A 1-d Conceptual Model for Precipitation Effects on AMSU Brightness Temperatures

As we have seen, theory and previous studies demonstrate the strong susceptibility of high-frequency window channels to ice scattering. Chapters 4 and 5 will use radiative transfer simulations and a sample of observational AMSU data to test the hypothesis that *scattering depression of high-frequency window channels (TB15 through TB20) can be used to quantify the scattering depression of 55 GHz temperature sounding channels (TB5 through TB8)*. Before proceeding to those steps, this section presents a simple 1-D conceptual model to check the feasibility of such an approach.

Figure 3.7 depicts the one-dimensional plane-parallel model geometry. The ocean surface is specular, with reflectivity  $r_{sea}$  and temperature  $T_{sea}$ . The troposphere is divided into two layers: the upper troposphere, which is the area of primary sounding channel sensitivity, and the lower troposphere, which lies below the bulk of the sounding channel weighting function. The lower tropospheric layer has temperature  $T_{la}$  and transmittance  $t_{la}$ . Superimposed on the lower tropospheric layer is a rain layer with temperature  $T_{rain}$ , transmittance  $t_{rain}$ , and single-

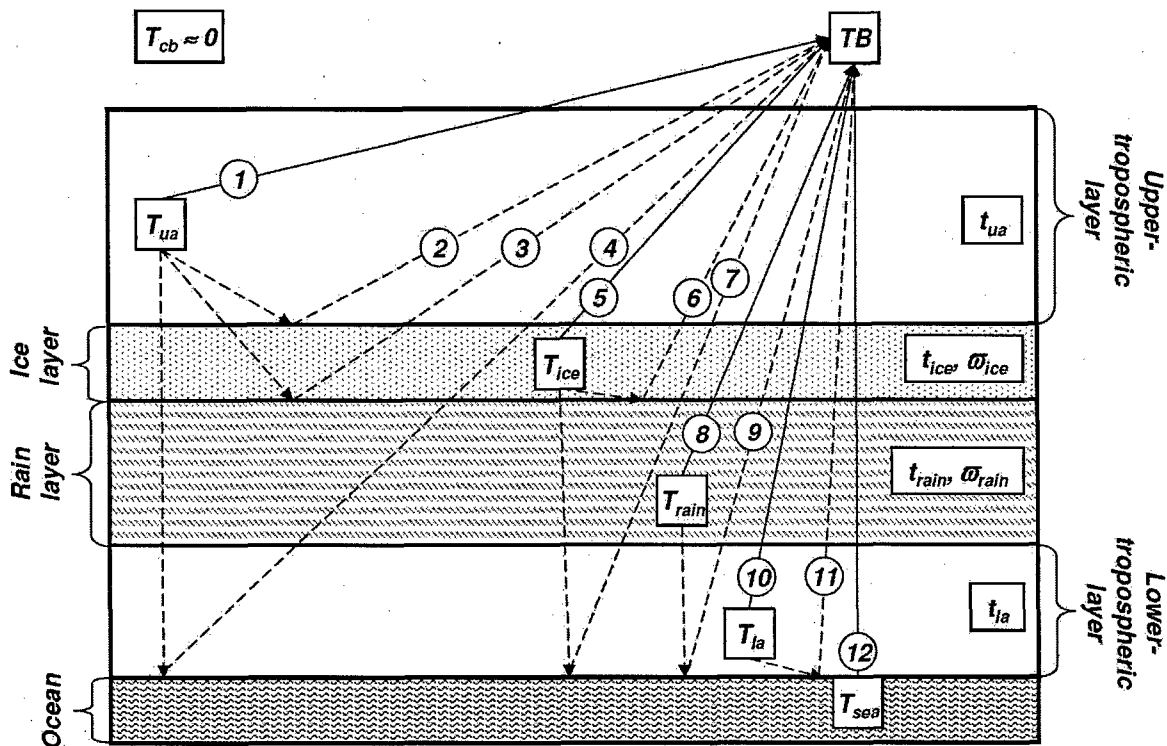


Figure 3.7: Geometry of the 1-D plane-parallel conceptual model for hydrometeor effects on AMSU window and sounding channel TB's. The brightness temperature observed by the instrument is the sum of 12 components (see text). Solid lines denote direct emission paths while dashed lines denote reflected emission paths.  $T$  indicates a layer's temperature,  $t$  its transmittance, and  $\omega$  its single-scattering albedo.

scatter albedo  $\omega_{rain}$ . Capping the rain layer is an ice layer with temperature  $T_{ice}$ , transmittance  $t_{ice}$ , and single-scatter albedo  $\omega_{ice}$ . Above the cloud is an upper-atmosphere layer with  $T_{ua}$  and  $t_{ua}$ . The cosmic background temperature,  $T_{cb}$ , is neglected. Two radiance streams--one upward and one downward--are tracked. All scattering directs intensity from one stream into the other. Multiple scattering is neglected.

The predicted  $TB$  measured by the instrument is composed of twelve components:

1. Direct upward emission from the upper-tropospheric layer:

$$TB_1 = T_{ua} (1 - t_{ua})$$

(Note that for a non-scattering layer, such as the upper troposphere, the sum of absorption and scattering is unity. Kirchhoff's Law requires emissivity to equal absorptivity, so the emissivity of a non-scattering layer becomes  $(1-t)$ .)

2. Downward emission from the upper-troposphere reflected by the ice layer and transmitted back upward through the upper-troposphere:

$$TB_2 = T_{ua} (1-t_{ua}) \omega_{ice} (1-t_{ice}) t_{ua}$$

3. Downward upper-tropospheric emission reflected by the rain layer and transmitted back upward to space:

$$TB_3 = T_{ua} (1-t_{ua}) t_{ice} \omega_{rain} (1-t_{rain}) t_{ice} t_{ua}$$

4. Downward upper-tropospheric emission reflected by the ocean surface and transmitted back upward:

$$TB_4 = T_{ua} (1-t_{ua}) t_{ice} t_{rain} t_{la} r_{sea} t_{la} t_{rain} t_{ice} t_{ua}$$

5. Upward ice-layer emission transmitted to space:

$$TB_5 = T_{ice} (1-t_{ice}) (1-\omega_{ice}) t_{ua}$$

(For the ice and rain layers, where scattering occurs, the layer's emissivity is  $(1-t)(1-\omega)$ .)

6. Downward ice layer emission reflected off the rain layer and transmitted upward to space:

$$TB_6 = T_{ice} (1-t_{ice}) (1-\omega_{ice}) \omega_{rain} (1-t_{rain}) t_{ice} t_{ua}$$

7. Downward ice layer emission reflected off the ocean surface and transmitted back upward:

$$TB_7 = T_{ice} (1-t_{ice}) (1-\omega_{ice}) t_{rain} t_{la} r_{sea} t_{la} t_{rain} t_{ice} t_{ua}$$

8. Upward emission from the rain layer transmitted through the ice layer and upper-troposphere:

$$TB_8 = T_{rain} (1-t_{rain}) (1-\omega_{rain}) t_{ice} t_{ua}$$

9. Downward emission from the rain layer reflected by the ocean surface and transmitted back upward:

$$TB_9 = T_{rain} (1 - t_{rain}) (1 - \omega_{rain}) t_{la} r_{sea} t_{la} t_{rain} t_{ice} t_{ua}$$

10. Upward emission from the lower troposphere transmitted through the rain, ice, and upper-troposphere layers:

$$TB_{10} = T_{la} (1 - t_{la}) t_{rain} t_{ice} t_{ua}$$

11. Downward emission from the lower troposphere reflected by the ocean surface, then transmitted upward through all layers:

$$TB_{11} = T_{la} (1 - t_{la}) r_{sea} t_{la} t_{rain} t_{ice} t_{ua}$$

12. Upward emission from the ocean surface, transmitted upward to space:

$$TB_{12} = T_{sea} (1 - r_{sea}) t_{la} t_{rain} t_{ice} t_{ua}$$

(For the ocean surface, reflectivity and absorptivity sum to unity so its emissivity is  $(1 - r)$ .)

The total brightness temperature measured from space is then the sum of these twelve components:

$$TB = \left\{ \begin{array}{l} T_{ua} (1 - t_{ua}) \left[ \begin{array}{l} 1 \\ + \omega_{ice} (1 - t_{ice}) t_{ua} \\ + \omega_{rain} (1 - t_{rain}) t_{ice}^2 t_{ua} \\ + r_{sea} t_{la}^2 t_{rain}^2 t_{ice}^2 t_{ua} \end{array} \right] \\ + T_{ice} (1 - t_{ice}) (1 - \omega_{ice}) \left[ \begin{array}{l} t_{ua} \\ + \omega_{rain} (1 - t_{rain}) t_{ice} t_{ua} \\ + r_{sea} t_{la}^2 t_{rain}^2 t_{ice} t_{ua} \end{array} \right] \\ + T_{rain} (1 - t_{rain}) (1 - \omega_{rain}) t_{ice} t_{ua} \left[ \begin{array}{l} 1 \\ + r_{sea} t_{la}^2 t_{rain} \end{array} \right] \\ + T_{la} (1 - t_{la}) t_{rain} t_{ice} t_{ua} \left[ \begin{array}{l} 1 \\ + r_{sea} t_{la} \end{array} \right] \\ + T_{sea} (1 - r_{sea}) t_{la} t_{rain} t_{ice} t_{ua} \end{array} \right\} \quad (3.1)$$

Limiting cases of clear conditions, an opaque lower troposphere, an opaque rain layer, and an opaque ice layer highlight the effects of water vapor and precipitation at different frequencies. For the limiting case of an atmosphere with no precipitation ( $t_{rain} = t_{ice} = 1$ ):

$$TB_{non-precip} = T_{ua}(1-t_{ua})(1+r_{sea}t_{la}^2t_{ua}) + T_{la}(1-t_{la})t_{ua}(1+r_{sea}t_{la}) + T_{sea}(1-r_{sea})t_{la}t_{ua}$$

For window channels, where  $t_{ua} \approx t_{la} \approx 1$ ,  $TB \rightarrow T_{sea}(1-r_{sea})$  and the observed  $TB$  will be approximately equal to that of the radiometrically cold ocean surface. For temperature and moisture sounding channels, where  $t_{la} \approx 0$  and  $t_{ua}$  is small,  $TB \rightarrow T_{ua}(1-t_{ua}) + T_{la}t_{ua}$  and the observed  $TB$  will be nearly equal to the upper-tropospheric temperature, with a small contribution by emission from the lower troposphere. As lower-tropospheric humidity increases, and  $t_{la}$  goes to zero (faster at high-frequencies) due to WV absorption,  $TB \rightarrow T_{la}$  and the observed  $TB$  approaches the opaque lower troposphere's temperature.

For an atmosphere with an opaque rain layer and no ice:

$$TB_{opaque\_warm\_rain} = T_{ua}(1-t_{ua})(1+\omega_{rain}t_{ua}) + T_{rain}(1-\omega_{rain})t_{ua}$$

In this case, observed  $TB$  depends only on upper-troposphere transmittance and the rain layer's single-scatter albedo. The Mie calculations in Sec 3.1 show that  $\omega_{rain}$  is about 0.25 for low-frequency window frequencies, and increases to  $\sim 0.5$  at high-frequencies.  $t_{ua}$  will be close to 1 for window frequencies and  $TB \rightarrow T_{rain}(1-\omega_{rain})$ . So the opaque rain is radiometrically cold for high frequencies due to scattering, which limits its emission, while it appears warmer at low frequencies where it emits more effectively. The low  $t_{ua}$  limits the rain layer's effect on 55 GHz

sounding channel  $TB$ . In effect, only the bottom tail of the 55 GHz weighting function extends down into the rain layer.

For an atmosphere with an opaque ice layer:

$$TB_{opaque\_ice} = T_{ua} (1 - t_{ua}) (1 + \omega_{ice} t_{ua}) + T_{ice} (1 - \omega_{ice}) t_{ua}$$

At low frequencies, ice extinction is very weak and it would be extremely difficult for an ice layer to be opaque. At high frequencies, ice can be significantly opaque and its higher  $\omega$  makes it appear even colder at these frequencies than the opaque rain layer. In fact, if the upper-troposphere is completely transparent and the ice layer is completely opaque,  $TB$  will approach 0.

The 1-D plane-parallel geometry greatly exaggerates precipitation effects in comparison with real-world observed  $TB$ 's, because the full instrument field of view is never completely filled with uniform deep convection producing opaque rain and ice layers like the ones modeled here. Instead, localized areas affected by rain and ice emission and scattering are averaged with large areas of ambient  $TB$ , muting the effect of the precipitation. Precipitating clouds should appear warmer when modeled in 3-D for two reasons: Petty (1994) pointed out that when viewed at oblique angles, the warm rain of a convective cloud can be viewed through the side of the cloud rather than through the ice layer capping it, reducing scattering attenuation. Additionally, ocean surface reflection of the warm rain emission can occur for some geometries, warming the radiometrically cold ocean surface's  $TB$  and counteracting some of the  $TB$  reduction caused by ice scattering in the scene.

Table 3.1 summarizes modeled low-frequency window ( $TB31$ ), temperature sounding ( $TB55$ ), and high-frequency window ( $TB89$  and  $TB150$ ) brightness temperatures using equation (3.1) for ten different cases. Rain and ice layer transmittances and single-scatter albedos are

Table 3.1: Modeled brightness temperatures at 31, 55, 89, and 150 GHz

Case	$T_{ia}$				$T_{rain}$				$T_{ice}$				$T_B$				$\Delta TB$				
	31	55	89	150	31	55	89	150	31	55	89	150	31	55	89	150	31	55	89	150	
Dry, no precip	1.0	0.1	1.0	1.0									135	230	180	195					
Standard	0.9	0.1	0.73	0.59									163	230	227	251					
Tropical	0.8	0.1	0.51	0.33									187	230	254	270					
Warm rain 1	0.8	0.1	0.51	0.33	0.9	0.81	0.73	0.66					195	230	227	227	8	-5	-27	-43	
Warm rain 2	0.8	0.1	0.51	0.33	0.8	0.64	0.51	0.41					201	229	203	196	14	-9	-51	-74	
Warm rain 3	0.8	0.1	0.51	0.33	0.7	0.49	0.34	0.24					206	229	184	174	18	-1.2	-70	-96	
Warm rain 4	0.8	0.1	0.51	0.33	0.6	0.36	0.22	0.13					209	229	169	160	22	-1.5	-85	-110	
Ice 1	0.8	0.1	0.51	0.33	0.6	0.36	0.22	0.13	0.999	0.995	0.983	0.951	209	229	166	152	22	-1.6	-87	-118	
Ice 2	0.8	0.1	0.51	0.33	0.6	0.36	0.22	0.13	0.995	0.975	0.918	0.778	208	228	156	126	21	-1.8	-98	-144	
Ice 3	0.8	0.1	0.51	0.33	0.6	0.36	0.22	0.13	0.990	0.951	0.843	0.605	207	228	144	99	20	-2.0	-110	-171	
	$T_{ia} = 225$		$t_{ua31} = 1.0$		$t_{ua55} = 0.1$		$t_{ua89} = 1.0$		$t_{ua150} = 1.0$												
	$T_{ice} = 265$		$0.99 < t_{ice31} < 1.0$		$t_{ice55} = t_{ice31}^5$		$t_{ice89} = t_{ice31}^{17}$		$t_{ice150} = t_{ice31}^{50}$												
			$\omega_{ice31} = 0.90$		$\omega_{ice55} = 0.96$		$\omega_{ice89} = 0.97$		$\omega_{ice150} = 0.98$												
	$T_{rain} = 285$		$0.6 < t_{rain31} < 1.0$		$t_{rain55} = t_{rain31}^2$		$t_{rain89} = t_{rain31}^3$		$t_{rain150} = t_{rain31}^4$												
			$\omega_{rain31} = 0.3$		$\omega_{rain55} = 0.4$		$\omega_{rain89} = 0.5$		$\omega_{rain150} = 0.5$												
	$T_{ia} = 275$		$0.8 < t_{ia31} < 1.0$		$t_{ia55} = 0.1$		$t_{ia89} = t_{ia31}^3$		$t_{ia150} = t_{ia31}^5$												
	$T_{sea} = 300$		$T_{sea31} = 0.55$		$T_{sea55} = 0.50$		$T_{sea89} = 0.40$		$T_{sea150} = 0.35$												

For all cases:

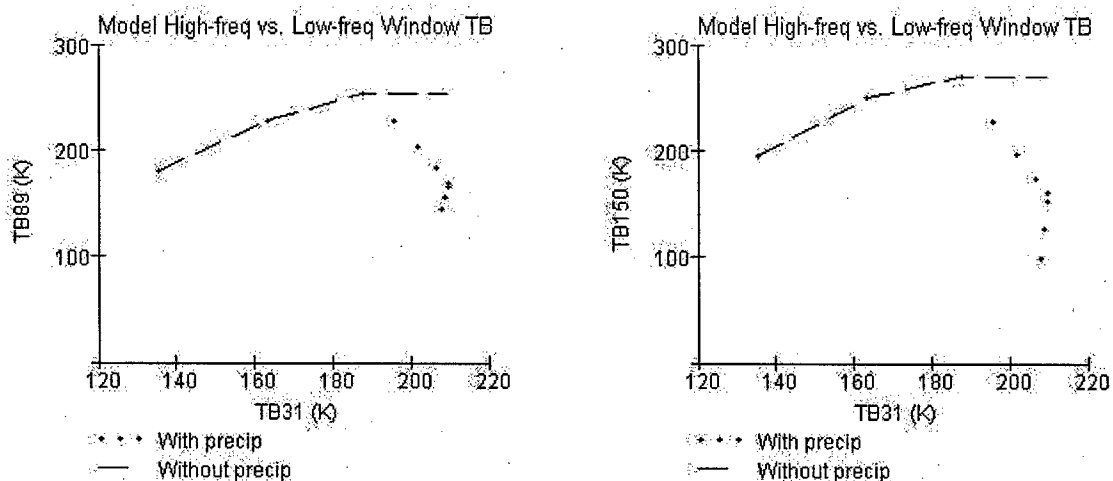


Figure 3.8: Modeled  $TB_{89}$  and  $TB_{150}$  vs.  $TB_{31}$ . Dashed curve depicts predicted  $TB$  without precipitation emission or scattering. Solid curve depicts modeled  $TB$  including precipitation effects. Table 3.1 summarizes assumptions and results for each of the 10 cases depicted here.

inferred from the precipitation Mie properties presented in Section 3.1. The rain and ice transmittances for higher frequencies are defined in terms of the 31 GHz transmittance, using the ratio of each frequency's extinction coefficient to its 31 GHz counterpart. The temperature of each layer is fixed. For window frequencies ( $TB_{31}$ ,  $TB_{89}$ , and  $TB_{150}$ ) the upper troposphere layer is transparent, while for the temperature sounding channel ( $TB_{55}$ ) its transmissivity is 0.1. Sea surface reflectivity is set to 0.55 for  $TB_{31}$ , decreasing to 0.35 for  $TB_{150}$ .

Three cases contained no precipitation, but steadily increasing humidity, represented by decreasing window channel  $t_{la}$ . This increased  $TB_{31}$  slightly (135 to 187 K), while increasing  $TB_{89}$  (180 to 254 K) and  $TB_{150}$  (195 to 270 K) more significantly.

Adding a warm rain layer of progressively greater opacity continued to warm  $TB_{31}$  slightly (195 to 209 K) while decreasing both the high frequency window channel  $TB$ 's due to scattering ( $TB_{89}$  drops from 254 to 169 K and  $TB_{150}$  drops from 270 to 160 K).  $TB_{55}$  also begins to decrease (by as much as 1.5 K) as rain intensity increases, due to the rain layer

replacing warm lower-tropospheric emission with radiometrically colder rain. Finally, adding an ice layer atop the warm rain layer, and increasing its opacity, tremendously reduced the high-frequency window *TB*'s (to 144 K for *TB89* and to 99 K for *TB150*), and continued reducing *TB55* (for a total reduction of about 2.0 K).

*TB31* exhibits very little effect from either rain or ice, so *TB89* and *TB150* scattering effects can be visualized by plotting them against *TB31*. Figure 3.8 depicts *TB89* and *TB150* vs. *TB31* for non-precipitating cases (dashed line) and precipitating cases (points). Figure 3.9 in turn depicts the strong correlation between sounding channel brightness temperature reduction due to precipitation,  $\Delta TB55$ , and window-channel *TB* precipitation reduction.

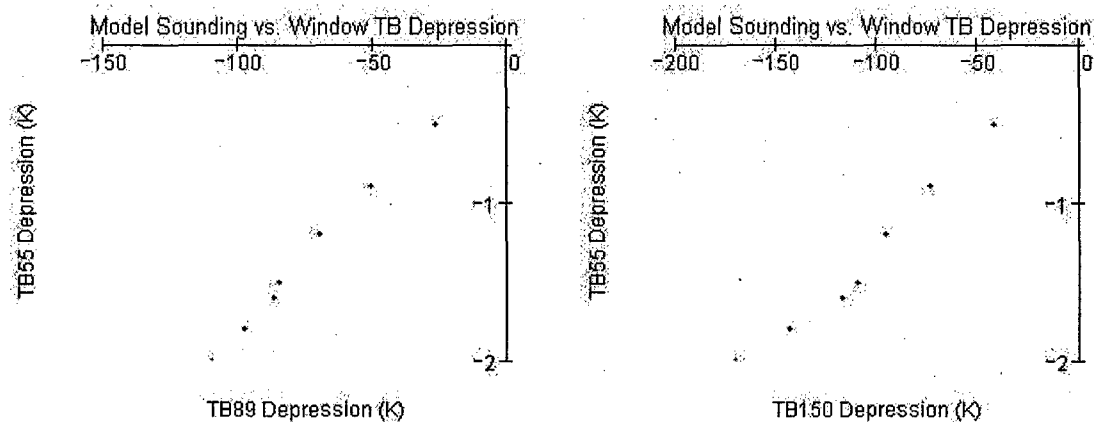


Figure 3.9: Modeled *TB55* depression vs. *TB89* and *TB150* depression for the 10 cases summarized in Table 3.1.

### 3.4. Summary

This chapter has examined precipitation effects throughout the microwave spectrum, with the goal of determining which other AMSU-A or -B frequencies may be useful for quantifying

precipitation effects on the AMSU-A frequencies near 55 GHz used to measure upper-tropospheric temperature. In summary, we have learned that:

- Humidity increases window channel opacity, especially for AMSU-A *TB1* and *TB15* through *TB20*, where humid atmospheres will be opaque
- Cloud droplet scattering is negligible and absorption is proportional to cloud liquid water. Cirrus ice crystals are small enough that they absorb and scatter negligibly in the microwave spectrum.
- Rain emits at low frequencies (*TB1* and *TB2*) and scatters at high frequencies (*TB15* through *TB20*)
- Snow does not significantly affect *TB1* or *TB2* unless it is very thick, in which case it will scatter weakly. Snow can scatter *TB15* through *TB20* significantly.
- Graupel will scatter strongly at all frequencies, but especially for *TB15* through *TB20*.
- The atmosphere is, in general, mostly transparent for window frequencies (*TB1* and *TB2* and *TB15* through *TB17*), so they are sensitive to hydrometeors throughout the vertical column. Thus,  $\Delta TB$  for these frequencies is closely related to the column-integrated liquid and ice water path. For temperature sounding (*TB5* through *TB8*) or moisture sounding (*TB18* through *TB20*) channels, where the atmosphere is opaque due to  $O_2$  and water vapor absorption, respectively,  $\Delta TB$  is only sensitive to hydrometeors that impinge significantly on the weighting function for that channel.

The goal for Chapters 4 and 5 is to develop an empirical scattering correction to AMSU-A sounding channel *TB*'s based on the observed depression of high-frequency window channel *TB*'s. A low-frequency window channel, which is only weakly affected by scattering, will be

used to predict the non-scattering high-frequency window channel *TB*. Principal component analysis will also be explored as a multi-channel tool for predicting sounding channel effects.

#### 4. Simulations of Precipitation Effects on AMSU-A and -B Channels

Chapter 2 noted that the current CIMSS TC intensity algorithm infers *MSLP* from the warm anomaly in *TB7* and *TB8*. The goal of this and the succeeding chapter is to develop a correction for precipitation effects on these channels. The conceptual model in Chapter 3 showed how deep rain layers impinging on these channels' weighting functions can cool *TB* by replacing radiometrically warm emission from the humid lower tropospheric with radiometrically colder (owing to its  $\sim 0.3$  single-scatter albedo) rain emission and reflected cold upper-tropospheric *TB*'s. Frozen precipitation particles in cumulus towers will affect *TB7* and *TB8* more strongly than rain, by virtue of their greater proclivity to scatter ( $\omega \sim 0.9$  for graupel and  $\sim 0.5$  for snow).

Previous studies of precipitation effects on microwave radiation have shown the utility of high-frequency window frequencies (89 GHz and 150 GHz) for quantifying scattering (Grody 1991; Petty 1994; Grody 1999). The conceptual model from Chapter 3 also showed that the scattering-induced *TB* depression at these frequencies correlates with the depression of sounding channel *TB*'s, despite the fact that window channels respond to column integrated liquid and ice quantities, while sounding channels are only affected by liquid and ice within the influence of their weighting functions. The purpose of this chapter is to verify that this relationship holds under more realistic atmospheric profiles of humidity, cloud, rain, snow, and graupel, at actual AMSU-A/B frequencies and scan angles, and with a more rigorous treatment of absorption and scattering.

#### 4.1. Model

Previous studies of microwave precipitation effects (Mugnai et al. 1990; Smith et al. 1991; Mugnai et al. 1993; Smith et al. 1994; Kummerow 1996; Panegrossi et al. 1998; Bauer and Mugnai 2003; Panegrossi 2004) have coupled fine-scale numerical weather prediction (NWP) model output with a radiative transfer model (RTM) using 1-D plane parallel geometry, and (typically) the Eddington two-stream approximation, which considers a single upward and downward intensity stream, each at a fixed incidence angle, and uses a scattering phase function simplified to for the limited number of possible scattering angles.

In the mid-1990's, Petty and other authors introduced Reverse Monte Carlo (RMC) techniques to microwave radiative transfer modeling. The Appendix discusses details of previous RMC models, as well as the one developed for this study. Briefly, RMC models trace photons backward from a sensor through a medium, following them as they are scattered (perhaps multiple times), and ultimately absorbed. RMC models make use of the reciprocity theorem, which postulates that scattering affects photons identically regardless of which direction they are traveling. The same phase function describes the probability of a forward-traveling photon scattering into a given direction or the probability that a scattered backward-traveling photon came from a given direction. Similarly, Kirchhoff's Law allows us to consider the point at which a backward-traveling photon is absorbed to be the point at which the photon would have been emitted had it been traveling in the forward direction.

The nature of RMC models enables any arbitrary 3-D geometry of absorbers and scatterers to be constructed, which eliminates the need for 1-D plane-parallel geometry and limited beam angles. The flexibility and fidelity of RMC techniques to the physical processes

being simulated comes at the price of very large computational expense. Each photon must be tracked backward through possibly many scattering events. Each of those events requires generating a random path length to the next extinction event, randomly determining whether the extinction event results in scattering or absorption, randomly determining the scattering direction, then performing the associated propagation direction transforms, position updates, and absorption point book-keeping. A large number of photons is generally required for the RMC results to converge. Even then, some amount of random noise will still exist in the results. But as computer speed and memory capacity continues to rapidly improve, RMC techniques are becoming more practical. The reason for using in this application is to replicate scattering processes as faithfully as possible and to allow generalization to 3-D geometry.

As discussed in Chapter 3, the Mie extinction and scattering properties for a collection of particles at a point in space can be derived from the precipitation densities at that point. We need to convert these densities to rain rates in order to use the Marshall-Palmer or Siskon-Srivastava empirical size distributions to determine the number density at each particle size. From the particle size spectrum, we can use Mie theory to compute extinction efficiency, single-scatter albedo, and asymmetry parameter or the Mueller matrix elements. The Appendix discusses the five-step process of translating a meteorological profile to Mie properties and then conducting the RMC radiative transfer.

#### **4.2. Data and Methodology**

The goal of this simulation study is to simulate the AMSU-A and -B *TB*'s produced by a number of prescribed dry, humid, warm rain, tropical stratiform, and tropical cumulonimbus

precipitation profiles. Using the modeled *TB*'s, we will compare sounding channel precipitation attenuation with window channel precipitation attenuation. The attenuation is quantified by comparing the simulated *TB*'s at each channel with *TB*'s modeled with rain, snow, and graupel densities set to 0. Petty (2001a) constructed a 1-D cloud model for use with a RMC model to study precipitation effects at Special Sensor Microwave Imager (SSM/I) frequencies and fixed view geometry. The clear/dry, humid, warm rain, and tropical stratiform profiles used in this study are created using Petty's parametric rain cloud model, which uses 19 user-defined parameters, along with detailed aggregation and conversion processes to generate realistic rain, snow, and graupel profiles.

Petty's model considers only droplets falling through still air, and is not intended for convective situations with strong updrafts, where, for instance, supercooled liquid or large rimed graupel particles can be lofted to the upper troposphere. To obtain realistic tropical convective profiles, output from a Mesoscale Model 5 (MM5) simulation of Hurricane Bonnie (1998) was used. This particular simulation was originally run at the NOAA Environmental Technology Laboratory with the purpose of producing simulated radiances for an experimental geostationary infrared sounding instrument. The simulation ran for 96 hours at 3-hour time steps from 0000 UTC 23 Aug 98 to 0000 UTC 27 Aug 98. The model domain is a 297 x 249 horizontal grid with 6.7 km spacing and 59 sigma levels between reference pressure levels of 1000 hPa and 10 hPa. The grid covered roughly 19° to 37° N latitude and 63° to 82° W longitude off the southeastern United States. Version 3.4 of the MM5 was used, with initialization data from the National Center for Environmental Prediction / National Center Atmospheric Research (NCEP/NCAR) Reanalysis Project (NNRP). Physics package options selected for the run were: the Kain-Fritsch

cumulus parameterization, the MRF (Hong-Pan) boundary layer scheme, the Reisner II microphysics scheme (which features supercooled water, slow-melting snow, and graupel riming), and the cloud-radiation scheme. Precipitation output at each grid point consists of bulk densities for rain, snow, and graupel categories, as well as cloud liquid, cloud ice, and specific humidity.

19 different profiles were modeled. For each profile, the RMC model simulated AMSU-A *TB1* through *TB8* and *TB15* for instrument fields of view (FOV's) 1, 5, 8, 11, and 15 and AMSU-B *TB16* through *TB20* for FOV's 1, 11, 22, 33, 45. The channel selection covers all relevant temperature sounding, moisture sounding, and window channels; AMSU-A stratospheric temperature sounding channels (*TB9* through *TB14*) were omitted. The FOV selection is spread evenly across scan angles from edge of scan (approximately  $48 \frac{1}{3}^\circ$  scan angle, producing an

Table 4.1: Simulation Cases

Case	Description	T <sub>sfc</sub> (K)	Z <sub>frz</sub> (km)	Z <sub>trop</sub> (km)	Cld base (km)	Cld top (km)	TPW (kg m <sup>-2</sup> )	CLW (kg m <sup>-2</sup> )	Rain (kg m <sup>-2</sup> )	Snow (kg m <sup>-2</sup> )	Grpl (kg m <sup>-2</sup> )
1	Clear/dry	303	4.4	16							
2	20% RH	303	4.4	16			16.0				
3	40% RH	303	4.4	16			31.9				
4	60% RH	303	4.4	16			47.9				
5	80% RH	303	4.4	16			63.9				
6	100% RH	303	4.4	16			79.8				
7	Warm rain	293	3.1	14	0.5	3.5	32.8	1.0	1.1		
8	Warm rain	293	3.1	14	0.5	3.5	32.8	1.5	2.3		
9	Stratiform rain	303	4.4	16	1.5	7.0	68.1	0.75	2.1	2.3	1.1
10	Bonnie(25) SW	301	6.8	19	1.5	4.5	69.7	0.72	0.33	0.012	0.002
11	Bonnie(25) NW	300	6.4	19	7.0	13.0	77.9	1.6	6.2	3.3	16.6
12	Bonnie(25) Eye	302	8.0	19			88.2	~0	~0	0.91	0.068
13	Bonnie(25) SE	301	6.4	19	1.0	5.0	82.0	0.27	0.057	0.34	0.047
14	Bonnie(25) NE	301	6.1	19	2.0	8.0	82.9	0.82	2.6	0.79	0.67
15	Bonnie(26) W	299	6.2	19	4.0	12.0	85.9	0.62	6.0	1.2	3.2
16	Bonnie(26) Eye	301	7.2	20	0.5	2.0	98.0	0.13	0.007	0.008	0.005
17	Bonnie(26) N	300	6.4	20	0.5	12.5	89.6	1.2	3.5	3.4	2.8
18	Bonnie(26) E	301	6.2	20	1.0	3.0	83.1	0.46	0.039	0.11	0.030
19	Bonnie(26) S	301	6.4	19	0.5	2.0	91.0	0.16	1.4	2.1	0.75

### Case 4: 60% Uniform Relative Humidity; No Precipitation

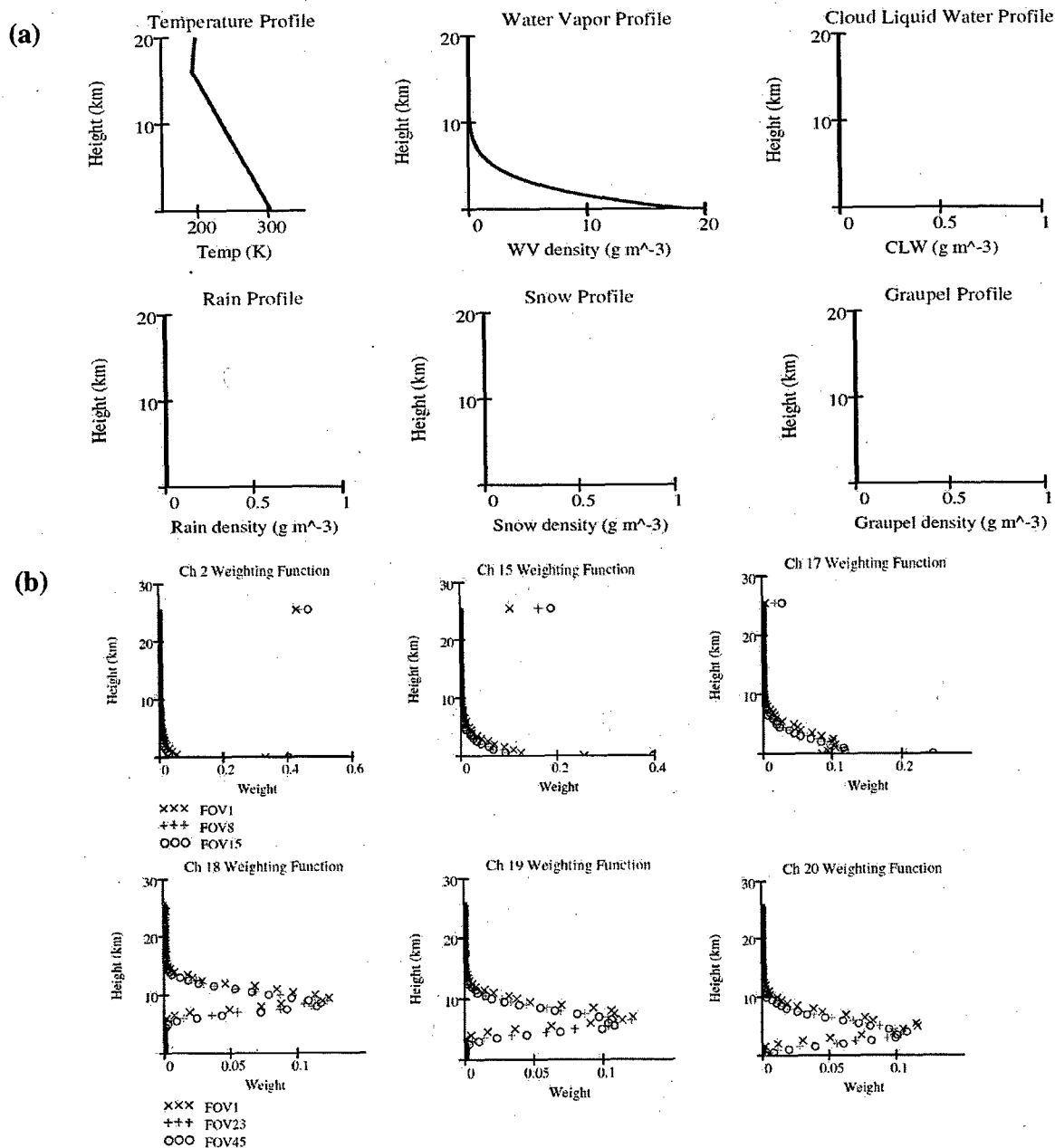


Figure 4.1: (a) Profiles of temperature, water vapor, cloud water, rain, snow, and graupel used for simulation case 4. (b) Resulting window channel weighting functions produced by the reverse Monte Carlo radiative transfer model for AMSU-A channels 2 (31 GHz) and 15 (89 GHz), FOV's 1, 8, and 15 and for AMSU-B channels 17 (150 GHz) and 18-20 (183 GHz), FOV's 1, 23, and 45. The top and bottom level weights indicate the fractional TB contribution of the cosmic background and the ocean surface, respectively.

## Case 8: Warm Rain

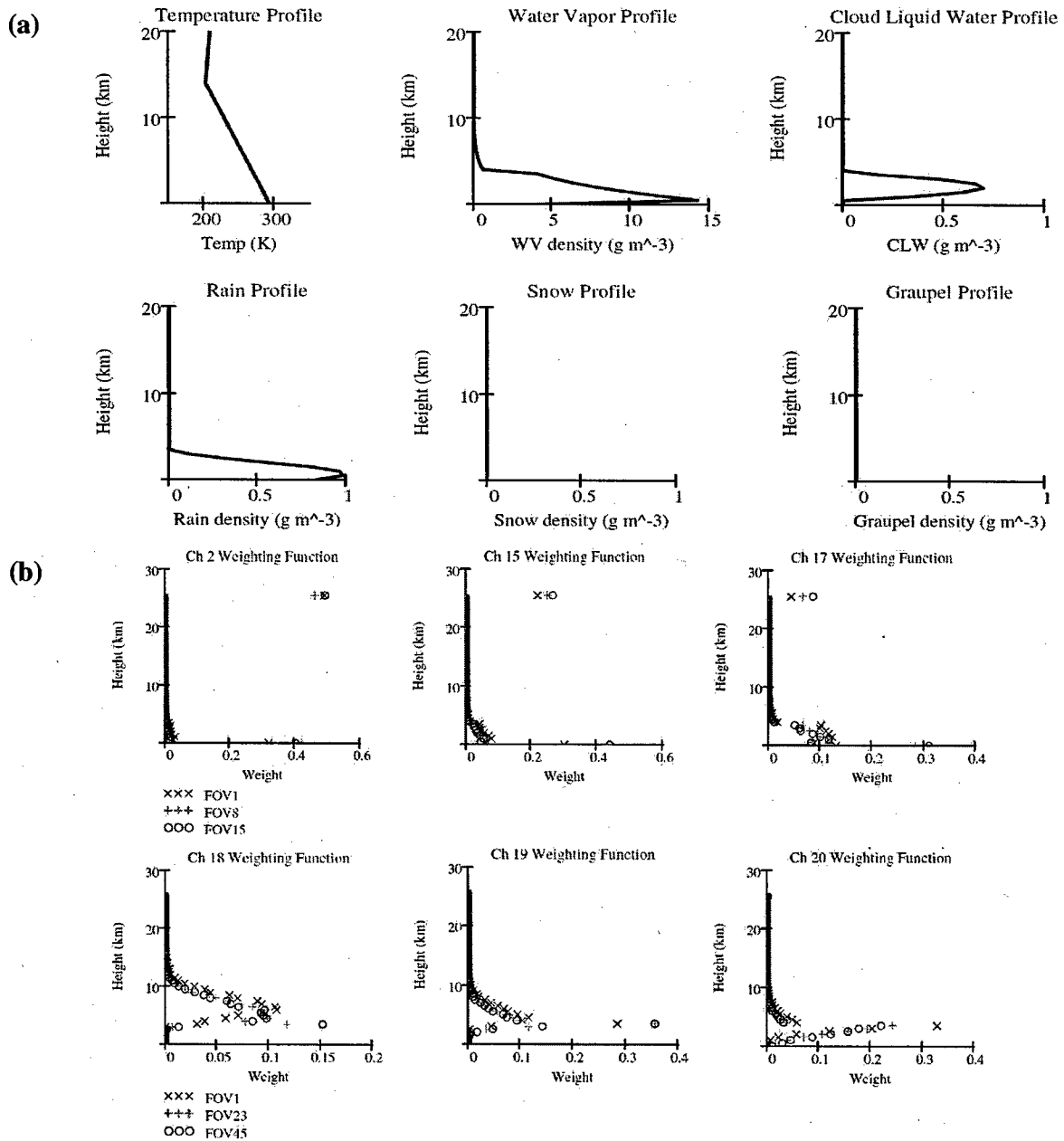


Figure 4.2: Same as Figure 4.1, but for case 8.

### Case 9: Tropical Stratiform Rain

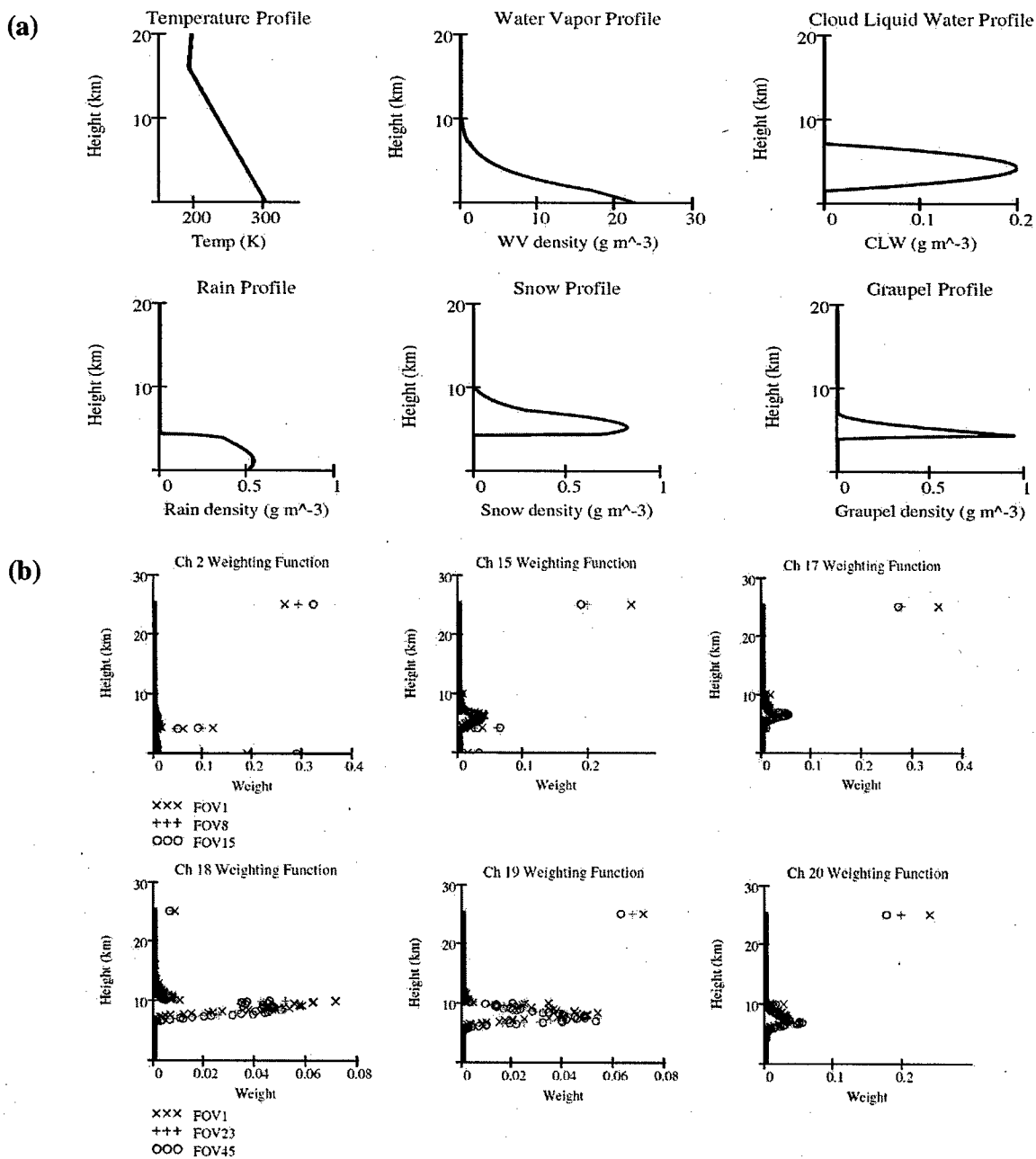


Figure 4.3: Same as Figure 4.1, but for case 9.

Earth-incidence angle of approximately  $60^\circ$ ) to nadir. 5000 photons were used for each channel and FOV combination. The RMC code was run twice for each profile; once with precipitation included and once with rain, snow, and graupel removed (water vapor and cloud were left in place). The precipitation attenuation,  $\Delta TB$ , for each channel is computed by subtracting the non-precipitating  $TB$  from the precipitating  $TB$ .

Table 4.1 summarizes the meteorological conditions for each of the nineteen profiles. Cases 1 through 6 were non-cloudy, non-precipitating scenes with temperature profiles from Petty (2001a) and uniform relative humidity throughout the depth of the atmosphere ranging from 0% (case 1) to 100% (case 6). The top half of Figure 4.1 depicts temperature and water vapor, cloud liquid, rain, snow, and graupel density profiles for Case 4 (60% RH). Profile 7 is the oceanic warm rain profile from Petty (2001a), which consists of a somewhat dry atmosphere with cloud and rain confined below the freezing level. Case 8 (Figure 4.2) is modified to increase the rain rate. Profile 9 is Petty's tropical stratiform rain profile, which has a thick snow and graupel layer extending from the freezing level to 10 km (Figure 4.3).

Figure 4.4 depicts cloud liquid water, column integrated rain water, and column integrated graupel for the MM5 Hurricane Bonnie simulation at 1200UTC 25 Aug 98 and 1200 UTC 26 Aug 98 (60 and 84 hours after forecast initialization). Profiles 10-14 are from 1200 UTC 25 Aug. At this time, the simulated hurricane had an intensity of 958 hPa. Five profiles are arrayed in an "x" around the storm center: Case 10 is the southwest point, located in a relatively clear area; case 11 is located in intense spiral band precipitation to the northwest; case 12 is in the eye; cases 13 and 14 are in spiral band precipitation to the southeast and northeast respectively. Figure 4.5 depicts the profile from the northwest spiral band and contains the

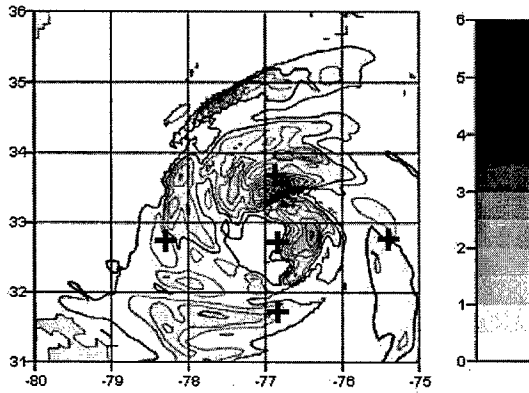
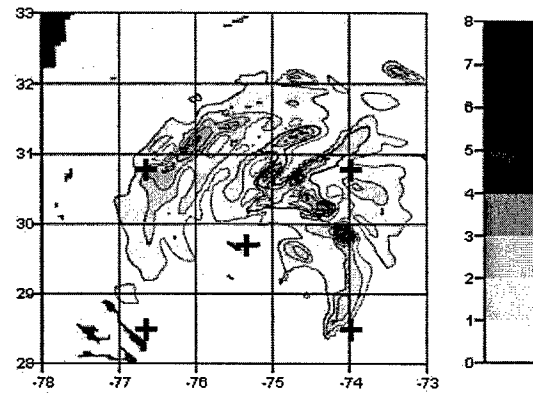
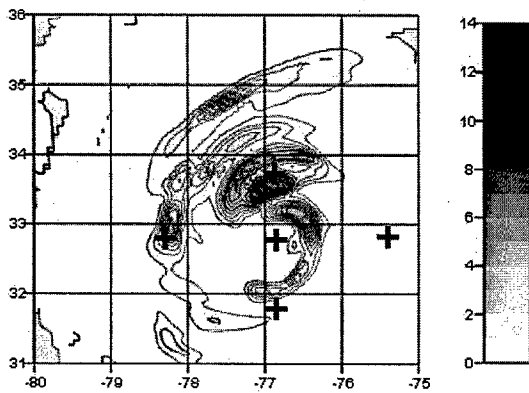
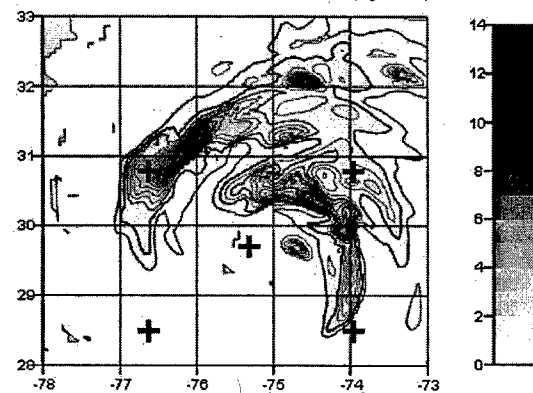
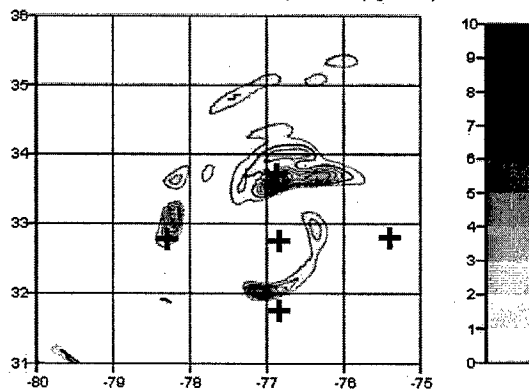
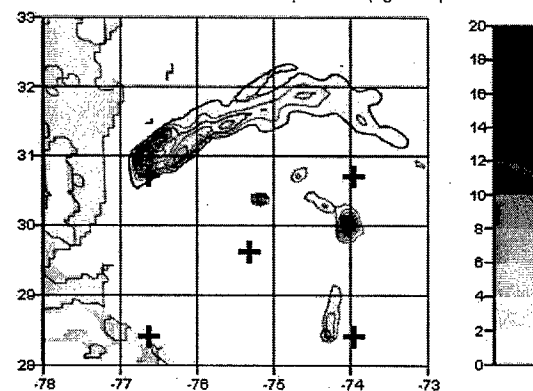
MM5 Bonnie 980826 12UTC Cld Liq Wtr (kg m<sup>-2</sup>)MM5 Bonnie 980825 12UTC Cld Liq Wtr (kg m<sup>-2</sup>)MM5 Bonnie 980826 12UTC Rain Path (kg m<sup>-2</sup>)MM5 Bonnie 980825 12UTC Rain Path (kg m<sup>-2</sup>)MM5 Bonnie 980826 12UTC Graupel Path (kg m<sup>-2</sup>)MM5 Bonnie 980825 12UTC Graupel Path (kg m<sup>-2</sup>)

Figure 4.4: Column integrated cloud liquid water (top), rain (middle), and graupel (bottom) for MM5 simulation of Hurricane Bonnie (1998) at 1200 UTC 25 Aug 1998 (right column) and 1200 UTC 26 Aug 1998 (left column). Bold '+'s indicate grid points selected for simulation cases 10 through 14 (25/12 UTC) and 15 through 19 (26/12 UTC).

### Case 11: Bonnie 1200UTC 25 Aug 98 Northwest Spiral Band

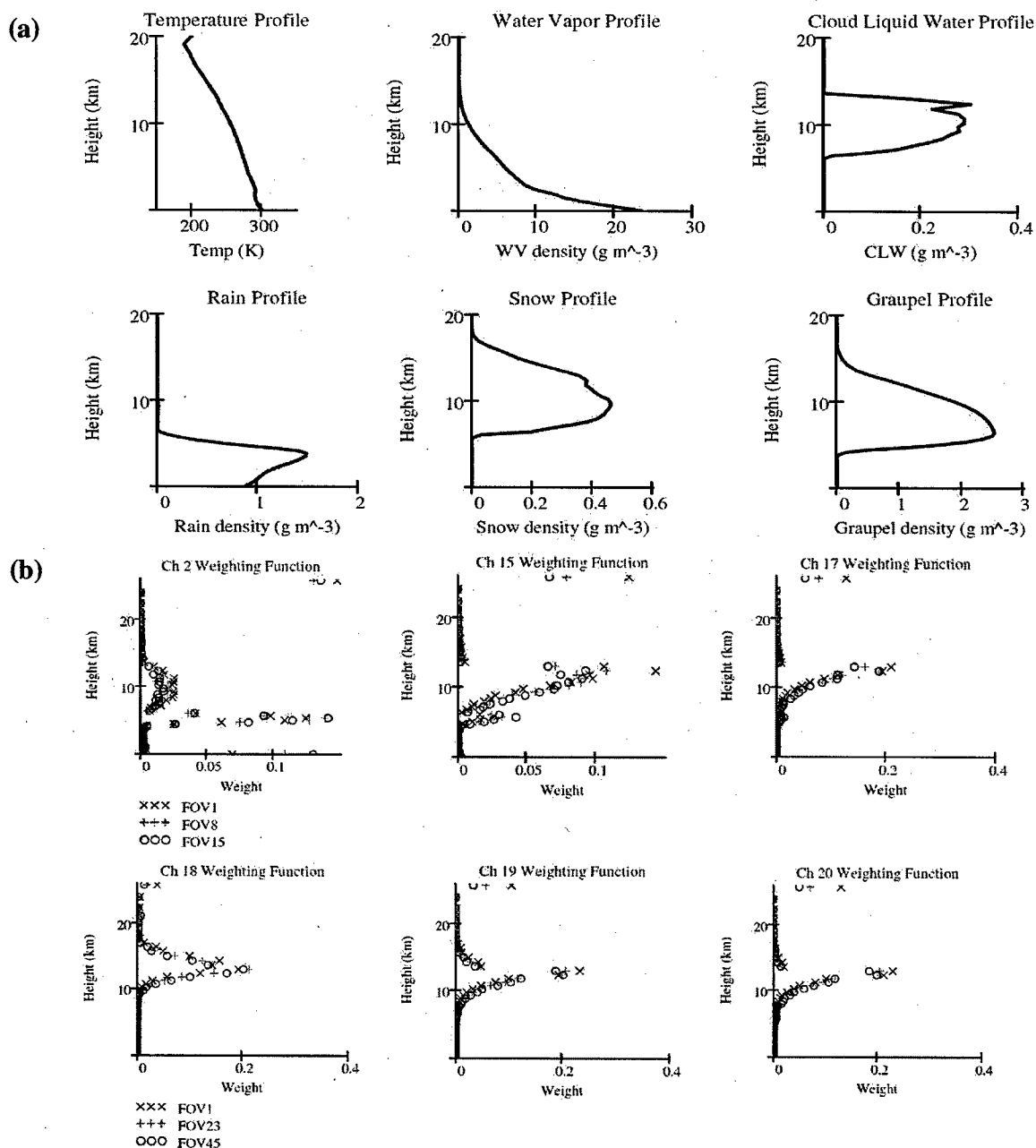


Figure 4.5: Same as Figure 4.1, but for case 11.

### Case 15: Bonnie 1200UTC 26 Aug 98 West Spiral Band

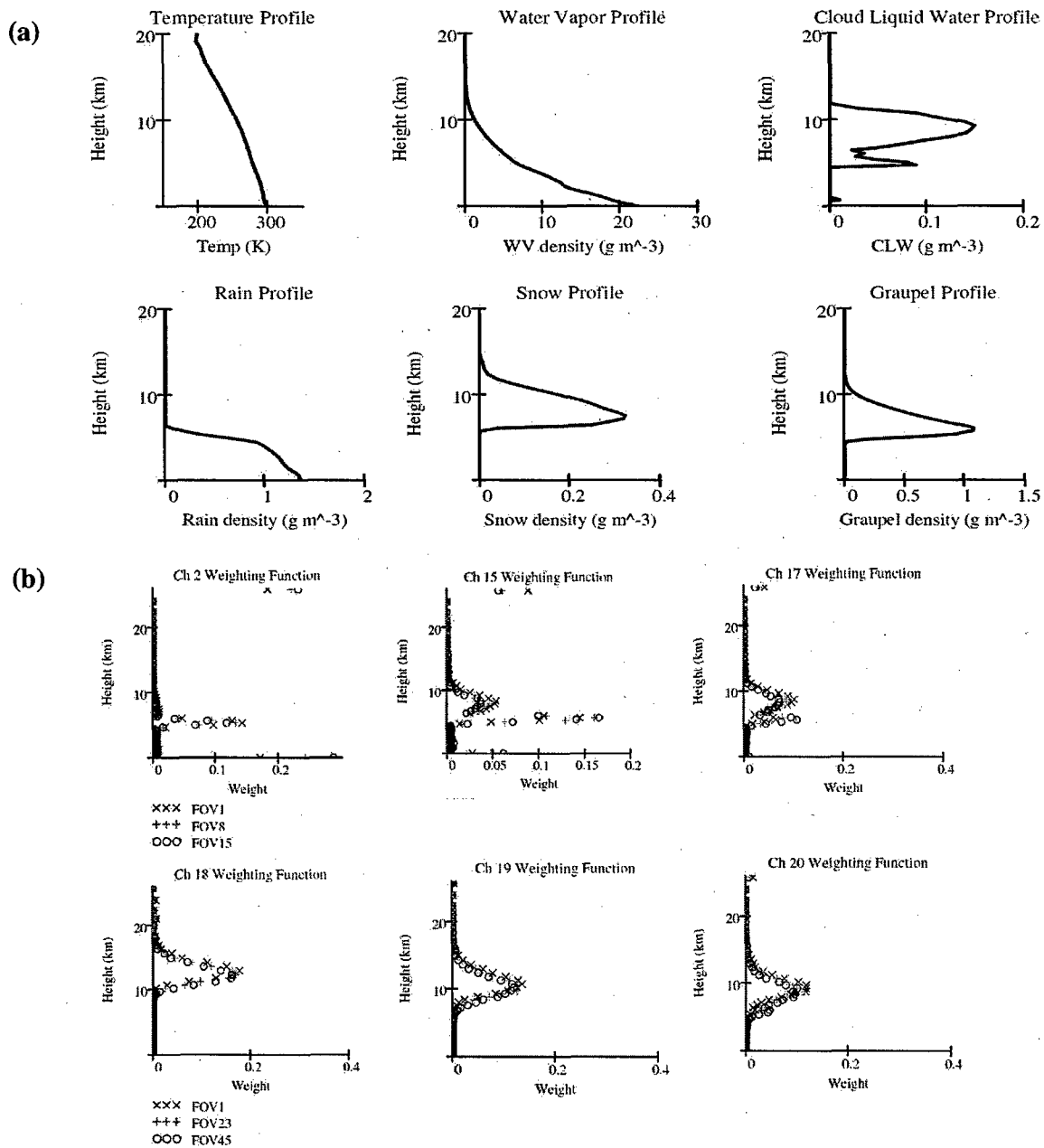


Figure 4.6: Same as Figure 4.1, but for case 15.

heaviest precipitation simulated in any of the cases. Profiles 15-19 are from Bonnie at 1200 UTC on the 26th, when the simulated Bonnie had improved its organization, intensified to 948 hPa, and was nearing landfall. These profiles are arranged in a "+" around the storm. Figure 4.6 depicts the profile from Bonnie's western spiral band, and is representative of spiral band precipitation.

### 4.3. Results

Accompanying each of the profiles in the top halves of Figures 4.1, 4.2, 4.3, 4.5, and 4.6 are the AMSU-A and -B window and moisture channel weighting functions produced by the RMC model from the profile in the top half of the figure. The weighting functions depict the fraction of photons in the RMC model that originate at each level. The weighting functions also include the fraction of photons emitted by the ocean surface or the cosmic background, and include those weights at the bottom and top levels of the function respectively. For window channels in less than opaque conditions, the sea surface and cold space are prime contributors to the observed TB, and the proportions of each correspond to the sea surface emissivity and reflectivity, respectively, matching the frequency and scan angle.

Figure 4.7 depicts *TB15* and *TB17*, the high-freq window channels, vs. *TB1* and *TB2*, the low-frequency windows, for each case and scan angle. Figure 4.8 does the same for *TB18* through *TB20*, the moisture sounding channels. In each plot, the modeled TB with precipitation turned off in the RMC model is depicted as a dot, while the corresponding TB with precip included is plotted with a circle. The dashed arrow tracks *TB* evolution as RH increases from 0% to 100% in the cloud- and precipitation-free cases (1 through 6). The primary effect in these

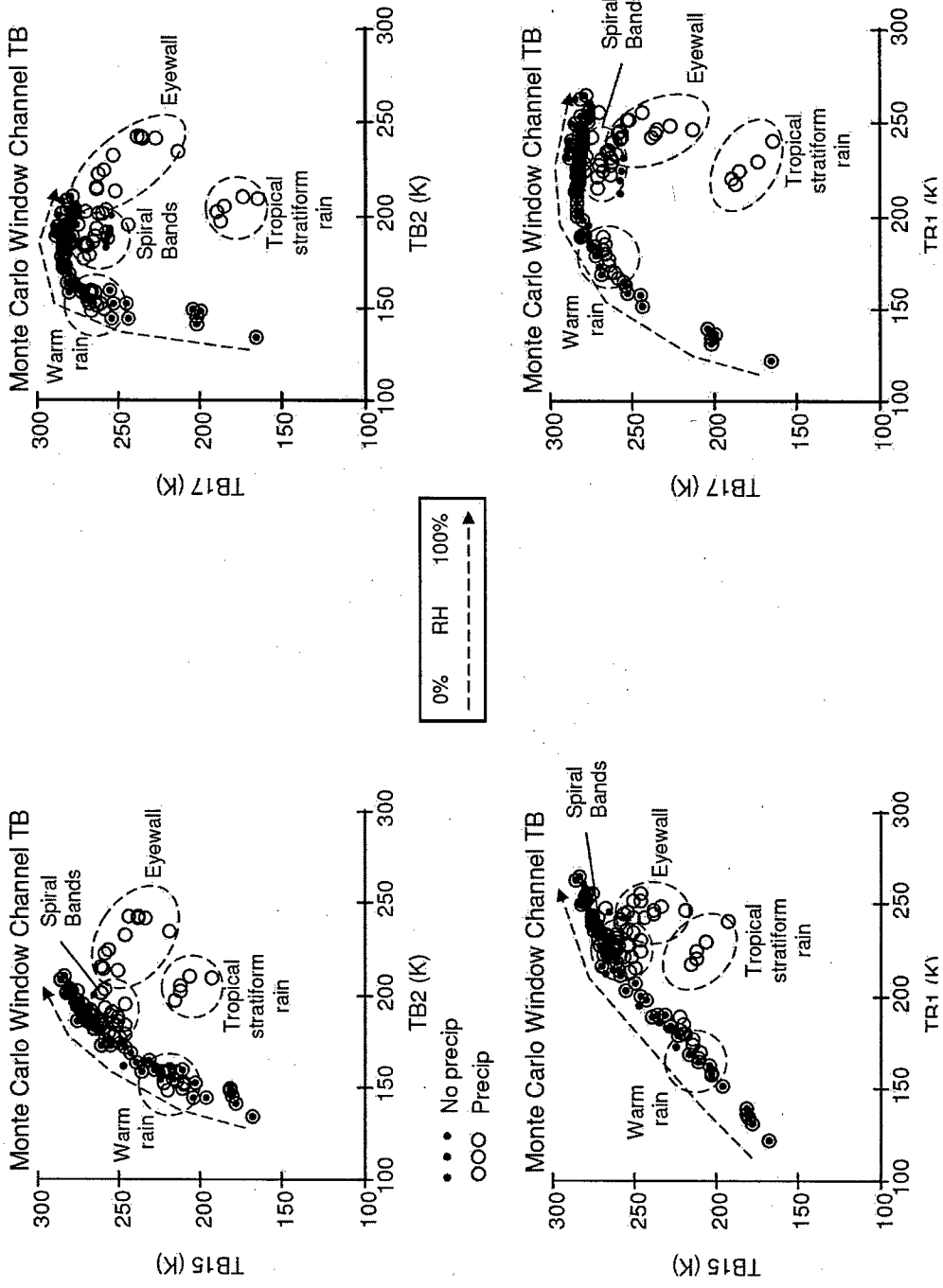


Figure 4.7: Simulated high frequency window channel TB's vs. Low Frequency window channel TB's. AMSU-A TB15 (left column) and AMSU-B TB17 (right column) vs. AMSU-A TB1 (bottom row) and AMSU-A TB2 (top row). Dots indicate TB's modeled with precipitation excluded. Circles indicate precipitating TB's. Dashed arrow follows modeled TB's as relative humidity increases from 0% to 100%. Dashed circles indicated modeled TB's from given types of precipitation.

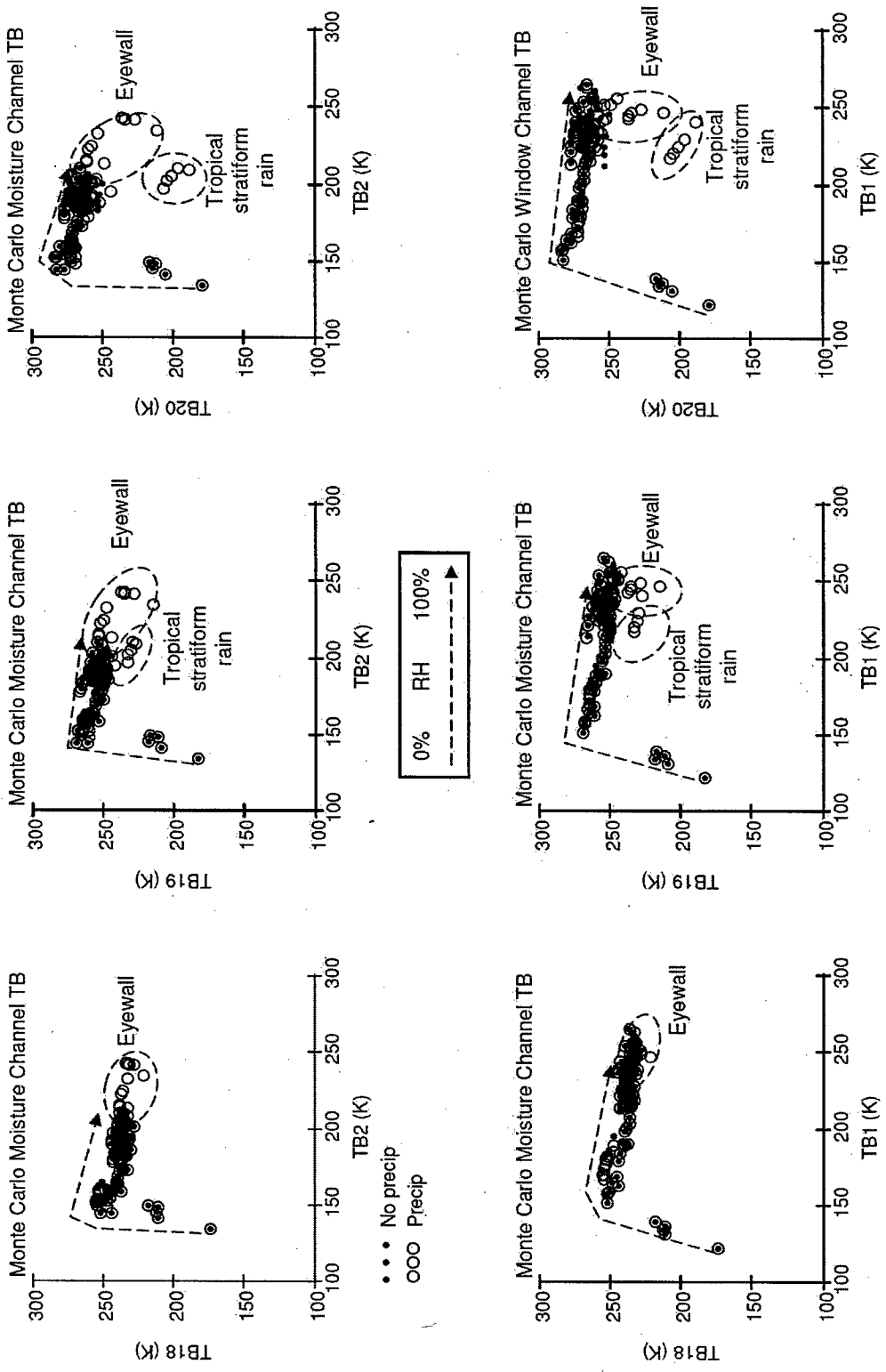


Figure 4.8: Same as Figure 4.7, except for AMSU-B moisture channels, TB18 through TB20, vs. AMSU-A low-frequency window channels, TB1 and TB2.

cases is on *TB18* through *TB20*, for which the atmosphere rapidly becomes opaque (between 0% and 20% RH, as indicated by the large *TB* jump between cases 1 and 2) and their weighting functions stratify with 18 highest (~ 9km), 19 in the middle (~ 7 km), and 20 lowest (~ 4 km). As RH increases, all three of these channels' *TB* decrease due to their weighting functions ascending in the increasingly opaque atmosphere.

*TB17* behaves similarly to *TB20*, since it is strongly affected by water vapor continuum absorption; it rapidly increases with increasing RH to a maximum at around 40% RH, then slowly decreases as its weighting function also ascends. The atmosphere remains slightly transparent to the other high-frequency window channel, *TB15*, which is still increasing as RH reaches 100%.

There is an important difference in the low-frequency window *TB* response to RH increase. *TB1* (23.8 GHz) is near the weak 22 GHz water vapor line, so it is more susceptible to water vapor emission and it increases much more with increasing RH than *TB2* (31.4 GHz). The high-frequency and moisture sounding channels reach their peak values over a smaller range of *TB2* variation, then saturate and remaining relatively flat as *TB2* increases. This should make *TB2* better for predicting no-scatter window and moisture channel *TB*'s because uncertainty in *TB2* will have little/no affect on relatively constant high-frequency *TB* once the atmosphere has become opaque. By contrast, *TB1* and *TB15* or *TB17* increase together nearly linearly, so uncertainty in *TB1* anywhere along its range of values could introduce large uncertainty in predicted no-scatter *TB15* or *TB17* using *TB1*.

The warm rain cases (7 and 8), by virtue of their relatively low RH (TPW close to the uniform 40% RH case) and the thinness of the rain layer, act very similarly to the cases with

increasing relative humidity. They cause no appreciable scattering effect on any channel.

By contrast, the Petty 2001 stratiform rain case (9) introduces significant scattering. It consists of a "snow-generating layer" extending from 10 km down to the cloud top at 7 km. Accretion and conversion processes within the cloud then generate a mixed graupel and snow layer extending down to the freezing level at 4.4 km. Snow melts instantaneously, while graupel takes 0.5 km to melt, creating a bright-band (large graupel particles, with steadily increasing water content, which giving them very large extinction coefficient and moderate single-scatter albedo) near the freezing level. Rain extends to the surface. The combined net effect of these precipitation contributors is an approximately 40 K warming for the low-frequency window *TB*'s due to rain emission. *TB18* is unaffected since the bulk of its weighting function is above most of the snow and graupel. *TB19* is slightly affected, while *TB20* and *TB17* (with their similar weighting function peaks) are hit hardest; both suffer a 70-80 K depression. *TB15* is changed little because the increased scattering *TB* depression caused by the ice-phase precipitation layer is offset by emission from the thick rain layer, which replaces the cold sea surface. This is the first case to exhibit sounding channel *TB* depression. As discussed in Chapter 3, this is due to the reflecting ice layer impinging on the low-level tail of the sounding channel weighting function, replacing warm lower-troposphere emission with reflected cold upper-troposphere emission.

Each of the two Hurricane Bonnie output scenes introduced a variety of profile types. Both had a relatively clear, but humid, profile within the eye and in one or two of the surrounding points. Both scenes also produced profiles with weak to moderate spiral band precipitation. This type of profile produces a 10-20 K increases in *TB2* due to rain emission, a

10-30 K decreases in *TB15* and *TB17* due to scattering, little effect on *TB18* due to the height of its weighting function, modest effects on the remaining moisture channels (~10 K depression in *TB19* and ~20 K depression in *TB20*), and weak low- and mid-tropospheric temperature sounding channel *TB* depression, but little or no *TB8* depression.

The northwestern profile from the 1200 UTC 25 Aug 98 scene (case 11) produced a profile with extremely heavy convective precipitation containing snow as high as 18 km and graupel as high as 15 km. Thick cloud extends from 15 km down to the melting level at around 7 km, and heavy rain lies below. In this case, *TB2* warms to about 240 K, the warmest value seen in any of the simulated profiles, because bright-band emission and opaque rain completely obscure the sea surface. All of the high-frequency channels have sharp peaks in their weighting functions at around 12-13 km in the ice layer, and all of their *TB*'s converge to about 230 K.

That represents *TB* depressions ranging from 10 K (*TB18*) to 60 K (*TB17*). The ice layer extends through all tropospheric temperature sounding channels' weighting functions, including channel 8's, so not surprisingly, this case produced the most significant sounding channel  $\Delta TB$  of the ensemble (0.5 K for *TB8*, 3 K for *TB7*, 8 K for *TB6*, and 18 K for *TB5*).

Figure 4.9 depicts correlation coefficients relating sounding channel  $\Delta TB$  to high-frequency window and moisture channel

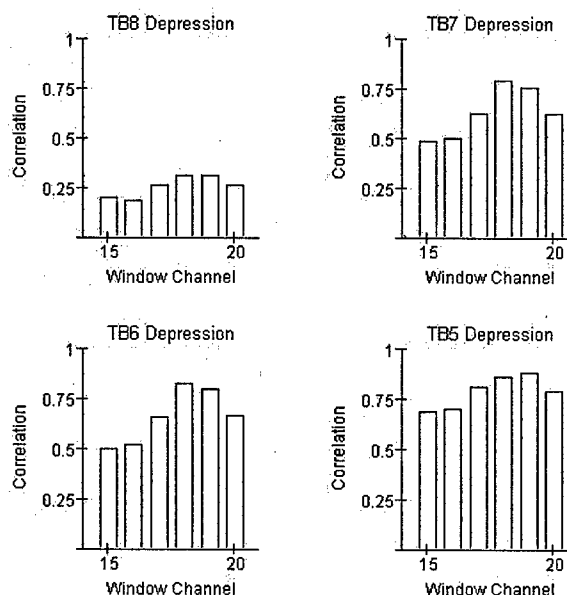


Figure 4.9: Correlations between high-frequency window/moisture channel  $\Delta TB$  and temperature sounding channel  $\Delta TB$ .

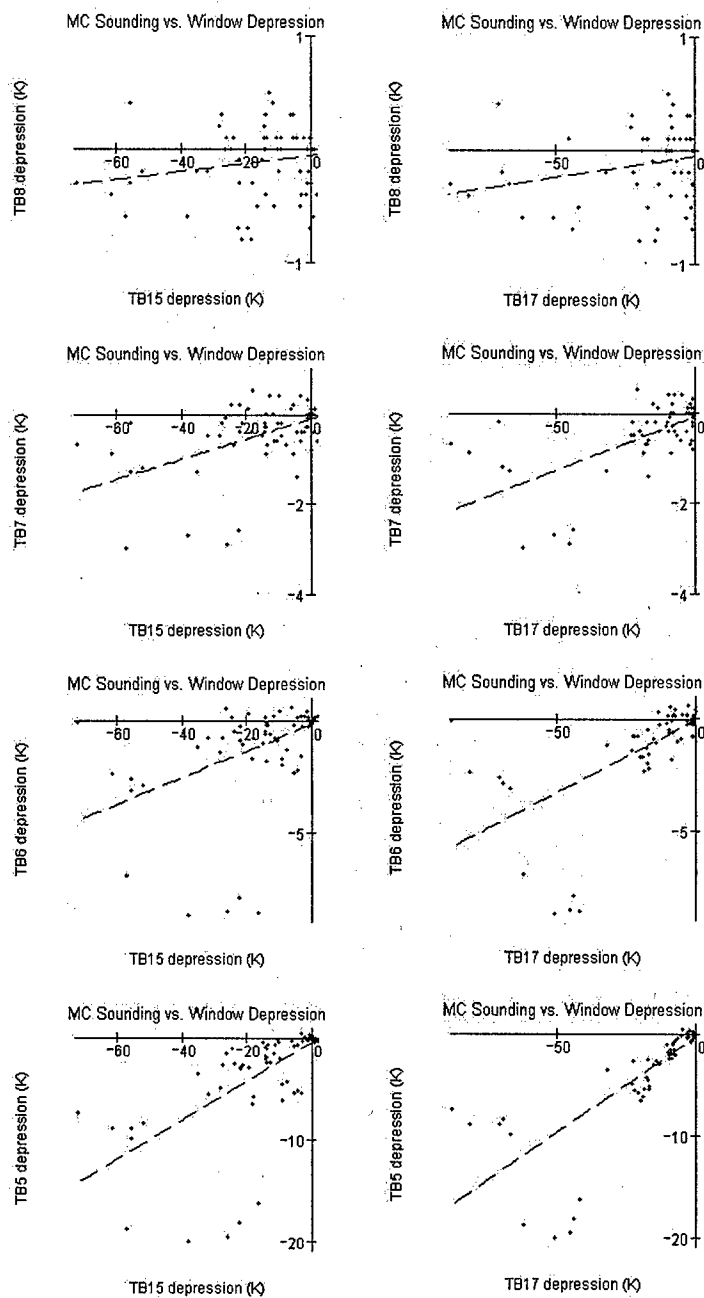


Figure 4.10: Simulated sounding channel scattering depression (dependent variable;  $\Delta TB8$  through  $\Delta TB5$  in rows descending from top) vs.  $\Delta TB15$  (left column) and  $\Delta TB17$  (right column). Correlation coefficients for each combination are shown in Figure 4.9.

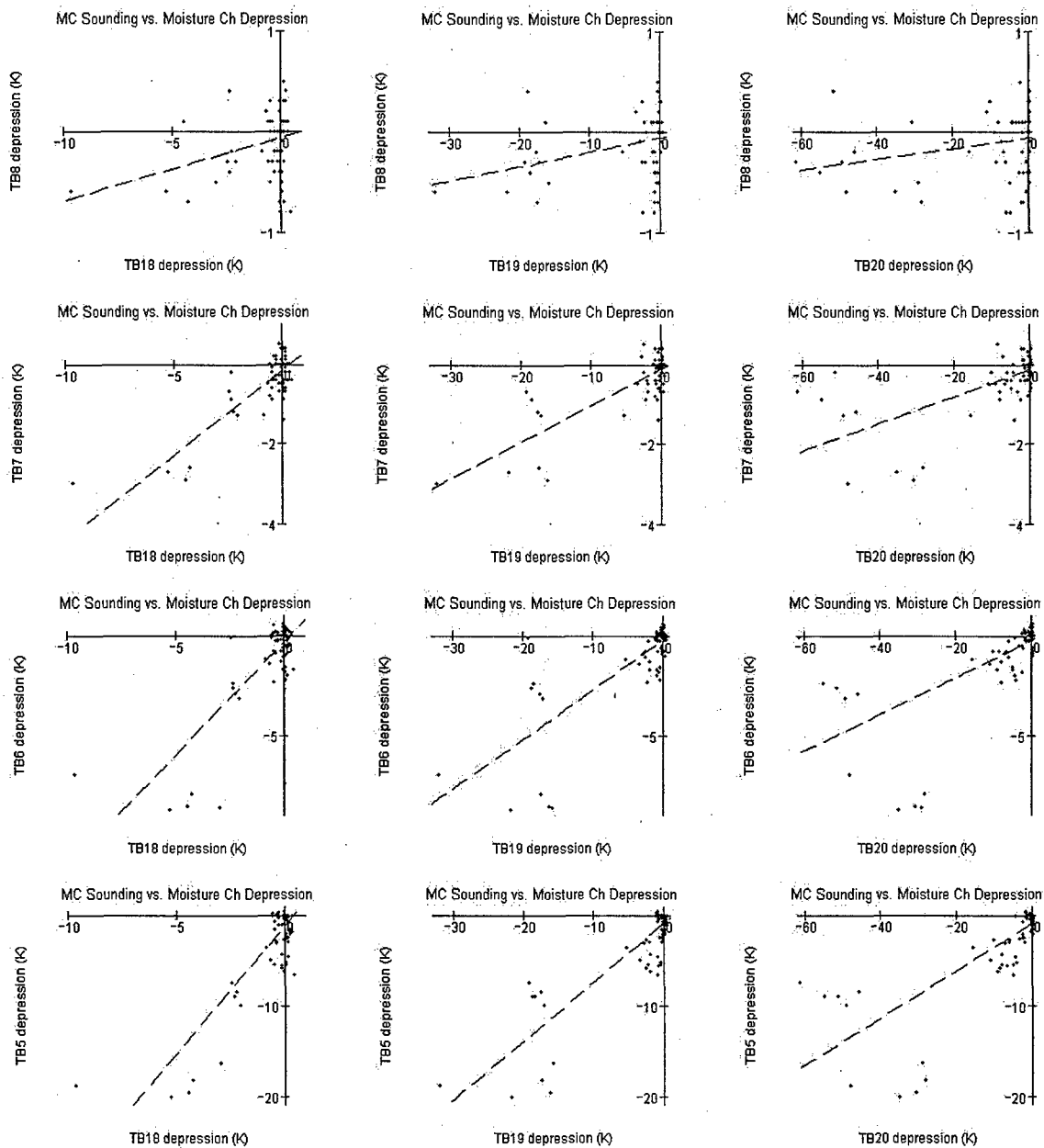


Figure 4.11: Same as Figure 4.10, but with AMSU-B moisture sounding channel scattering depression ( $\Delta TB18$  through  $\Delta TB20$ ) as the independent variable. Correlations with sounding channel  $\Delta TB$  are in Figure 4.9.

$\Delta TB$ . Correlations are uniformly weak for  $\Delta TB8$ , and increase with lower-level channels.

$\Delta TB18$  and  $\Delta TB19$  perform best across the board, with correlations approaching 0.9 for  $\Delta TB5$ .

Figures 4.10 and 4.11 show scattering depression for each of the four sounding channels vs. both high-frequency window channels' (4.10) and all three moisture sounding channels' (4.11)  $\Delta TB$ .

Least-squares best-fit lines are superimposed.

Bauer (2001) and Petty (2001) demonstrated that principal component analysis was useful for isolating multi-channel precipitation effects. Figure 4.12 depicts the first empirical orthogonal function ( $EOF1$ ) of the standardized  $\Delta TB$  for the combined set of low-frequency, high-frequency, and moisture channels ( $\Delta TB1$ ,  $\Delta TB2$ , and  $\Delta TB15$  through  $\Delta TB20$ ). This EOF explains 72% of the variation in the data set. The sign of an EOF's elements is arbitrary, since the sign of the corresponding principal components is chosen to produce the correct physical result. What is important is the relative magnitude of each element, and the sign of that individual element with respect to the rest. For this EOF,  $\Delta TB1$  and  $\Delta TB2$  are the opposite sign of  $\Delta TB15$  through  $\Delta TB20$ . This is consistent with rain emission warming the low-frequency window  $TB$ 's and scattering reducing the high-frequency  $TB$ 's. Figure 4.13 depicts  $\Delta TB$  for each sounding channel vs. the first principal component of the combined window channel  $\Delta TB$  set with accompanying correlations. Results are similar to using an individual high-frequency channel  $\Delta TB$ . The correlation with PC1 decreases from about 0.9 for  $\Delta TB5$  to about 0.3 for  $\Delta TB8$ .

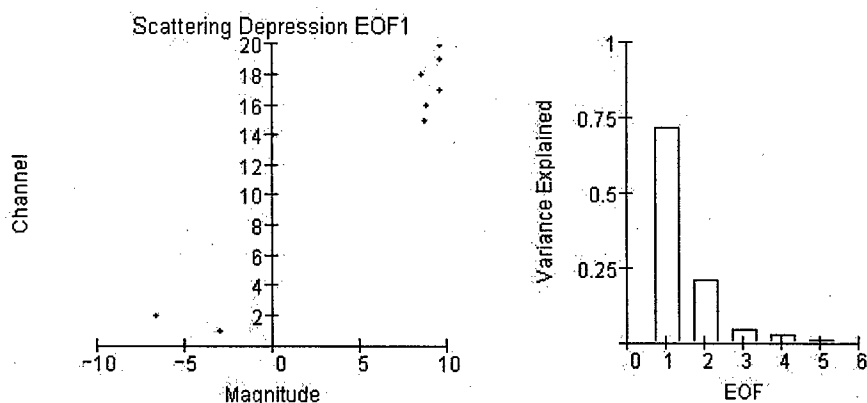


Figure 4.12: Leading EOF (left) of simulated window and moisture channel  $\Delta TB$ . Opposing sign of TB1 and 2 vs. TB15-20 is consistent with rain emission warming TB1 and 2 while scattering reduces TB15-20. Variance explained by the 6 leading EOF's of window and moisture channel  $\Delta TB$ . EOF1 explains 72% of the multi-channel variance.

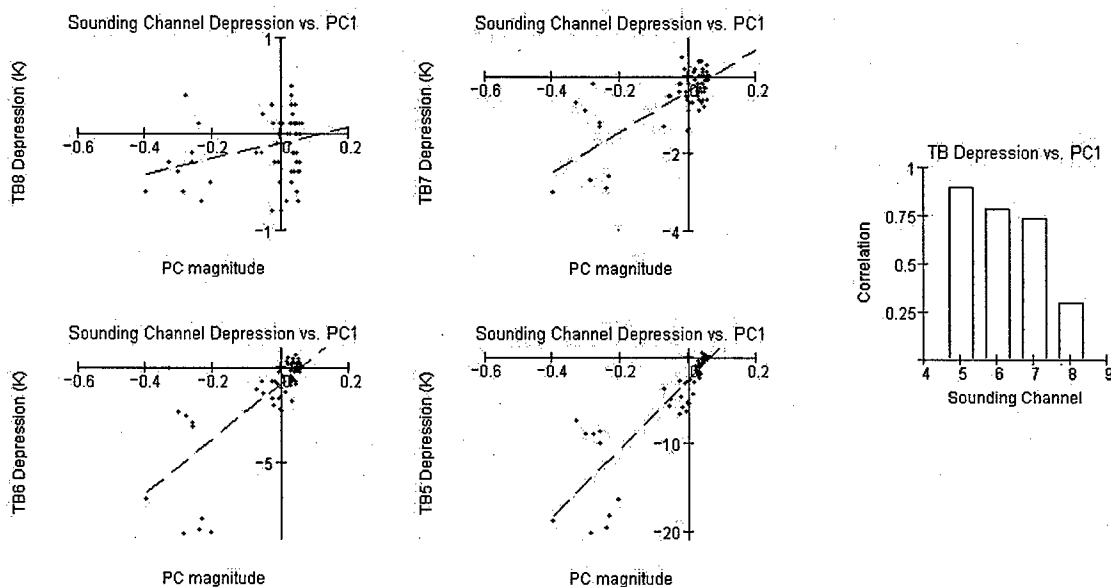


Figure 4.13: Simulated sounding channel  $\Delta TB$  vs. the leading principal component of window or moisture channel  $\Delta TB$  (corresponding to *EOF1* in Figure 4.12). Correlations with each sounding channel  $\Delta TB$  (at right) are comparable to correlations achieved using  $\Delta TB18$  or  $\Delta TB19$  alone.

#### 4.4. Discussion

The flatter curves for high-frequency and moisture channel  $TB$  vs.  $TB2$  indicate that  $TB2$  is probably a better choice than  $TB1$  to use for predicting the no-scatter high-frequency  $TB$ 's.  $TB1$  responds strongly to both humidity variation and rain emission, while  $TB2$  is much less sensitive to humidity. Since we are interested only in precipitation effects, excluding  $TB1$  humidity variation as a source of uncertainty in predicted no-scatter high-frequency  $TB$ 's should increase their accuracy.

The best correlated high-frequency  $\Delta TB$  for each sounding channel  $\Delta TB$  is either  $TB18$  or  $TB19$ . However, it is significant to point out that the no-scatter  $TB$  values are known exactly in these simulation cases.  $TB18$  depressions are very small (10 K at most), so it is doubtful--given the uncertainty in no-scatter high-frequency  $TB$ 's predicted using  $TB2$ --that in practice the no-scatter  $TB18$  can be estimated with that degree of accuracy.

Principal component analysis clearly highlights the multi-channel scattering signature, but because of the redundancy of information provided by the scattering-sensitive high-frequency channels, the first PC doesn't perform significantly better than a single high-frequency channel for predicting sounding channel  $\Delta TB$ .

These results suggest that correcting  $TB8$  for precipitation scattering effects is going to be problematic. Simulated scattering  $\Delta TB8$ 's were on the same order as the Monte Carlo statistical noise, which suggests that scattering effects on channel 8 may not be discernable from real-world sources of noise. The  $TB8$  weighting function peaks near 15 km at nadir (higher at edge of scan), so even in vigorous eyewall convection, it is difficult for a significant number of frozen hydrometeors to impact this channel significantly (just as it is difficult to affect  $TB18$ , which also

peaks very high in the troposphere in humid conditions). A promising approach may be to use moisture channels that peak near the same level to correct individual sounding channels, i.e. *TB18* to correct *TB7* and *TB8*, *TB19* to correct *TB6*, and *TB20* to correct *TB5*.

The simulations in this chapter support the hypothesis from Chapter 3--namely, that precipitation scattering depression of sounding channel *TB*'s can be quantified by using the depression in high-frequency window or moisture sounding channels. It appears that *TB2*, which is only weakly affected by scattering, will allow prediction of high-frequency no-scatter *TB*'s, from which scattering depression can be determined. Then sounding channel  $\Delta TB$  can be inferred, and corrected for, by using the empirical relation between high-frequency and sounding channel  $\Delta TB$ . The next chapter presents analysis of observed AMSU-A and -B data and develops such a correction technique, which is then used in Chapter 6 to improve TC intensity estimates.

## 5. Developing an Empirical Scattering Correction

The conceptual model presented in Chapter 3 suggested using a low-frequency window channel to predict high-frequency window or moisture channel non-scattering  $TB$ , in a manner similar to the Grody (1991, 1999) scattering index. The simulation study in Chapter 4 demonstrated that scattering-induced high-frequency window or moisture channel  $TB$  depression ( $\Delta TB$ ) from predicted no-scatter values is proportional to sounding channel  $TB$  depression due to precipitation. The simulation results also suggest that  $TB_2$  would be a better low-frequency predictor of high-frequency no-scatter  $TB$  and that  $\Delta TB_{18}$  or  $\Delta TB_{19}$  might be the best predictors for sounding  $\Delta TB$ .

This chapter will apply those concepts to a large set of observed AMSU data to verify them in practice and develop an empirical correction for sounding channel precipitation effects. Chapter 6 will apply the correction technique and validate the performance of scattering-corrected  $TB$ 's in the CIMSS AMSU-based  $TC$  intensity estimation technique.

### 5.1. Data and Methodology

Since a  $TC$ 's upper-tropospheric warm anomaly may be on the order of 10 K, and the simulated scattering effect on AMSU-A sounding channels was typically on the order of 0.1 to 10 K, it will be difficult to isolate the  $TB$  reduction caused by scattering if observed only near  $TC$  centers. So this chapter begins with an analysis of AMSU-A and -B data from tropical scenes without a  $TC$  present.

For this analysis, four days of archived AMSU data are used: 01 Jan, 01 Apr, 01 Jul, and 01 Oct 2003. Three AMSU instruments were operational at the time, flying on the NOAA-15, -

shape for each AMSU-B FOV in the 3 x 3 array with the AMSU-A 3 1/3°-width Gaussian beam centered at the middle of the array produces each AMSU-B FOV's relative contribution to a synthetic AMSU-A resolution FOV. The corner points of the 3 x 3 AMSU-B array contribute 0.096 each to the convolved *TB*, the edge points contribute 0.118, and the center FOV contributes 0.144. For all further analysis, AMSU-B data is first convolved to AMSU-A resolution.

### ***5.1.2. Limb Correction***

Limb darkening, the decrease in *TB* with increasing scan angle for tropospheric sounding channels, is caused by the longer slant path traveled through the absorbing atmosphere. This effect can reduce observed *TB* by as much as 10 K from nadir to edge of scan as the weighting function ascends to approximately the level of the next higher channel at nadir (for example, the channel 7 weighting function--which peaks at approximately 250 hPa at nadir--peaks at about 150 hPa at edge of scan, the same level at channel 8 at nadir; see Figure 2.15). In order to maintain uniform sensitivity to a fixed atmospheric level across the full AMSU-A scan, a limb correction technique must be employed, and the CIMSS AMSU-based TC intensity algorithm follows the one developed by Goldberg et al. (2001). For each channel and FOV, a synthetic limb-corrected *TB* is produced using a weighted sum of the channel and its neighbors above and below. Goldberg et al. (2001) derived the coefficients of the weighted sum using a large sample of AMSU data stratified by latitude, ocean or land surface, and time of year. The standard deviation of the resulting limb-corrected *TB*'s is within the instrument noise. The limb-correction coefficients can be thought of as constructing a synthetic weighting function that maintains its approximate shape and peak height across the scan line. By using limb-corrected

sounding channel *TB*'s, the CIMSS TC algorithm ensures that a channel remains sensitive to temperatures at a nearly constant level, regardless of scan angle. For this analysis, using limb-corrected sounding *TB*'s ensures that their sensitivity to hydrometeors will remain relatively constant across the scan line as well.

Goldberg et al. (2001) were also able to produce limb-correction coefficients for the window channels. This is less straightforward than for sounding channels because the window channels usually have a strong surface contribution and each has a different response to humidity. The authors chose channels 1, 2, and 4 as contributors to the limb-correction for *TB1* and *TB2* and channels 2, 3, and 15 as contributors to limb-corrected *TB15*. This study, however, intends to use each channel's unique response to moisture, cloud, rain, and ice. Blending multiple window channels by way of limb correction will mix these effects to different degrees at different scan angles, complicating the task of quantifying scattering.

A final note about limb correction: the coefficients derived by Goldberg et al. (2001), and used in operations by the CIMSS TC intensity technique, produced a large amount of noise (1 to 2 K) from FOV to FOV across a scan line. The underlying raw brightness temperatures all vary smoothly across the scan line, indicating that the noisiness is produced by the limb correction coefficients. The noise in channel 8 is on the same order as the expected *TB* precipitation perturbation predicted by the simulation results in Chapter 4. For this reason, new limb-correction coefficients were derived for the sounding channels using this data set. The resulting coefficients for channel 8 are considerably smoother and reduce the FOV to FOV noise. Those limb coefficients are used to limb-correct AMSU-A sounding channels for all analyses in this and the subsequent chapter.

16, and -17 spacecraft (NOAA-17's AMSU-A has since failed). Each day's data includes AMSU-A and -B scan lines which are completely over ocean and confined between 15° S and 15° N latitude. The over-ocean requirement eliminates any effects of land-surface emissivity on the results. The latitude bounds were chosen to minimize the effect of tropopause height variation on the results, particularly for AMSU-A channel 8, which is sensitive to temperature in the upper troposphere near 150 hPa. The full sample contained 375,325 individual fields of view (FOV). After the initial analysis using the TC-free tropical data, a second analysis was conducted for comparison, using 30 FOV x 30 FOV boxes centered on TC's from the 2003 Atlantic hurricane season. This additional data set contained 112,500 FOV's from 125 different TC scenes.

#### ***5.1.1. AMSU-B to AMSU-A Convolution***

Since AMSU-B has 3 times finer resolution than AMSU-A, some method needs to be used to convolve AMSU-B brightness temperatures from their native resolution to the same resolution as the AMSU-A FOV's with which they will be used. Bennartz (2000) demonstrated a convolution method using a Backus-Gilbert technique on observed AMSU-B data. The resulting convolution coefficients account for both the instrument resolution differences as well as asymmetries in instrument response across the scan line.

The convolution approach used for this analysis is simpler and does not account for variation in antenna response and co-location across the instruments' scan lines. AMSU antenna patterns consist of a strong main lobe centered on the instrument line of sight, with half-power beam-widths of 3 1/3° for AMSU-A and 1.1° for AMSU-B. Each AMSU-A FOV corresponds to a 3 x 3 array of AMSU-B FOV's. Convolution of the 2-dimensional 1.1°-width Gaussian beam

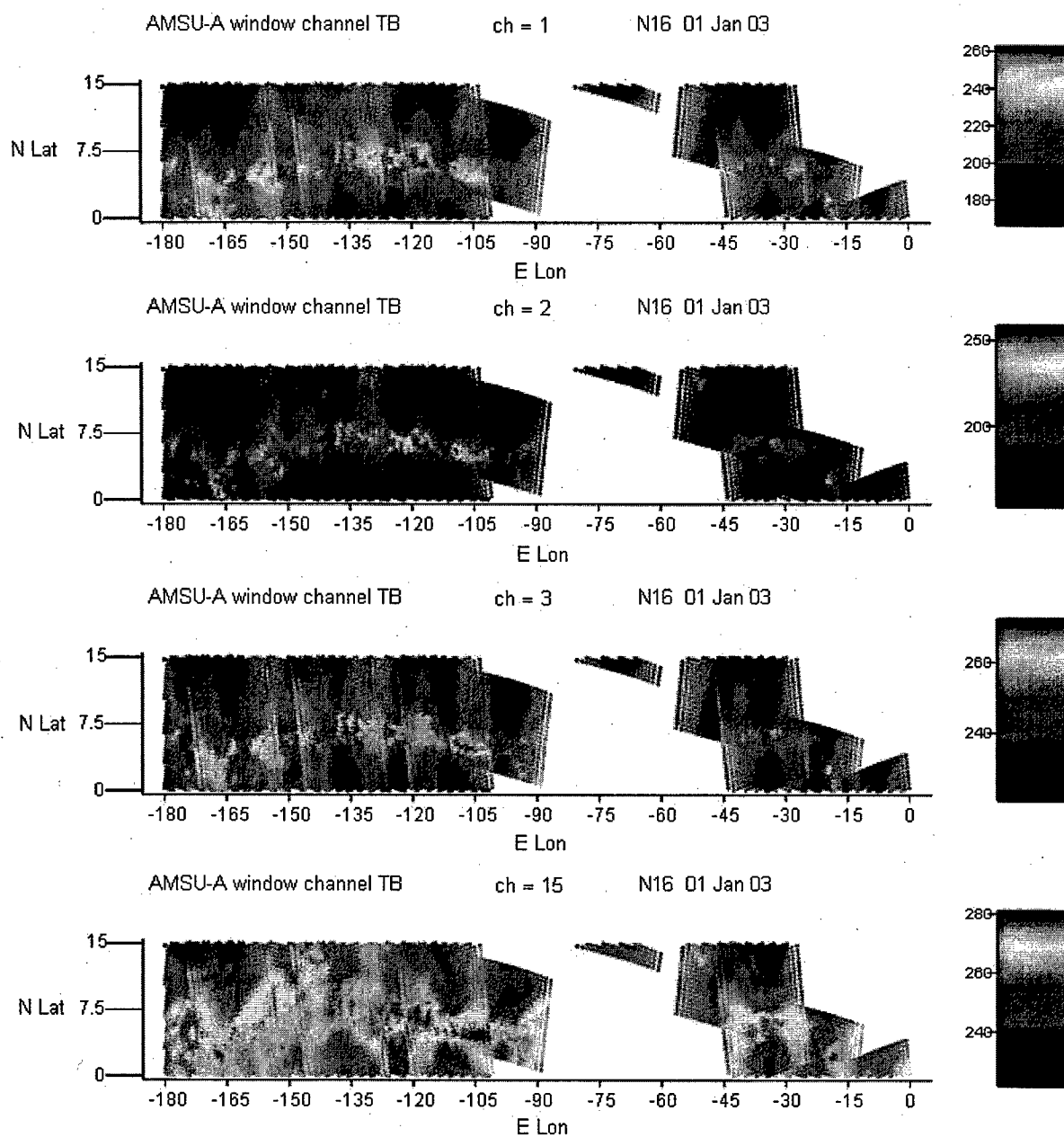


Figure 5.1: AMSU-A window channel (*TB1*, *TB2*, *TB3*, and *TB15* from top to bottom) brightness temperatures (in K) from NOAA-16 on 01 Jan 03.

## 5.2. Results

Figures 5.1 through 5.4 are images of AMSU *TB*'s from one satellite (NOAA-16) on one of the four days (01 Jan 03) for the western hemisphere. Five ascending orbits and seven descending orbits throughout the day are merged to form a single image, which accounts for the discontinuities in the images. A scan line is only used if it is completely over ocean (a requirement driven by the limb-correction development process), so large swaths of data are missing around South America and Africa.

Figure 5.1 depicts AMSU-A window channels: 1, 2, 3, and 15. A *TB* gradient from nadir to edge of scan is evident for each channel. It is caused by limb effect in the humid tropical atmosphere. *TB1* and *TB15* are very sensitive to humidity, so strong meridional gradients are observed in these channels approaching the convection in the intertropical convergence zone (ITCZ). *TB2* is relatively unaffected by humidity so it exhibits a very sharp *TB* gradient at the edge of the ITCZ precipitation. *TB3* is more difficult to interpret because it is sensitive to lower-tropospheric temperature, in addition to sea surface emission and humidity. It is not particularly useful for our purpose of predicting high-frequency *TB*. The strong mesoscale convective system (MCS) affects several FOV's near 7° N 120° W and offers a good example of the multi-channel scattering signature. It exhibits a strong warm signal in *TB2*, which contrasts sharply with the strong depression in *TB15*. Discussion of the following images will focus on this MCS.

Figure 5.2 shows limb-corrected AMSU-A temperature sounding channels. *TB4* has strong surface sensitivity, so rain emission blocks the radiometrically cold sea surface (as well as possibly increasing sea sfc emissivity as falling rain roughens it) The MCS causes about 5 K depression in *TB4*. The *TB5* weighting function peaks near 700 hPa, and it contains a small, but

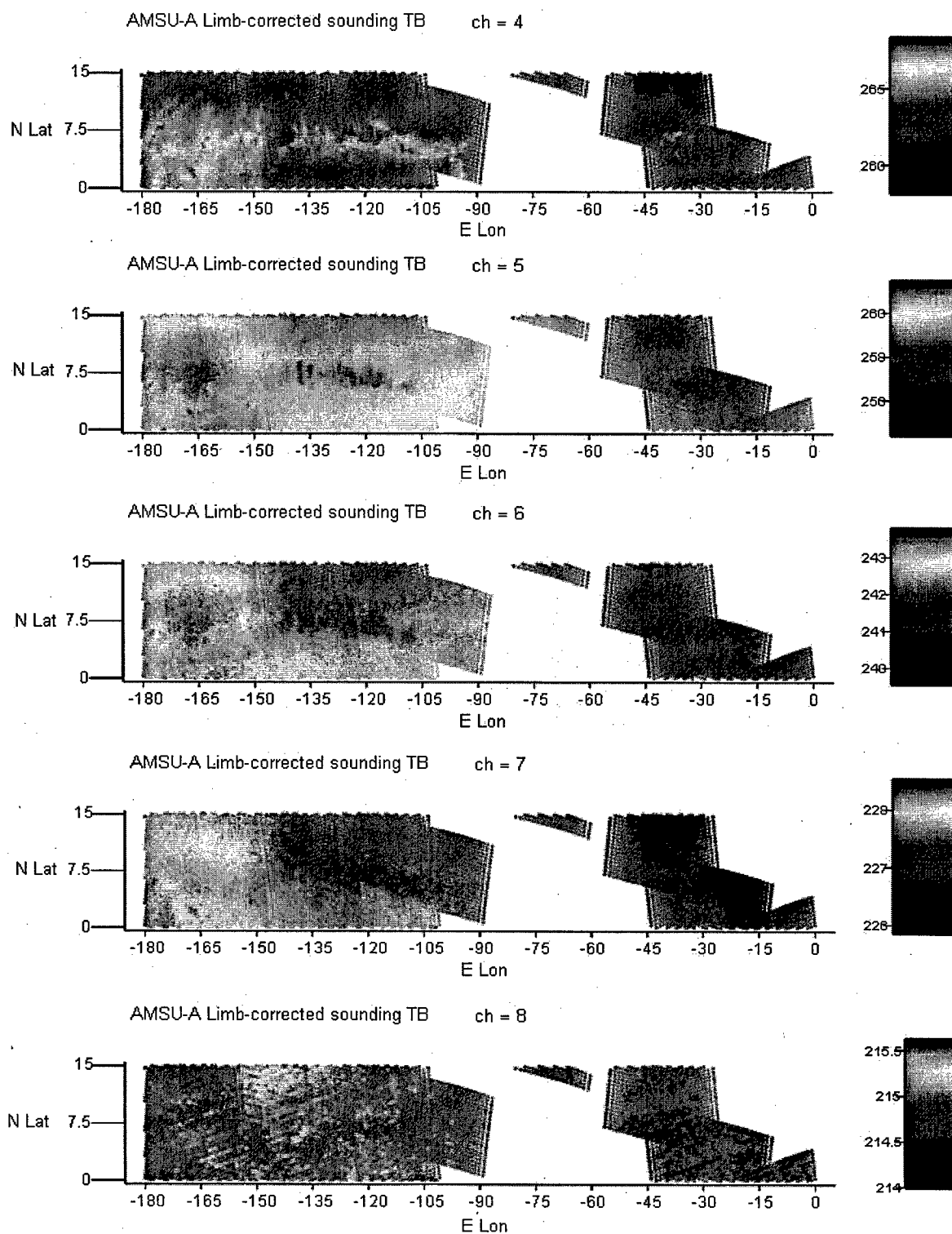


Figure 5.2: AMSU-A temperature sounding channels (*TB4* through *TB8* from top to bottom), NOAA-16, 01 Jan 03.

non-negligible, surface component. Some rain warming is evident in this channel, as well as about 2 K of scattering *TB* depression by the MCS. *TB6* is sensitive to 400 hPa and has no surface contribution. Zonal *TB* variation becomes the largest source of variability for this and higher sounding channels. The MCS causes about 1.5 K scattering depression. *TB7* (250 hPa) suffers a 1 K reduction by the MCS. Whatever scattering effect is present in *TB8* is lost among about the approximately 0.5 K of noise in the scene, consistent with Chapter 4's conclusion that scattering effects on *TB8* will be hard to quantify.

Figure 5.3 depicts AMSU-B window channels (*TB16*, 89 GHz, and *TB17*, 150 GHz) convolved to AMSU-A resolution. While they use the same frequency, the convolved AMSU-B *TB16* is about 10 K colder than AMSU-A *TB15* in scattering areas due to better ability of AMSU-B to resolve finer details that get smoothed by AMSU-A resolution. Even after

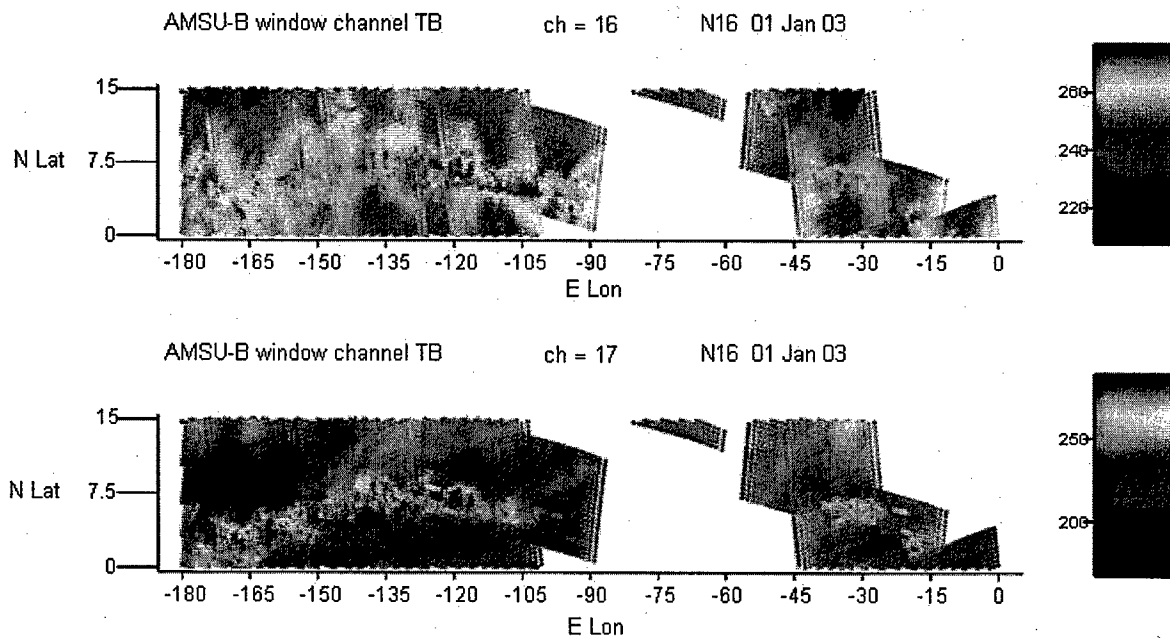


Figure 5.3: AMSU-B window channels (*TB16* and *TB17* top to bottom) convolved to AMSU-A resolution.

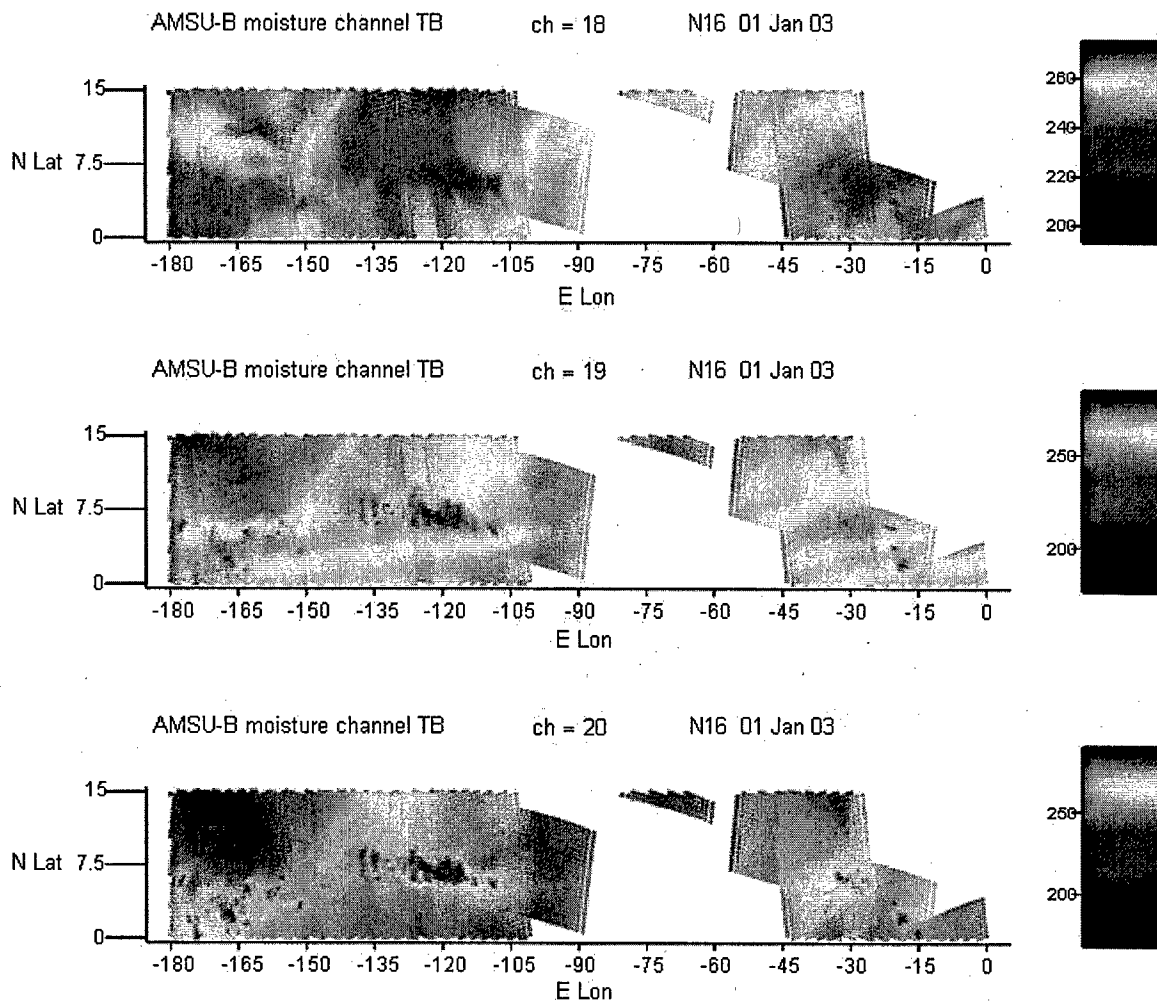


Figure 5.4: AMSU-B moisture sounding channels (*TB18* through *TB20* top to bottom) convolved to AMSU-A resolution. NOAA-16 on 01 Jan 03.

convolution, the coldest AMSU-B FOV's contribute strongly to cooling the full FOV. The *TB17* weighting function is above surface in humid tropical conditions, so the scene is a relatively uniform 280 K background with cooler *TB*'s in precipitation and strong *TB* reduction by the MCS, which actually consists of several diffuse cold spots in *TB17*, instead of single sharp maxima observed in other window and sounding *TB*'s.

AMSU-B moisture channels (*TB18* through *TB20*, 183.31 +/- 1, 3, and 7 GHz) are shown in Figure 5.4. The progressively lower weighting functions of *TB18*, *TB19*, and *TB20* are evident in the increasing background *TB*. As channels penetrate deeper, they experience greater scattering *TB* depression. *TB18* is reduced the least (but still a considerable amount) by the MCS, while *TB20* appears similar to *TB17*, a result of their very similar weighting functions in humid conditions. An important feature to note is the large-scale variation of 20-40 K *TB* in each channel, caused by large-scale variation in precipitable water across the ocean basins.

Figure 5.5 contains scatter plots of each high-frequency window or moisture channel vs. *TB2*. The *TB15* and *TB17* curves qualitatively match the simulation-predicted results (Figure 4.7). Each follows a well-defined logarithmic curve from  $(TB2, TB15) \approx (150 \text{ K}, 200 \text{ K})$  to  $(TB2, TB15) \approx (200 \text{ K}, 270 \text{ K})$  as relative humidity (or slant path) increases. *TB15* then decreases with increasing *TB2*. The simulation results showed that this is scattering-induced. Similarly, *TB17* undergoes sharp initial rise with *TB2* followed by quick drop as scattering rapidly becomes important. *TB18* through *TB20* are also qualitatively similar to the simulation results. Each channel begins with a high *TB* (low weighting function peak) at low *TB2*. *TB18* through *TB20* then decrease with increasing *TB2* due to the weighting function rising. The more sparsely populated triangular region of depressed *TB* for channels 18-20 appears to be a

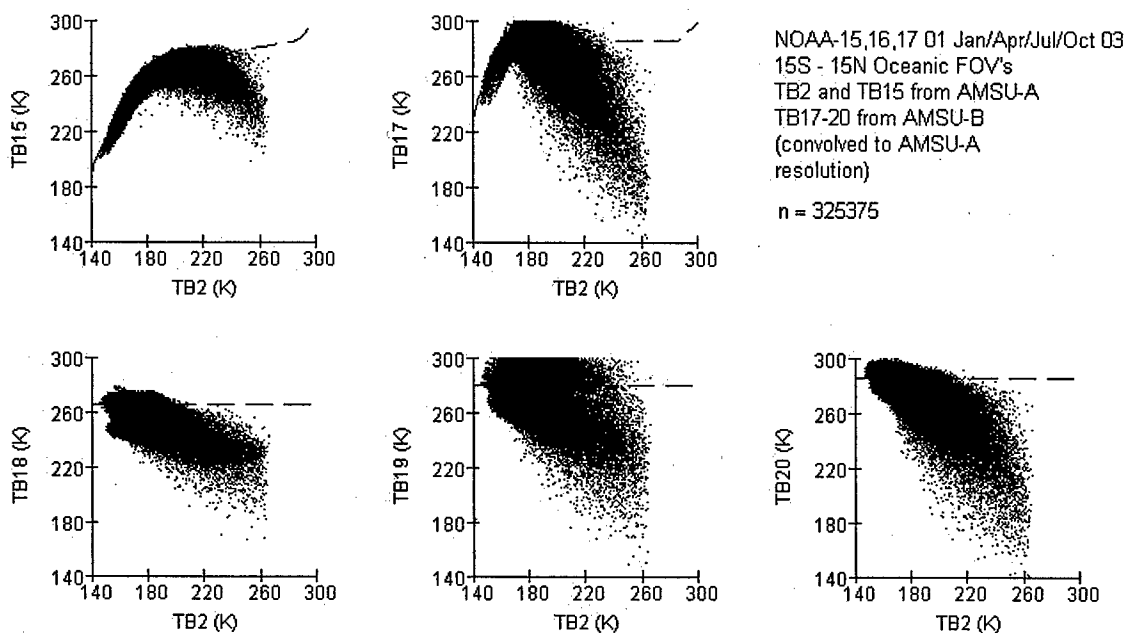


Figure 5.5: AMSU-A *TB15* and AMSU-B *TB17* through *TB20* (convolved to AMSU-A resolution) vs. AMSU-A *TB2* for all FOV's used in the tropical ocean scenes shown in Figures 5.1-5.4.

scattering effect. Note that, despite little scattering effect in the simulations, *TB18* does exhibit some depression.

Figure 5.6 depicts the same, except for 75,319 FOV's within 1000 km of a TC center. Land was not filtered out of these scenes. For land FOV's, the high surface emissivity makes all window *TB*'s large. Each plot has a cluster of clear land scenes in its upper right; this is most distinct in *TB15* and *TB17*. A dense line of points connects this land cluster to the opaque humid/cloudy atmosphere point ( $TB2, TB15 \approx (200 \text{ K}, 270 \text{ K})$ ). Similar dense lines of points (most visible in *TB15*, *TB17*, and *TB20*) connect the land cluster and the opaque humid/cloudy curve to a point near ( $TB2, TB15 \approx (260 \text{ K}, 200 \text{ K})$ ) or ( $TB2, TB17 \approx (260 \text{ K}, 140 \text{ K})$ ).

There are similar, but less distinct, land clusters in *TB18* through *TB20* (all of whose surface contributions are usually weak), along with triangular regions funneling points toward a

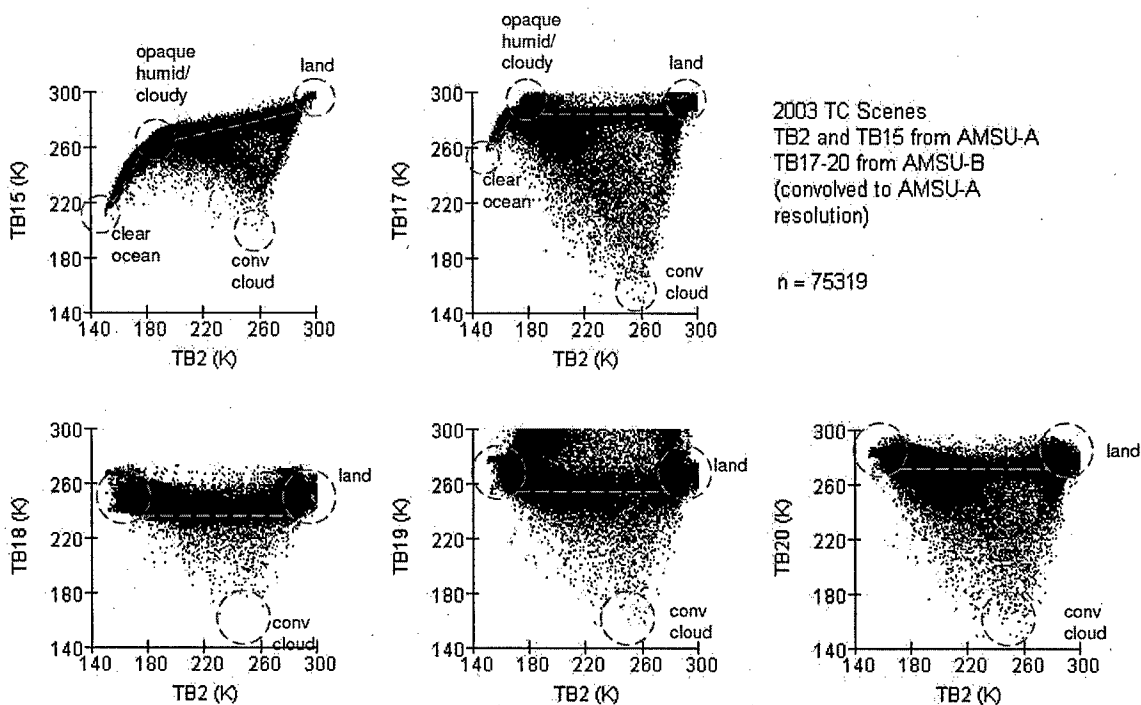


Figure 5.6: Same as Figure 5.5, but for 2003 Atlantic hurricane scenes (with land FOV's included). Dashed circles highlight multi-channel  $TB$ 's from clear ocean scenes, humid/cloudy scenes, clear land scenes, and FOV's filled with convective precipitation. Dashed line indicates approximate no-scattering  $TB$ 's.

limiting point near  $TB2 = 260$  K. The maximum depression occurring for each channel near  $TB2 = 260$  K is likely caused by FOV's completely filled with deep cumulus convection. Points along the denser lines are clear scenes over ocean or land with varying fractions of convection within the scene. Points within the triangle bounding the three limiting points each contain some mix of land, ocean, clouds, and convection.

Since the observed  $TB$  is a weighted average of the different constituent scenes within the FOV, the amount of convection filling a scene can be estimated by how far its point in  $TB2$ - $TBx$  space is pulled away from the non-scattering line and toward the limiting convective point. This is essentially what the  $\Delta TB$  from the simulations in Chapter 4 was measuring. By measuring

how far the high-freq window or moisture channel  $TB$  is depressed from the no-scatter line, we obtain a proxy for the fraction of the beam filled with scattering precipitation.

The data samples depicted in Figures 5.5 and 5.6 form the basis for the following empirical relations for the predicted high-frequency non-scattering  $TB$  as a function of  $TB2$ :

$$\begin{aligned}
 TB15_{pred} &= \left. \begin{cases} -529.9 + 7.8234 \times TB2 - 0.01909 \times TB2^2 & TB2 \leq 200K \\ 270 + \frac{15}{85}(TB2 - 200) & 200K < TB2 \leq 285K \\ TB2 & TB2 > 285K \end{cases} \right\} \\
 TB17_{pred} &= \left. \begin{cases} -1387.6 + 19.68 \times TB2 - 0.05794 \times TB2^2 & TB2 \leq 170K \\ 285 & 170K < TB2 \leq 285K \\ TB2 & TB2 > 285K \end{cases} \right\} \\
 TB18_{pred} &= 240K \\
 TB19_{pred} &= 260K \\
 TB20_{pred} &= 280K
 \end{aligned}$$

Sounding channel  $TB$  depression is caused by rain and ice that fills the beam both horizontally and vertically, since precipitation that doesn't reach the level of sensitivity of a channel's weighting function won't affect it significantly. So each channel will have a different slope relating its scattering  $\Delta TB$  to that of a high-frequency window or moisture channel. Figure 5.7 shows scatter plots of limb-corrected  $TB7$  and  $TB8$  vs.  $\Delta TB15$  and  $\Delta TB19$ . Dashed lines overlaid on the plots are least-squares best-fit lines for points with high-frequency depressions exceeding one standard deviation. As predicted by the simulation results,  $TB8$  has the weakest scattering reduction signature. The bimodal  $TB8$  distribution is caused by seasonal variation in tropopause height; the 01 Jan 03 and 01 Apr 03 average  $TB8$  is 215.5 K while the 01 Jun 03 and 01 Oct 03 average  $TB8$  is 216.5 K. Table 5.1 summarizes sounding channel vs. window/moisture channel depression correlations.

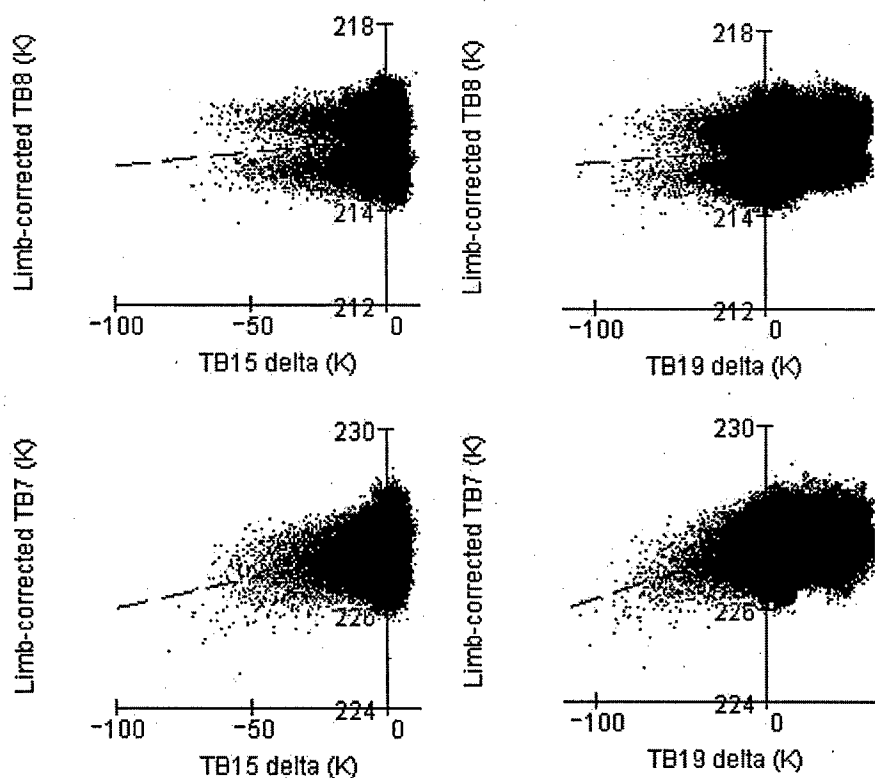


Figure 5.7: Limb-corrected TB8 (top row) and TB7 (bottom row) vs. TB15 scattering depression (left column) and TB19 scattering depression (right column). Dashed lines are least-squares best-fit to points with  $\Delta TB15$  or  $\Delta TB19 < -1\sigma$ .

Table 5.1: AMSU-A limb-corrected temperature sounding channel  $TB$  correlation with window/moisture channel  $\Delta TB$

	$\Delta TB15$	$\Delta TB17$	$\Delta TB18$	$\Delta TB19$	$\Delta TB20$
$\Delta TB8$	.079	.053	.044	.070	.031
$\Delta TB7$	.24	.24	.37	.39	.22
$\Delta TB6$	.37	.39	.47	.49	.40
$\Delta TB5$	.59	.59	.50	.56	.57
	n=37573	n=25711	n=2947	n=5506	n=55951

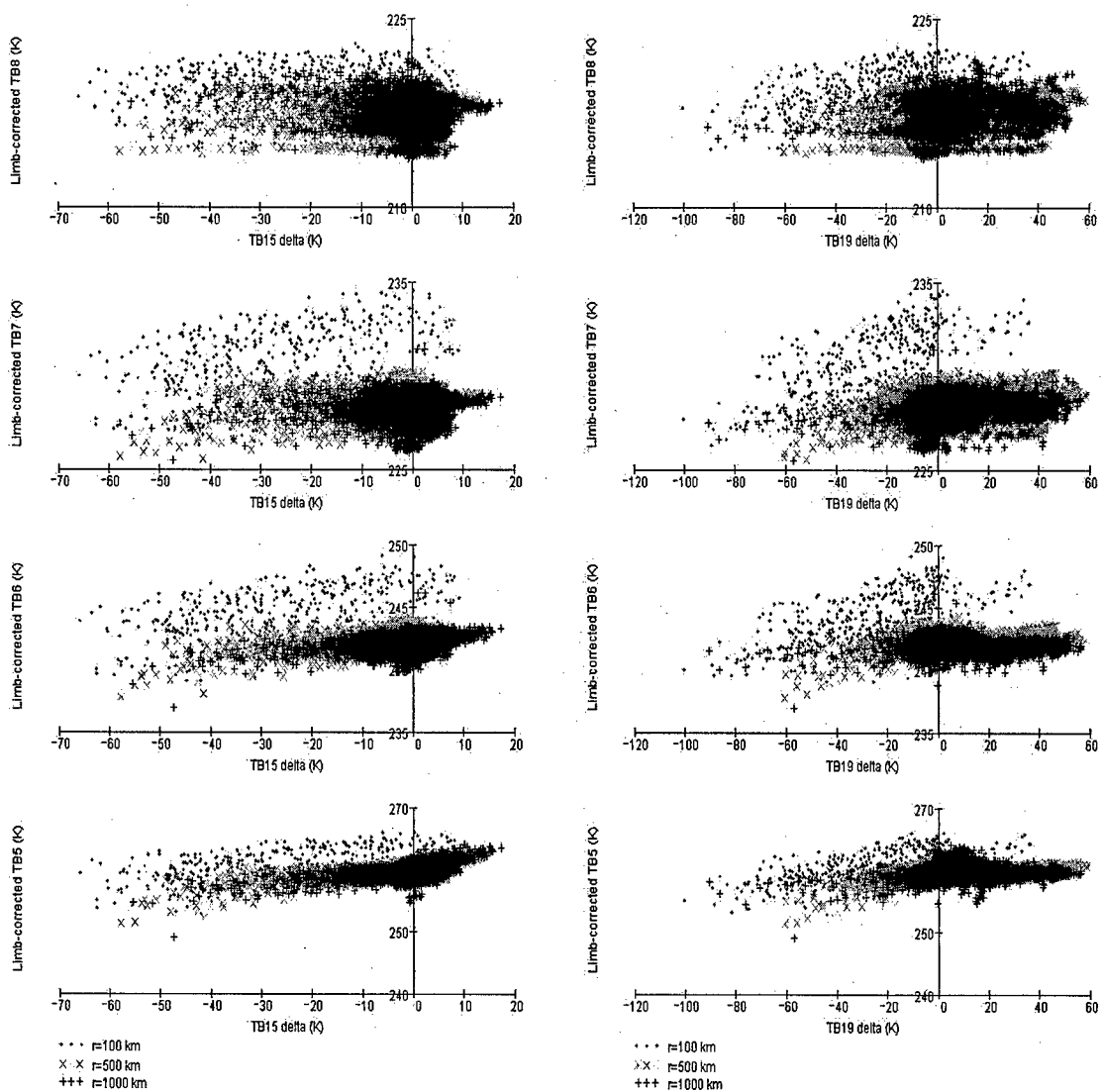


Figure 5.8: Sounding channel  $\Delta TB$  vs.  $\Delta TB15$  (left) and  $\Delta TB19$  (right) for 2003 Atlantic TC scenes. Dots denote points within 100 km of TC center; x's, points at 500 km from TC center; and +'s 1000 km.

The nearly linear relationships evident among limb-corrected sounding *TB* and window/moisture *TB* depressions should make it straightforward to correct for scattering by simply adding the product of the slope and the window/moisture channel depression. There is a complication, however. Figure 5.8 depicts limb-corrected sounding channel depression vs. *TB15* and *TB19* depression at three different radii from storm center in the 2003 Atlantic TC scene data. Points at 500 km and 1000 km from storm center have nearly identical slopes as obtained from the tropical ocean scenes. But points within 100 km of storm center appear to have significantly larger slopes, especially for *TB7* and *TB8*. For all radii, there is a large cluster of points with small window/moisture depression. But at small radii, the TC warm anomaly is reflected in the much greater spread in sounding channel *TB*. It is this population which appears to have the greater slope.

There are at least two possible explanations for this discrepancy. The first is simply that, while all tropical convection is weak by mid-latitude standards, it is slightly stronger in TC eyewalls and spiral bands than it is in the tropical oceans in general. Cecil (2002) used the Tropical Rainfall Measuring Mission Microwave Imager and Precipitation Radar to show that TC eyewall convection tends to have higher radar reflectivity at higher altitudes than general oceanic convection, as well as colder 85 and 37 GHz polarization-corrected temperature (PCT; i.e. greater ice scattering). Figure 5.9 from Cecil (2002) compares the radar reflectivity profiles in different tropical convective settings. Saturated parcels start their ascent in either the TC eyewall or a tropical cumulonimbus cloud with approximately the same moisture content--that of a saturated parcel at a sea surface temperature near 300 K. High-frequency window channels are primarily sensitive to the vertically integrated water and ice content--which should be

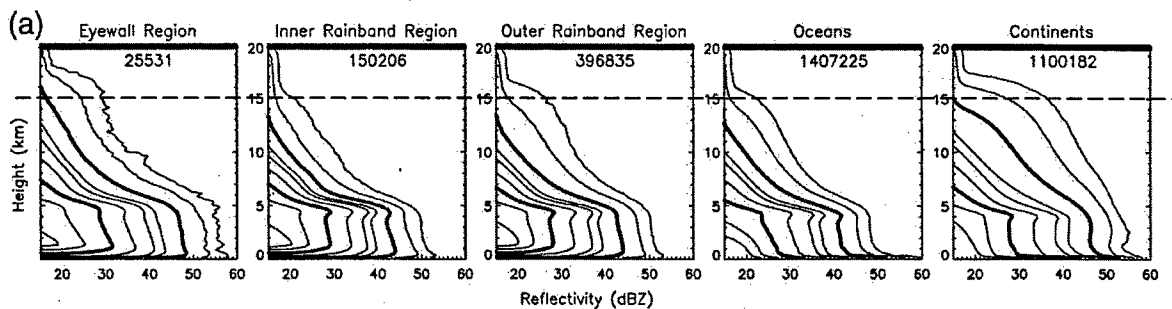


Figure 5.9: Tropical Rainfall Measuring Mission (TRMM) Precipitation Radar (PR) cumulative reflectivity profiles for (left to right) TC eyewalls, TC inner rainbands, TC outer rainbands, tropical oceanic convection, and tropical continental convection. Bold contours are 50th and 99th percentile of the cumulative distribution. Dashed line is overlaid at 15 km altitude (approximately the level of AMSU-A *TB8* weighting function peak). From Cecil (2002).

approximately the same in either eyewall or general tropical conditions--while a sounding channel is sensitive only to the scatterers that reach the level to which its weighting function is sensitive. Said differently, the mechanically-driven ascent in the TC eyewall may be able to loft the same liquid and ice content to a higher altitude than the weakly buoyant moist ascent in a convective hot tower in the inter-tropical convergence zone (ITCZ), thus affecting upper-level sounding channels more for the same window channel depression.

A second, related, explanation is based on the difference in the ambient environment surrounding the convective updrafts. By the time a TC forms, the radially confined heat released by the organizing convection has created a nearly moist lapse rate through the troposphere, so convective updrafts in the eyewall and inner spiral bands are nearly isothermal with the surrounding environment aloft. Away from a TC, convective updrafts occur in an unsaturated environment where parcels are radiating to space and sinking subsiding everywhere outside the convective updraft (thus the requirement for hot towers as articulated by Simpson et al. 1998). So the mid and upper levels in the tropics can be considerably cooler and drier than the warm,

saturated environment in the immediate vicinity of a TC center. The convective cell affecting a sounding channel is averaged with the *TB* contribution from the rest of the 3-D volume of the FOV. In the isolated tropical convective cell, the updraft core may be substantially warmer than the surrounding environment, so the *TB* depression caused by scattering competes with warming contributed by the updraft itself. For convection in and near the TC eyewall, though, the updraft's temperature is nearly equal to its surroundings, so scattering can depress the sounding channel *TB* without competition from the sensible heat added by an isolated hot tower's core. Figure 5.10 illustrates conceptually the disparate effects of scattering precipitation on AMSU high-frequency window and temperature sounding channels.

Whatever the physical mechanism, it appears necessary to apply a larger sounding vs. window/moisture *TB* depression slope to correct for scattering in proximity to a TC center.

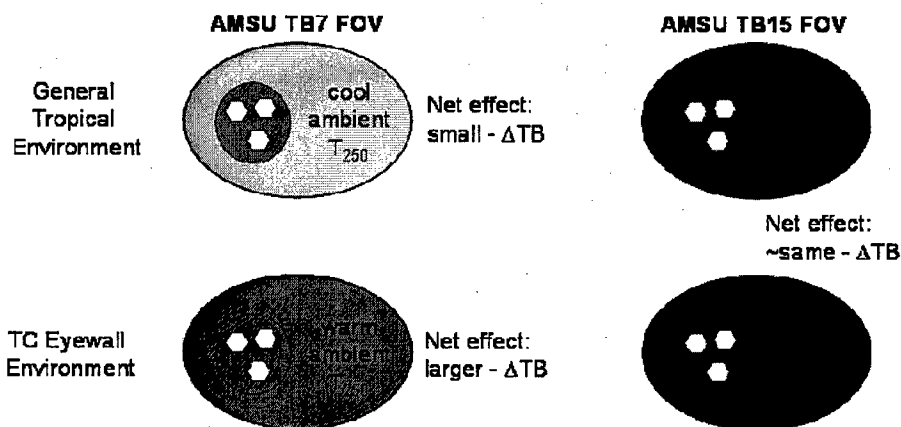


Figure 5.10: Conceptual diagram of ambient environment modulation of sounding channel scattering *TB* depression. AMSU-A sounding channel (e.g. TB7) FOV (left column) and high-frequency window channel (e.g. TB15) FOV (right column) for isolated tropical convective cells in the ambient tropical environment (top row) and eyewall convection (bottom row). Window channel ambient environment (the opaque humid lower troposphere) and scattering by hydrometeors are the same in both cases. Sounding channel ambient environment is cooler for isolated tropical convection so warm convective core counters some of the hydrometeor scattering effect. Sounding channel ambient environment and convective core temperatures are approximately equal, so scattering acts unopposed. Net effect is larger sounding channel  $\Delta TB$  for the same window channel  $\Delta TB$  in TC eyewall convection.

Table 5.2 summarizes the slopes for the general tropical convection case (weaker slopes) and the

Table 5.2: Sounding  $\Delta TB$  vs. window/moisture maximum  $\Delta TB$  slope for near-TC cases and general tropical cases

	$\Delta TB15$		$\Delta TB17$		$\Delta TB18$		$\Delta TB19$		$\Delta TB20$	
	max	general								
$\Delta TB8$	.028	.0060	.020	.0015	.093	.0029	.030	.0030	.032	.0012
$\Delta TB7$	.058	.013	.029	.0045	.11	.019	.055	.012	.031	.0058
$\Delta TB6$	.070	.032	.072	.012	.13	.038	.078	.026	.042	.017
$\Delta TB5$	.086	.067	.043	.025	.14	.069	.065	.048	.052	.031

maximum slope observed within 100 km of the 2003 TC centers.

The correlation coefficients in Table 5.1 indicate that  $\Delta TB18$ ,  $\Delta TB19$ , and  $\Delta TB15$  are best correlated with sounding channel depression. These three predictor channels are each tested for their ability to improve the correlation between  $TB7$  and  $TB8$  warm anomaly and TC  $MSLP$ . For each of the three candidate predictor channels, three correction methods are tested. The first correction method used only the sounding  $\Delta TB$  vs. high-frequency  $\Delta TB$  slope derived from the non-TC tropical data set. The second method used the maximum slopes from Table 5.2 for FOV's within a 3 x 3 box centered on a TC's estimated location and the weak non-TC slopes elsewhere. The third method used the average of the weak and strong slopes for the 3 x 3 storm-centered box and weak slopes elsewhere.

Testing data for this chapter and Chapter 6 was a set of 497 AMSU observations of Atlantic basin TC's from 1998 to 2004. Each AMSU overflight was coincident (within +/- 3 hours) with an aircraft reconnaissance  $MSLP$  observation, which serves as ground truth. For each AMSU overflight, a 30 FOV x 30 FOV box is centered on the storm's position, which was interpolated from post-analyzed best-track data. AMSU-B  $TB$ 's were convolved, as described in Section 5.1, and stored along with the AMSU-A  $TB$ 's for the 30 x 30 FOV array.

The desired scattering correction is applied (Figure 5.11 is an example of the *TB15*-based scattering correction applied to limb-corrected *TB7* and *TB8*) and the *TB7* and *TB8* warm anomalies are computed as follows:

1. Limb-correct the raw sounding channel *TB*'s
2. Compute the predicted no-scatter *TB15* (or *TB18* or *TB19*) using *TB2*
3. Compute  $\Delta TB15$  (or  $\Delta TB18$  or  $\Delta TB19$ )
4. If  $\Delta TB15$  (or  $\Delta TB18$  or  $\Delta TB19$ ) is less than zero, multiply it by the appropriate sounding channel slope and add the absolute value of the result to the limb-corrected sounding channel *TB*
5. For each FOV adjacent to the interpolated storm position:
  - a. Compute the environmental brightness temperature,  $TB_{env}$ , using up to 4 FOV's spaced +/- 8 FOV's in the along- and cross-track directions from the FOV being considered
  - b.  $\Delta TB7$  or  $\Delta TB8$  is the difference between the selected FOV's *TB* and  $TB_{env}$ .
6. Pick the largest  $\Delta TB7$  or  $\Delta TB8$  from the array of FOV's surrounding the center.

The full dataset is divided into a 249-sample test set, used to develop regression coefficients, and a 248-sample validation set. Table 5.3 summarizes correlations between  $\Delta TB7$  or  $\Delta TB8$  and TC *MSLP* for non-corrected *TB*'s and each of the nine scattering correction methods tested.

Table 5.3: Comparison of *TB7* and *TB8* Anomaly Correlation with TC *MSLP*, n=248

Scattering correction method	None	TB15			TB18			TB19		
		general	max	average	general	max	average	general	max	average
TB7 warm anomaly correlation	.803	.856	.886	.899	.830	.647	.797	.753	.340	.528
TB8 warm anomaly correlation	.872	.889	.899	.903	.875	.646	.810	.865	.569	.720

Surprisingly, *TB18*- and *TB19*-based scattering corrections reduced the correlations, dramatically in some cases. Variation in humidity causes considerable variability in the height at

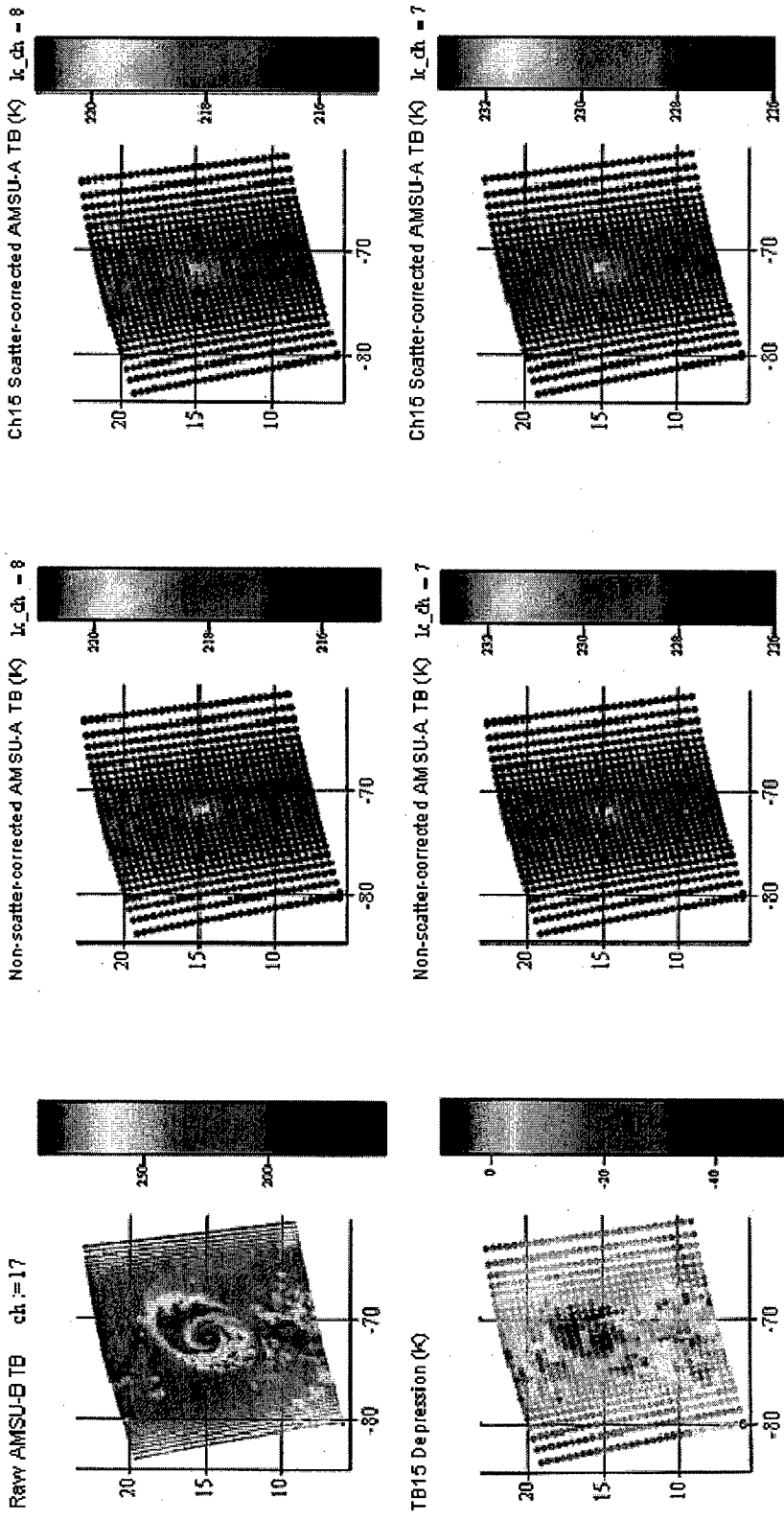


Figure 5.11: Hurricane Ivan 1904 UTC 19 Sep 04. AMSU-B TB17 (upper left) clearly shows eyewall and spiral band convection (cold TB's). AMSU-B TB15 (lower left). AMSU-A limb-corrected TB7 (top-middle) and TB8 (bottom-middle) prior to scattering correction. Depression within the TC warm anomaly is not evident, as the warm anomaly is several K, while scattering effects on TB7 and TB8 are on the order of 1 K. Scattering-corrected TB7 (top right) and TB8 (bottom right). TB7 warm anomaly has increased by approximately 0.5 K. Scattering effects on TB8 are far less noticeable. Note also that the cool surrounding TB's (especially in the northeast spiral band) have increased, yielding a smoother environmental TB field.

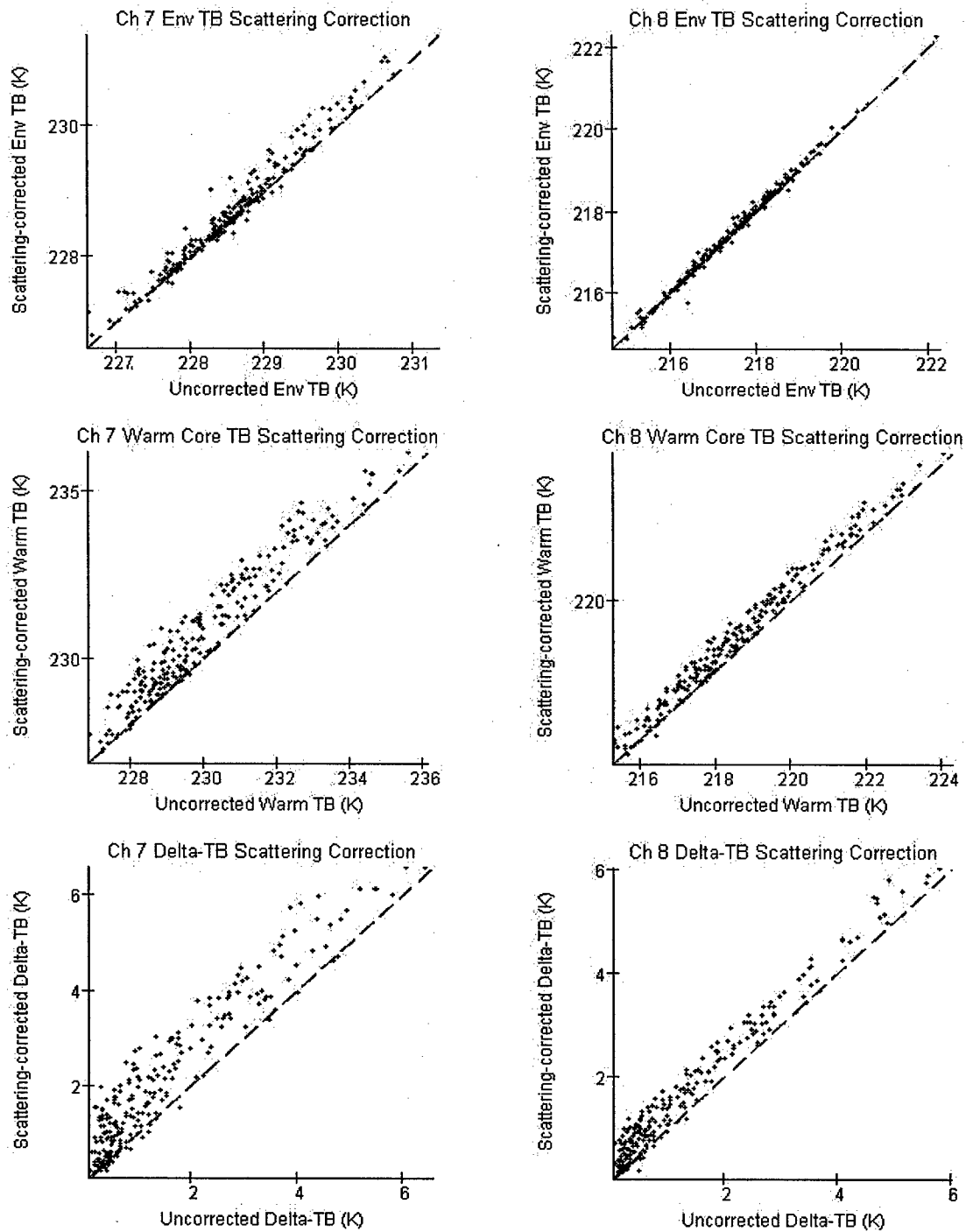


Figure 5.12: Channel 7 (left column) and 8 (right column) scattering correction effect on environmental *TB* (top row), warm *TB* (middle row), and  $\Delta TB$  (bottom row) for 248 Atlantic TC cases from 1998-2004.

which the  $TB_{18}$  and  $TB_{19}$  weighting functions peak, causing a wide range of  $TB$  variability (20 - 30 K) not attributable to scattering. In proximity to a TC center, where there may be a considerable area of near saturation, these channels' weighting functions would rise and reduce  $TB_{18}$  and  $TB_{19}$ , independent of any scattering effects. This may be causing them to over-correct the sounding channel  $TB$ 's.

$TB_{15}$ -based scattering corrections, however, improved correlations for both  $\Delta TB_7$  and  $\Delta TB_8$ . The best performance is obtained using the averaged weak and strong slope near storm center and the weak correction at large radii. Since the scattering correction is applied to all FOV's in the 30 x 30 array, it has potential to affect both  $TB_{env}$  and the warm pixel  $TB$ . Figure 5.12 depicts pre- and post-correction  $TB_{env}$ , warm  $TB$ , and  $\Delta TB$  for channels 7 and 8. Figure 5.13

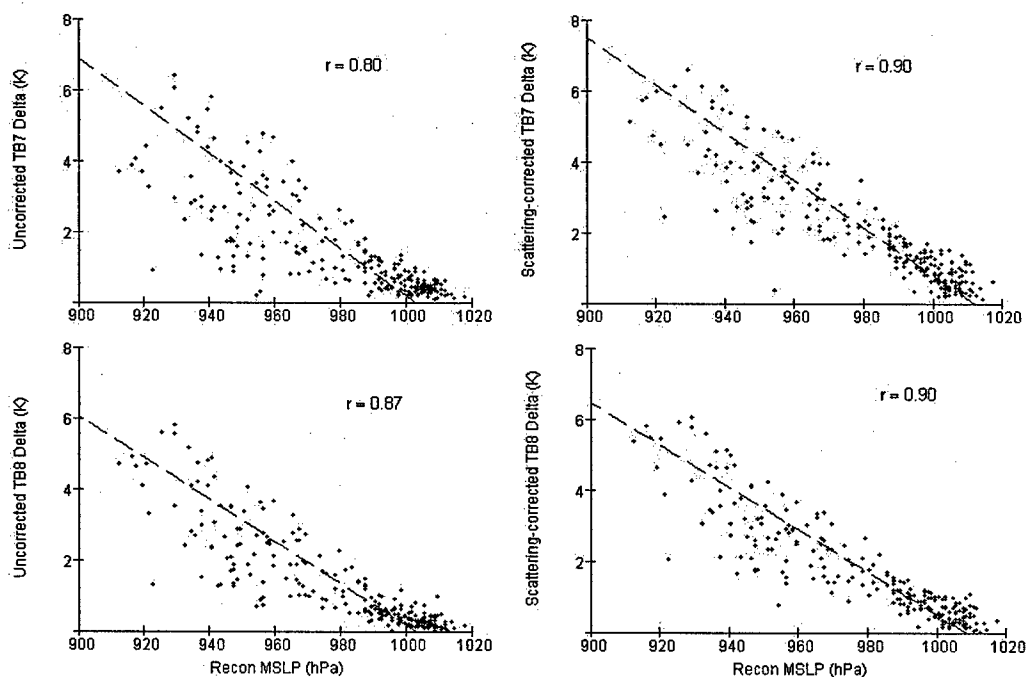


Figure 5.13: Non-corrected (left column) vs. scattering-corrected (right column)  $\Delta TB_7$  (top row) and  $\Delta TB_8$  (bottom row) correlation with TC MSLP for 248 Atlantic TC cases from 1998-2004.

includes four scatter plots of uncorrected and corrected  $\Delta TB7$  and  $\Delta TB8$  vs.  $MSLP$ . The reduction in scatter is especially dramatic for  $\Delta TB7$ .

### 5.3. Discussion

The results presented in this chapter explain the physical mechanism underlying variability in  $TB2$  and high-frequency window/moisture channel space. They demonstrate that  $TB2$  can be used effectively to estimate  $TB15$  or  $TB17$  in the absence of precipitation effects (due to the  $TB18$  through  $TB20$  variability caused by humidity,  $TB1$  is less effective at pinning down what those  $TB$ 's should be in the absence of scattering).  $\Delta TB15$ ,  $\Delta TB18$ , and  $\Delta TB19$  have the most robust relationship with limb-corrected sounding channel  $\Delta TB$ , and of those three channels,  $TB15$  is the only one that improves the correlation between upper tropospheric warm  $TB$  anomaly and TC  $MSLP$ . In Chapter 6, the  $TB15$  scattering correction method will be applied to CIMSS' AMSU-based TC intensity estimation algorithm.

## 6. A Precipitation Correction for the CIMSS AMSU-based TC Intensity

### Estimation Algorithm

Chapter 5 built on the theoretical basis from Chapter 3 and the simulation study results from Chapter 4 to develop an empirical sounding channel precipitation correction. In Section 5.3, it was shown that the correction substantially improved  $\Delta TB7$  and slightly improved  $\Delta TB8$  correlations with TC *MSLP*. This chapter will apply the same precipitation correction method to the current CIMSS AMSU-based TC intensity algorithm and study its impact.

### 6.1. The Current CIMSS Operational TC Intensity Algorithm

The CIMSS algorithm is one of two AMSU-based techniques currently providing near real-time intensity estimates to TC warning centers. The other is the CIRA technique described in Section 2.3, which uses gridded AMSU retrieved temperature fields.

The current algorithm builds on the previous work of Kidder et al. (1978) and Velden and Smith (1983), and has undergone several evolutionary changes since its inception. In its original form, the algorithm corrected for sub-sampling using Merrill's (1995) warm anomaly structure retrieval initialized with a storm size estimate derived from the Laplacian of AMSU-B 89 GHz *TB*'s (Brueske 2001; Brueske and Velden 2003). Kabat (2002) introduced a  $\Delta TB8$  regression relation, in addition to the existing  $\Delta TB7$  relation, along with logic governing when to choose a *TB8 MSLP* estimate over a *TB7* estimate. Herndon et al. (2004) replaced the warm anomaly retrieval and *TB16* size estimate by using an external TC radius of maximum wind (RMW) estimate from a TC warning center as a proxy for the horizontal extent of the warm anomaly. Using the RMW compared to the known FOV size, Herndon et al. developed an *MSLP* size bias

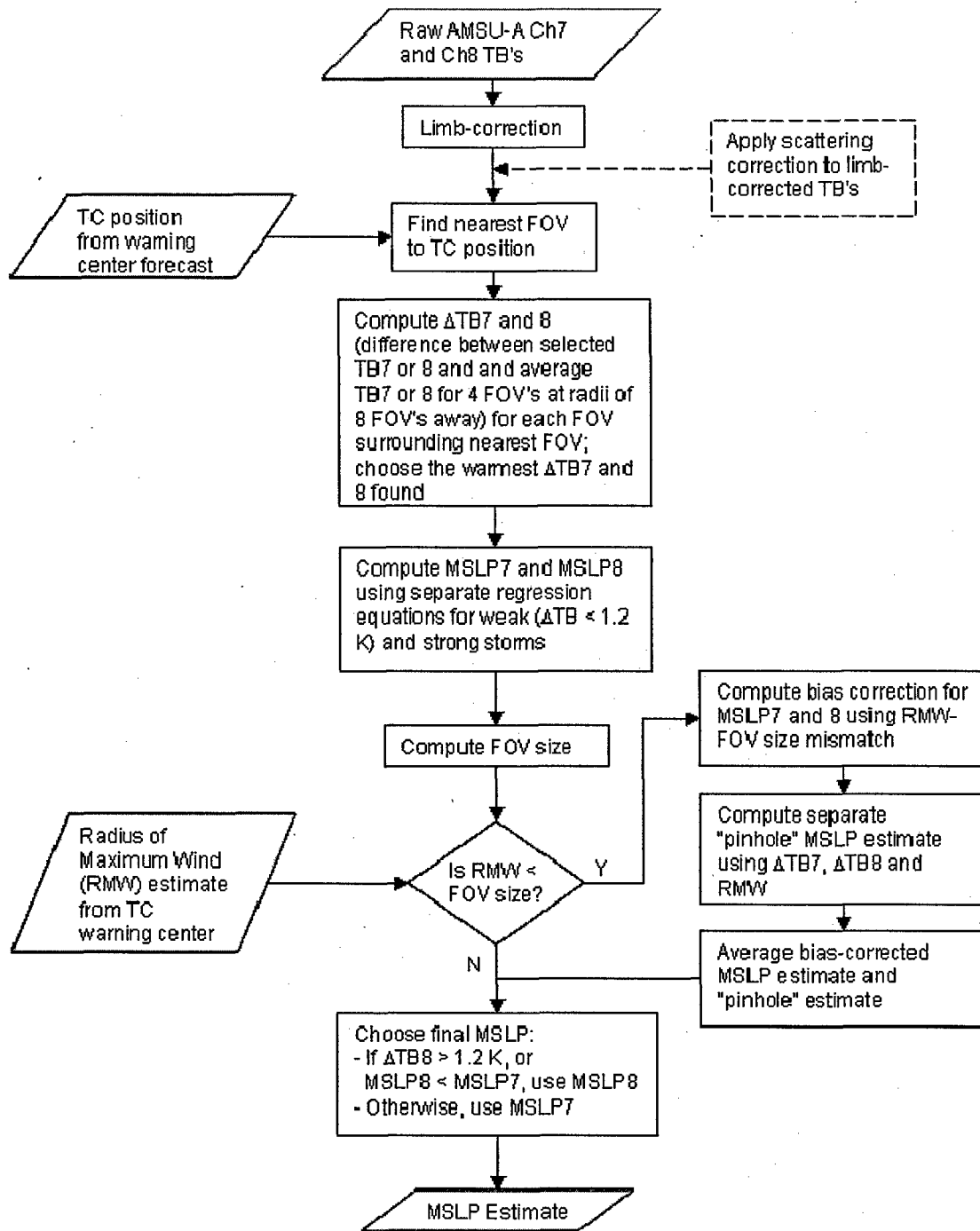


Figure 6.1: CIMSS AMSU-based TC intensity estimation algorithm flowchart. The dashed box at upper right indicates the point at which precipitation correction would take place.

correction, and noting that the warm anomaly vs. *MSLP* relationship was slightly non-linear, introduced two regression slopes for each channel, to be used according to the strength of the warm anomaly. Figure 1 is a flowchart outlining the current algorithm.

The two most significant recent changes with respect to precipitation effects were the inclusion of  $\Delta TB8$  by Kabat (2002) and the growth of its influence on the final *MSLP* estimate with changes implemented by Herndon et al. (2004). Currently a channel 7-based *MSLP* estimate is only chosen in weak cases ( $\Delta TB8 < 1.2$  K) where channel 7 yields a lower *MSLP* estimate than *TB8*. As noted in Chapters 4 and 5, channel 8's weighting function peaks high enough in the troposphere as to make it only weakly susceptible to precipitation effects, and to make correction problematic.

Sources of error in the current algorithm include: instrument noise (tenths of a K), bracketing of the warm core between adjacent fields of view (could introduce errors comparable to the warm anomaly magnitude itself); sub-sampling of the warm core by the large instrument FOV, especially at large scan angles (again, could introduce error comparable to warm anomaly magnitude), and precipitation effects, which for *TB7* and *TB8* are on the order of 2 K and tenths of a K, respectively. The presence of the other sources of error imposes a limit on how well the algorithm can perform, even with a perfect scattering correction. CIRA's algorithm, the  $V_{max}$  technique described in Spencer and Braswell (2001), and the CIMSS algorithm have all converged to very nearly the same accuracy figure, suggesting that each technique may be squeezing as much accuracy out of the current instrument as possible.

## 6.2. Precipitation Correction Methodology

The details of the precipitation method were discussed in Chapter 5, but are outlined again here:

1.  $TB2$  is used to predict  $TB15$  in the absence of scattering

$$TB15_{pred} = \left\{ \begin{array}{l} -529.9 + 7.8234 TB2 - 0.019093 TB2^2 \quad \text{if } (TB2 < 200; \text{humid scenes}) \\ 270 + \frac{15}{85}(TB2 - 200) \quad \text{if } (200 < TB2 < 285; \text{cloudy land scenes}) \\ TB2 \quad \text{if } (TB2 > 285; \text{clear land scenes}) \end{array} \right\}$$

2. If  $TB15$  is depressed below this predicted value, the difference is multiplied by the empirical sounding  $\Delta TB$  vs.  $\Delta TB15$  slope found in Chapter 5 to obtain the sounding channel  $TB$  correction.
3. For AMSU  $TB$ 's within 2 FOV's of the TC center, a stronger  $TB$  correction slope is used, which averages the slope found Chapter 5 for the general tropical convection cases with the slope observed in TC cases. Table 6.1 summarizes these sounding  $TB$  correction slopes for use with  $\Delta TB15$ .

Table 6.1: Sounding channel  $TB$  vs.  $\Delta TB15$   
precipitation correction slopes

Channel	General slope	TC core slope
8	.006	.017
7	.013	.036
6	.032	.051
5	.067	.075

## 6.3. Validation data set

The data set used for this validation effort consists of 497 AMSU observations of TC's. Historical storm positions, intensities, and RMW at six-hour intervals were obtained from the

National Hurricane Center's TC Best Track dataset. Using archived orbital elements for the NOAA satellites and the best-track storm positions, each AMSU overflight of a known TC since June 1998 (when the first AMSU instrument flew on NOAA-15) was determined. From that large listing of overflights, times within 3 hours of a WP-3D or WC-130 aircraft reconnaissance observation of the storm were selected. AMSU data for the selected overflights were obtained from the AMSU archive at CIMSS, supplemented by data obtained from NOAA's Comprehensive Large-Array Stewardship System.

Aircraft reconnaissance *MSLP* is taken to be ground truth for this study, but it has several sources of error. First, the *MSLP* is determined either from a dropsonde, which has accuracy of 1 hPa (Hock and Franklin 1999), or by extrapolating *MSLP* from the temperature and pressure aloft, which can have substantially larger error. Second, the sonde is dropped as nearly as possible to where the crew believes the storm center to be, but this position may be in error, causing the true minimum in sea-level pressure to be missed. Third, since the AMSU overflight and reconnaissance observation are not exactly coincident, storm intensity change during the interim may also add error on the order of a few hPa.

The precipitation-corrected *TB7* and *TB8* anomalies will have a different *MSLP* relationship than their uncorrected counterparts, so the *MSLP* regression coefficients and size bias correction coefficients are re-derived after scattering correction. To avoid over-fitting, the data set is divided in half, with the 249 odd-numbered observations used to obtain the regression coefficients and the 248 even-numbered observations used for validation.

#### 6.4. Cleaner TB7 or TB8 vs. MSLP Relationship from Scattering Correction

As noted in Chapter 5, scattering correction improves the correlation between *TB7* or *TB8* anomaly and *MSLP*, so before studying performance of the current CIMSS algorithm, we note that a simple linear regression of *TB7* anomaly achieves 12.4 hPa RMSE (a 3.6 hPa improvement) and *TB8* anomaly achieves 12.2 RMSE (a 1.2 hPa improvement). As Herndon et al. (2004) noted, AMSU will sub-sample the warm anomaly in cases where the RMW is small and the instrument FOV is large; this becomes a significant error source for estimates at large

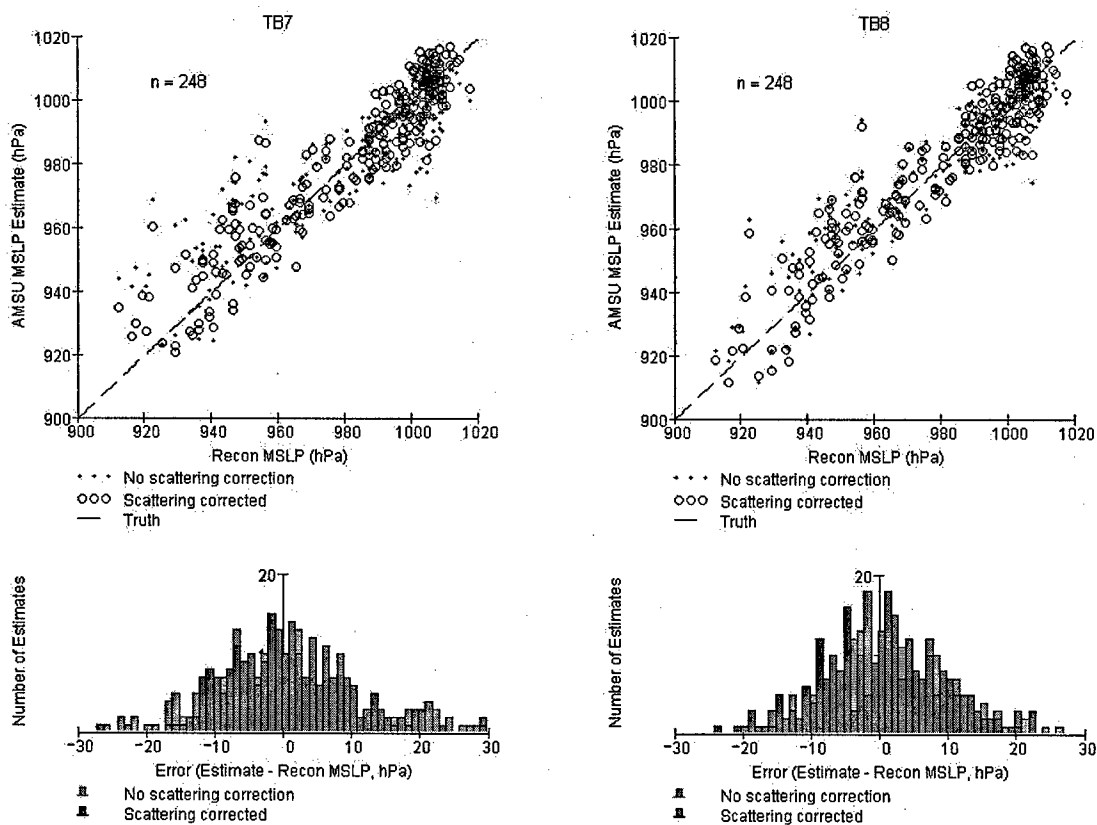


Figure 6.2: Improvement in single-channel size-bias corrected *MSLP* estimates after precipitation correction is applied to AMSU *TB7* and *TB8*. RMSE for channel 7 estimates after correction is 9.3 hPa; for channel 8 it is 9.0 hPa.

scan angles. If a multiple regression bias correction, using RMW and FOV is applied to the single-channel estimates, RMSE improves to 9.3 hPa (for channel 7) and 9.0 hPa (for channel 8). These RMSE values are comparable to non-scattering corrected RMS errors for the CIMSS algorithm. Figure 6.2 includes scatter plots of AMSU channels 7 and 8 *MSLP* estimates vs. aircraft-measured *MSLP* with and without scattering correction.

### 6.5. CIMSS Algorithm Performance Improvement

Figure 6.3 is the same as Figure 6.2, but for the CIMSS two-channel algorithm. RMSE and average mean error improvement (summarized in Table 6.2) are more modest. Two reasons explain why: First, as noted above, as the algorithm has evolved, it has become very *TB8* centric. *TB7* estimates only come into play for weak TC's, and even then, only when channel 7 estimates a lower *MSLP* than channel 8 (which sometimes occurs when the nascent warm anomaly is confined to around 250 hPa and hasn't yet grown upward to 150 hPa). As the results in Chapter 4 and 5 indicate, AMSU channel 8 is largely immune to scattering by tropical convection, which rarely reaches the 15 km height where the limb-corrected channel 8 weighting function peaks.

The second reason for the modest CIMSS algorithm performance improvement is that the current size bias correction is already indirectly correcting for some scattering effects. Herndon et al. (2004) found a weak bias for small storms and large scan angles (where the AMSU FOV is largest) caused by sub-sampling. So when the algorithm determines that the warm anomaly size (as represented by RMW) is smaller than the instrument FOV size, it decreases the *MSLP* estimate to correct the weak bias caused by the sub-sampled warm anomaly.

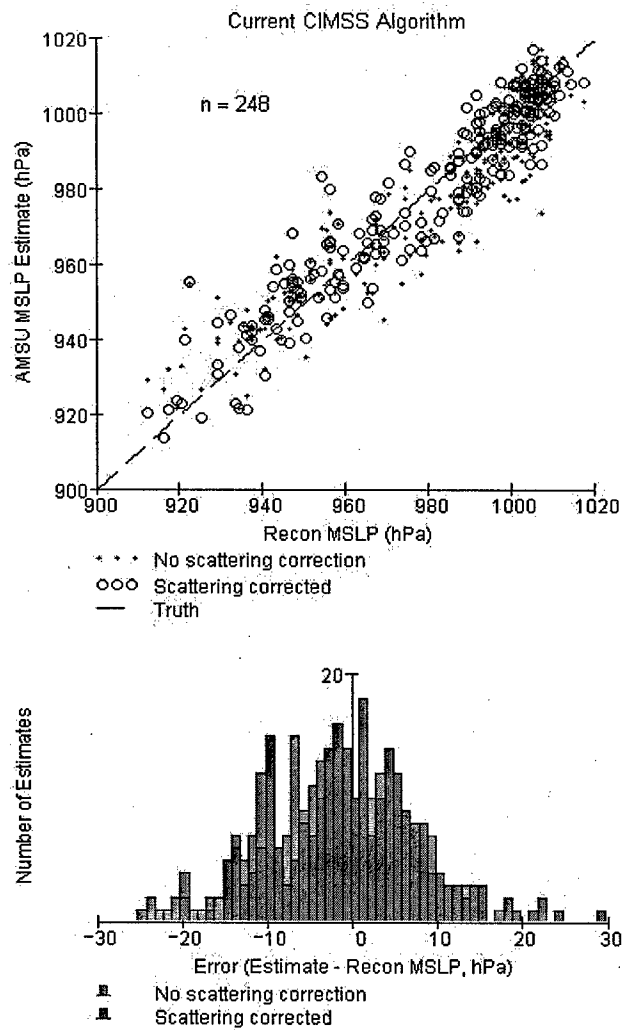


Figure 6.3: Comparison of CIMSS TC intensity algorithm performance before and after precipitation correction. The histogram at bottom compares errors without (background) and with (foreground) scattering correction.

Table 6.2: Comparison of RMSE, Average Mean Error (AME), and bias of CIMSS TC intensity estimates with and without precipitation correction

Method	RMSE (hPa)	AME (hPa)	bias (hPa)
Non-corrected	8.8	6.8	-0.01
Precipitation corrected	8.0	6.1	1.1
n = 248			

Figure 6.4 is a scatter plot of RMW vs. *MSLP* for the TC's in the  $n = 248$  validation dataset tested here, and it shows the strong relationship between increasing TC intensity and decreasing storm radius. But as storm intensity increases (and intense convection is localized in the relatively small eyewall), precipitation scattering is more likely to significantly weaken sounding channel *TB*'s near storm center. So sub-sampling and precipitation scattering complement each other and both conspire to weaken the warm anomaly measured by the instrument, weakening the AMSU intensity estimate. Thus, an empirical bias correction that corrects for weak estimates when RMW is small will also remove some of the error caused by

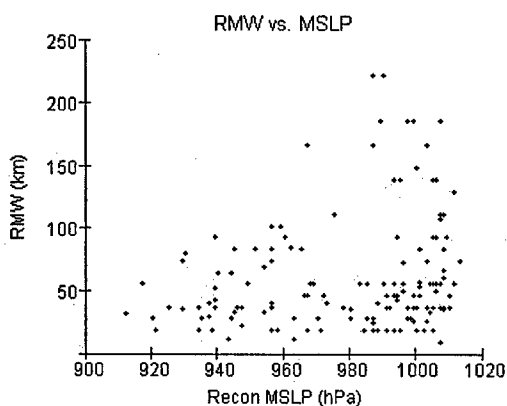


Figure 6.4: TC radius of maximum wind vs. *MSLP* for  $n = 248$  validation sample.

precipitation scattering. As evidence that this is in fact occurring, Table 6.3 compares the RMSE improvement of the size bias correction for non-precipitation corrected vs. precipitation corrected *TB7* and *TB8* *MSLP* estimates. The size bias contribution is reduced by about 1/3 (for channel 8) and about 1/2 (for channel 7). This is significant because the RMW value is

Table 6.3: Comparison of size-bias RMSE improvement on non-corrected and precipitation-corrected AMSU TC intensity estimates

Method	Pre size bias correction RMSE (hPa)	Post size bias correction RMSE (hPa)	Size bias RMSE improvement (hPa)
Non-corrected	9.9	8.8	1.1
Precipitation corrected	8.8	8.0	0.8
n=248			

obtained from the TC warning centers, where it is estimated by satellite analysts, and is therefore subject to significant inaccuracy, and often is missing due to high analyst workload or neglect.

Table 6.4 compares RMSE, AME, and bias changes vs. TC intensity before and after precipitation correction. Performance for 950-975 hPa storms actually deteriorated slightly due to creation of some outliers. The regression fit for weak storms and very strong storms, however was improved.

Table 6.4: CIMSS Algorithm RMSE, AME, and bias by TC intensity

		RMSE	AME	bias
No precipitation correction	>1000 hPa	7.6	5.9	-1.3
	975-1000 hPa	8.2	6.3	-2.5
	950-975 hPa	9.5	7.5	0.1
	<950 hPa	10.5	8.3	5.7
Precipitation corrected	>1000 hPa	5.7	4.3	-0.9
	975-1000 hPa	7.2	5.9	0.0
	950-975 hPa	10.0	7.5	2.9
	<950 hPa	9.9	7.8	4.2
n=248				

### 6.5. Another Approach Enabled by Scattering Correction

In Section 2.1, the expression relating *MSLP* to temperature anomaly requires the assumption that the *TB7* or *TB8* anomaly represents the mean temperature anomaly through the full depth of the troposphere. This assumption was necessary because of precipitation effects on the low- and mid-tropospheric sounding channels (*TB5* and *TB6*). Surface emissivity also affects the lowest channel, *TB4*. This precipitation correction does not correct *TB5* or *TB6* enough to add additional information beyond what the precipitation corrected *TB7* or *TB8* currently contains, but the corrected *TB*'s are usable for producing a vertically-averaged *TB* anomaly,

which has comparable RMSE and AME (9.4 hPa and 7.1 hPa) to single-channel estimates. An area for future work is to refine this vertically-integrated technique and explore whether it has skill in situations where single-channel estimates are prone to error.

## 6.6. Discussion

### Correcting for precipitation

substantially improves the *TB* anomaly vs. *MSLP* relationship for channels 5 through 7 while slightly improving channel 8. The current CIMSS algorithm, by evolving to become more reliant on the *TB8* anomaly and employing a size bias correction that indirectly corrects for scattering-induced weak intensity estimates, had already reduced the

impact of precipitation on intensity estimates. Essentially all of the gross outliers in the data set tested resulted from small storm size and/or scan geometry effects (sub-sampling and bracketing). The primary benefit of the scattering correction is to reduce some of the spread across the spectrum of intensity, rather than correcting individual gross outliers. A secondary benefit is the reduction of dependence on the external RMW estimates.

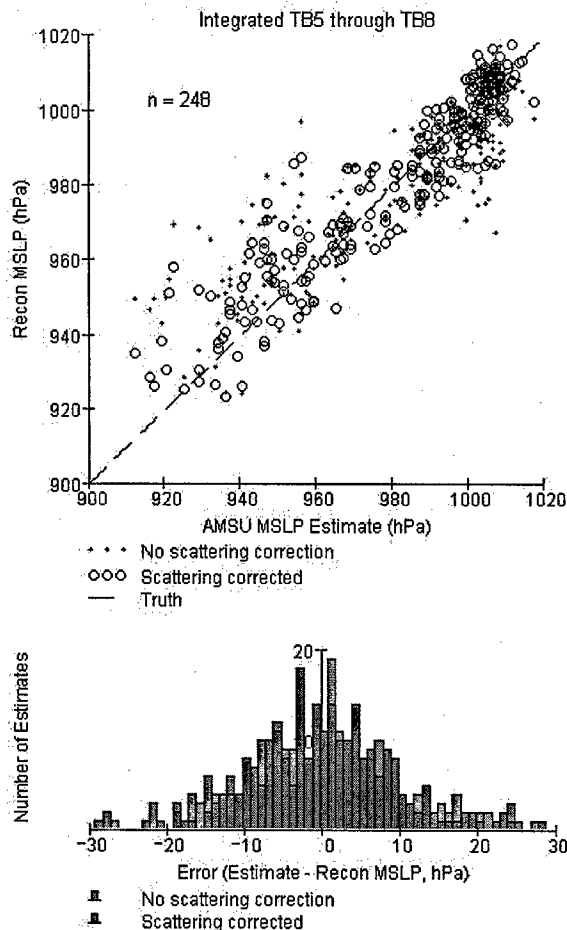


Figure 6.5: Precipitation correction improvement in a TC intensity estimation technique using a vertically-integrated *TB* anomaly employing channels 5 through 8.

Most significantly, this correction method is the most physical of the methods employed to date. Velden and Smith (1983), Velden (1989), and Velden et al. (1991) manually removed FOV's that qualitatively appeared to be precipitation-affected. Spencer and Braswell (2001) included precipitation-sensitive channels as multiple-regression predictors, but this method does not enable a true determination of the unaffected  $TB$  gradient, the true physical link to  $V_{max}$ . Demuth et al. (2004) employ the most physical method to date, using AMSU cloud liquid water and cloud ice water correlation with reduced tropospheric sounding channel  $TB$ . But as discussed in Chapter 3, Li and Weng (2002) point out that this type of correction is effective mostly for the lower-tropospheric sounding channels ( $TB4$  and  $TB5$ ). DeMuth et al. (2004) are left to correct the upper-tropospheric sounding channels by smoothing the Laplacian of the  $TB$  field when they detect an anomalously cold  $TB$ . The problem here is that a warm anomaly FOV, which is still warmer than its surroundings, but not as warm as it should be in the absence of precipitation scattering, will not be corrected.

The precipitation correction method here uses AMSU channels insensitive to tropospheric temperature to quantify precipitation effects on sounding channel  $TB$ 's, then corrects those  $TB$ 's before applying them to a TC intensity algorithm. As a result, this technique can be applied to any chosen algorithm relating sounding  $TB$  to TC MSLP, and even other similar instruments.

## 7. Conclusions and Future Work

### 7.1. Summary

Hurricanes are significant natural disasters, so it's important to forecast their impacts correctly for both civil society and military operations. Forecasting TC impacts requires accuracy in forecasting TC track, TC maximum sustained winds, and the TC wind distribution. Recently TC track forecasting has improved significantly, while intensity forecasting has stagnated because the processes governing it are still poorly understood or not resolvable by existing NWP models. The best forecast tools are statistical, relying on current TC intensity and intensity trend. In situ TC intensity obs are very rare, so the bulk of intensity measurements are remotely-sensed by satellite. The mainstay Dvorak technique, which uses visible and IR geostationary imagery, can be subjective, labor intensive, and constrained by rules that limit its ability to respond to rapid storm changes. Complimenting this remote sensing technique with one that is more physical and objective would benefit forecasters. In this spirit, microwave temperature sounding instruments have been used for nearly 30 years to estimate TC *MSLP* by measuring warm anomaly in upper-tropospheric *TB* above storm center. Until the AMSU instrument, this wasn't feasible operationally because of poor instrument resolution and data refresh rates. Today CIMSS' AMSU technique performs on a par with the Dvorak technique, but still suffers from uncertainty, part of which is due to scattering by hydrometeors in eyewall or spiral band convection. This study used theory and observational data to develop an empirical correction to reduction in tropospheric sounding channel brightness temperatures (*TB*'s) caused by scattering.

Chapter 3 showed that AMSU-A's low frequency window channels were sensitive to relative humidity changes and rain emission. High frequency channels were subject to rain emission, but also scattering by large liquid and frozen hydrometeors, especially graupel. Because the atmosphere is transparent in the window bands between  $O_2$  and water vapor absorption lines, these channels are sensitive to emission/scattering caused by the total optical depth of hydrometeors throughout the depth of the troposphere, while sounding channels are only sensitive to hydrometeors impinging the channel's weighting function. Nevertheless, a simple 1-d plane-parallel conceptual model showed that window channel  $TB$  perturbations caused by a rain and ice layer correlated with  $\Delta TB$  in an upper-tropospheric sounding channel.

Chapter 4 employed a unique, polarized reverse Monte Carlo radiative transfer model, coupled with prescribed profiles of temperature, pressure, humidity, cloud liquid, rain, snow, and graupel (some based on Petty 1-d rain model; some obtained from a fine-scale model simulation of 1998's Hurricane Bonnie) to verify under more realistic conditions the utility of the high-frequency window  $TB$ 's for correcting sounding channel  $TB$ 's. AMSU-A channel 2  $TB$  was found to be a good predictor of high-frequency window channels ( $TB15$  and  $TB17$ ) in the absence of scattering. The depression of high-frequency  $TB$ 's from their modeled no-scattering values correlated well with depression in tropospheric temperature sounding channels. Individual high-frequency channels, particularly AMSU-B moisture channels, performed as well as the first principal component of the channel ensemble.

Chapter 5 analyzed four days of N15, N16, and N17 AMSU data over oceans between  $15^\circ S$  and  $15^\circ N$  latitude. Using this data, and a compilation of 125 TC scenes from 2003, an empirical prediction for no-scatter  $TB15$  through  $TB20$   $TB$ 's using  $TB2$  was developed. The

depression from the predicted no-scatter high-frequency  $TB$  values was correlated with sounding channel  $TB$  depressions. The slope relating window and sounding channel  $\Delta TB$ , however, was found to be stronger within 100 km of a TC center. Two possible explanations are offered, both centered on difference between convective clouds in the inter-tropical convergence zone (ITCZ), where the slopes were derived versus in the TC eyewall or inner rainbands. The first is based on Cecil's (2002) finding that eyewall and rainband convection produce greater radar reflectivity aloft than ITCZ convection. Since both types of convection start from similar near-saturated surface parcels at approximately the same temperature as the sea surface, there may not be much vertically-integrated ice or water content difference between the two types, and so little window-channel  $TB$  difference, but the greater reflectivity aloft indicates hydrometeors are lifted higher in eyewall convection, causing greater effects on upper-tropospheric temperature sounding channels.

The second explanation is based on the different ambient thermodynamic environment of the two settings. The warming in an ITCZ hot tower interior competes against scattering to influence microwave  $TB$ , reducing the scattering effect. Eyewall convection is occurring in a warm, saturated environment and is mostly mechanically driven. So scattering is free to reduce the microwave  $TB$  without interference from warming within cloud. Both processes might be both at work simultaneously. The net result is that for a given high-frequency  $TB$  depression, hydrometeors in a TC eyewall or inner spiral band are more effective at reducing sounding channel  $TB$ . Empirical scattering corrections, using different slopes near TC center vs. at larger radii, were tested, and  $TB15$  was found to perform best in reducing the scatter between channel 7 and 8 warm anomaly magnitude and TC  $MSLP$ .

In chapter 6, an  $n = 497$  sample of AMSU overflights of TC's between 1998 and 2004 was used to validate the performance of the scattering correction when applied to the current CIMSS TC intensity technique. Limb-corrected sounding channel *TB*'s were first corrected for scattering using the empirical method developed in Chapter 5. Applying this correction improved CIMSS algorithm RMSE and average mean error by about 10%. Part of the reason for the modest improvement is the CIMSS algorithm's strong dependence on the *TB8* warm anomaly, which (at 150 hPa) is largely immune from scattering effects. Additionally, the algorithm is already indirectly correcting for scattering through its size bias correction. At small storm sizes, sub-sampling reduces the AMSU field of view's sensitivity to the warming present. At the same time more convection is occurring (since strong storms tend to be smaller) near the center and weakening observed *TB* anomaly. Both effects reduce the observed warm anomaly, so correcting for the observed weak bias for small storms corrects for scattering at the same time that it corrects for sub-sampling.

Correcting all tropospheric sounding channels for precipitation effects improves the lower channels' accuracy to the extent that a vertically-averaged *TB* anomaly now performs on a par with single-channel *TB7* or *TB8* and may do a better job of fully sampling the deep-layer thermal anomaly in future intensity techniques.

## **7.2. Future Work: Adaptation to SSMIS**

The next generation of operational temperature sounding instrument, the Special Sensor Microwave Imager/Sounder (SSMIS) was launched in Fall 2003 and is currently completing its calibration/validation period. This instrument combines the conical scan geometry and high

resolution of the earlier SSMI instrument, with the temperature and moisture sounding channels of the AMSU instrument.

SSMIS' conical scan geometry will benefit TC intensity estimation because limb-correction and variable field-of-view sizes across a scan line will no longer be sources of error. Its higher resolution (37 km vs. 48 to 150 km for AMSU-A) will help to reduce sub-sampling problems.

But SSMIS has potential to be more vulnerable to scattering. Its suite of temperature sounding channels includes equivalents to AMSU-A's channel 6 and channel 8, but not channel 7. Channel 8 is the ideal MSLP estimation channel for AMSU, since it is relatively immune from precipitation effects while retaining sensitivity to the TC warm anomaly. The key, though, is that at large scan angles, where temperature sounding channel weighting functions move to higher levels due to limb darkening, AMSU has channel 7 available to blend with channel 8 via limb correction, and keep the limb-corrected channel 8 sensitive to 150 hPa temperature across the full scan. SSMIS' scan angle is fixed at  $45^\circ$ , where its channel 8 weighting function will peak significantly higher than 150 hPa. Its next-lower channel is equivalent to AMSU-A channel 6, whose weighting function peaks at approximately 250 hPa at  $45^\circ$  scan angle. This is approximately the level to which AMSU's limb-corrected channel 7 is sensitive and precipitation effects are much more pronounced than they are at 150 hPa.

This means that SSMIS will likely rely on its channel 6 equivalent to estimate TC intensity, and will need scattering correction to achieve accuracy equivalent to the AMSU-based technique. Fortunately, SSMIS also has low- and high-frequency window channels similar to AMSU. The precipitation correction technique developed in this study--temperature sounding

channel correction via depression of a high-frequency window channel from its low-frequency derived no-scatter predicted value--will be directly applicable, and potentially more vital to producing useful TC intensities using this future generation of instrument.

## **Appendix: A Polarized Reverse Monte Carlo Radiative Transfer Model**

### **A.1. Motivation**

This appendix describes in detail the polarized reverse Monte Carlo (RMC) radiative transfer model (RTM) used to accomplish the simulation study in Chapter 4. The purpose of that chapter was to determine whether scattering-induced depression in high-frequency Advanced Microwave Sounding Unit (AMSU) brightness temperatures (TB) could be used to quantify scattering effects on AMSU temperature sounding *TB*. This was accomplished using an ensemble of 19 one-dimensional profiles with known temperature, moisture, cloud liquid, rain, snow, and graupel. Nine of those profiles were prescribed using a 1-D model developed by Petty (2001a). The remaining ten were obtained from a Mesoscale Model 5 (MM5) simulation of Hurricane Bonnie (1998). By comparing modeled TB's at AMSU frequencies and scan geometries with precipitation included and removed, the precipitation effect on each channel was determined for use in developing an empirical scattering correction.

The requirement for the study, then, was an RTM that was flexible enough to allow different forms of meteorological variable inputs, would easily allow changes or removal of individual moisture or precipitation components to isolate their effects, would run quickly enough to allow multiple cases to be completed relatively quickly, would allow a number of different types of output. A large number of existing radiative transfer codes exist in widespread use, but each would require considerable time to learn and adapt to this purpose. Additionally, the author wanted to avoid depending results from a "black box," of whose inner workings he had limited understanding. Finally, future work with this model will include adaptation to 3-D inhomogeneous scenes. Other radiative transfer methods--two-stream, successive orders of

scattering, discrete ordinates--are not readily adaptable to geometries other than 1-D plane-parallel. Only Monte Carlo methods, as described in section A.2, are well-suited for this geometry. Other Monte Carlo microwave radiative transfer codes have been developed, but all are developed with the Special Sensor Microwave Imager (SSM/I) in mind and are limited to the special cases of vertical, horizontal, or no polarization, and fixed scan angles. For these reasons, the author opted to develop a new RMC RTM able to handle the large number of AMSU-A and -B scan angles, frequencies, and polarizations, accept different types of meteorological profiles, allow easy exclusion of some or all precipitation constituents, and readily adaptable to 3-D geometry.

## A.2. Previous Monte Carlo Models

Petty (1994, 1994a) was the first to introduce RMC techniques to the application of microwave radiative transfer in the atmosphere. He described how a photon (or packet of photons) traveling from an emitting source, through a scattering medium, to a sensor could be just as easily traced backward along the same path from sensor to emitter. The reciprocity theorem allows the same scattering phase function that predicts the probability of a forward-traveling photon scattering into a given direction to be used for determining the probability that a backward-traveling photon was scattered *from* a given direction. Random numbers are used: 1) in conjunction with the local extinction coefficient to generate a photon's path length between extinction events; and 2) to determine the direction of scattering when a scattering event occurs. Petty gave each photon an initial weight (visualized as a probability of continuing to exist) and removed a fraction of the weight equal to  $(1 - \omega)$  at each extinction event. This continues for the

photon through numerous scattering events until its weight is reduced below some threshold (at which point it is considered totally absorbed) or it leaves the domain. At each point where a photon encounters extinction, the probability density it sheds in the event is accumulated at that point. After all the photon packets have been exhausted, the relative weight at each point in the 3-D domain determines how much the physical temperature at that point contributes to the *T<sub>B</sub>* observed by the sensor. Petty handled polarization by treating each photon packet as permanently polarized, either vertically or horizontally, and using the appropriate polarized reflectivity upon encountering the ocean surface. Necessary inputs to the model are 3-d domains of temperature, extinction coefficient, single-scatter albedo, and asymmetry parameter.

Petty used his results to demonstrate the feasibility of RMC methods for predicting realistic microwave *T<sub>B</sub>*'s in highly inhomogeneous 3-D domains. He also noted two phenomena that would be impossible to model in plane-parallel geometry: First, a significant *T<sub>B</sub>* contribution comes from warm rain emission observed from the sides of clouds, reducing the scattering impact of the ice layer in the top of the cloud, which would always be encountered if plane-parallel geometry was used. Second, ocean-surface reflection of warm rain emission can contribute significantly--and increase--the observed *T<sub>B</sub>*.

Roberti et al. (1994) also developed a RMC technique at about the same time, and present a detailed discussion of their technique. Liu (1996) developed a novel polarization treatment in his backward-forward Monte Carlo (BFMC) model. He traced photons backward unpolarized to their emission sources, then forward through the same scattering points, as a pair of photons, one vertically polarized and one horizontal. At each scattering event, he used a rotated phase matrix, which would produce different intensities for the vertically and horizontally polarized incident

photons, to account for non-isotropic scattering. The end-state polarization for the photon was determined from the ratio of the vertical/horizontal pair's intensities. Roberti and Kummerow (1999) concluded, instead, that rigorous polarization in a Monte Carlo model is only possible in the forward direction. Kim et al. (2004) compared various radiative transfer methods, using an RMC technique as the accuracy benchmark.

### A.3. Key Assumptions and Approximations

Several assumptions influence the results from this RMC implementation. First, the assumed form of the liquid and frozen precipitation size distribution determines how a given precipitation density affects the Mie properties of the medium. This model uses the Marshall-Palmer (MP) distribution for rain and graupel, modified per Petty (2001a) to account for fall-speed variation with density, and its effect on relating precipitation density to rain rate. The Sekhon-Srivastava (SS) distribution is used for snow, with the exponential decay parameter,  $\Lambda(R)$  scaled by  $2^{-2}$ , to produce more realistic snow size distributions, again per Petty (2001a).

The composition of graupel will affect its Mie parameters strongly, by changing its complex refractive index, as well as its geometric size. For the study in Chapter 4 were obtained following Petty's methodology: above the freezing level, graupel is 70% air and 30% ice. When it falls below the freezing level, it melts smoothly over 0.5 km of descent, with its water fraction increasing linearly from 0% to 100% with the remainder composed of the 70% air-30% ice mixture. The complex refractive index for all cases is computed using the Bruggeman formula:

$$f_1 \frac{\epsilon_1 - \epsilon_{av}}{\epsilon_1 + 2\epsilon_{av}} + (1 - f_1) \frac{\epsilon_2 - \epsilon_{av}}{\epsilon_2 + 2\epsilon_{av}} = 0$$

where  $\epsilon_1$  and  $\epsilon_2$  are the dielectric constants of two mixed substances,  $f_1$  is the fraction of the first substance, and  $\epsilon_{av}$  is the dielectric constant of the mixture (Bohren and Huffman 1983; Petty 2004). For melting graupel,  $\epsilon_{av}$  for the air-ice mixture is again averaged, this time with the appropriate fraction of water.

Mie theory, of course, introduces a very important assumption--spherical particles. Aerodynamic forces make falling raindrops oblate and give them a preferred orientation and riming and accretion of frozen particles may produce pronounced asymmetries. Treatment of such non-spherical particles and their preferred orientations is problematic, and well beyond the scope of this study, but it needs to be noted as a source of uncertainty.

Finally, polarization is handled in a limited fashion in this implementation. Photons are initialized with a linear polarization matching the polarization angle of the sensor, which rotates with scan angle. A rigorous treatment of polarization would require using the Mie properties at each grid point to compute the 4x4 Mueller matrix elements (Section 3.1), then using that matrix to determine the probability of an incident polarized photon scattering in any direction, and the polarization it would assume at each direction. The scattered direction would then be chosen randomly according to the directional probability distribution. This is computationally prohibitive, particularly in 3 dimensions.

Instead, photons are limited to linear polarization. At each level in the 1-dimensional domain, Mie theory is used to compute the upper-left diagonal elements of the Mueller matrix. The scattered intensity is then computed for each scattering angle,  $\theta$ . This is repeated after rotating the incident photon through  $0^\circ$  to  $90^\circ$  about the incident direction. The result is a two-dimensional array of scattered intensities for all combinations of scattering angle and rotation

angle. This array is stored for each frequency, channel, and model grid point before beginning the RMC radiative transfer.

When a photon is scattered by the RMC model, the scattering direction is randomly chosen using the stored probability density function. The incident and scattering directions together form the plane of scattering, and the incident photon's polarization state is computed relative to this plane, and preserved after it is scattered. A rigorous treatment of scattering, by use of the full Mueller matrix would allow obliquely polarized incident photons to produce elliptically polarized scattered photons and vice versa (via the lower-right corner Mueller matrix elements). This treatment of scattering ignores that aspect. However, the scattered polarization state is of third order importance; of first order is whether scattering occurs at all, determined together by the extinction coefficient and single-scatter albedo, while the asymmetry parameter (operating through a phase function approximation or embodied in the truncated Mueller matrix used here) assumes second-order importance by determining the angular distribution of scattering energy.

#### **A.4. Methodology**

The model implemented for the work accomplished in Chapter 4 contains five separate modules:

##### ***A.4.1. Meteorological Profile Generation***

The first module generates the temperature, pressure, and air, water vapor, cloud liquid, rain, snow, and graupel density for each 1-D level. Drop size spectra are computed using the modified MP and SS formulas for user-defined precipitation size (liquid mass-equivalent sizes

for snow and graupel) bins. Two versions of this module were written. The first replicates Petty's (2001a) 1-d parametric cloud model for a regularly-spaced vertical grid of user-defined spacing. This version generates precipitation rates for each precipitation species at each level; the MP and SS distributions are used directly to compute size spectra. The second version reads a binary MM5 model output file and produces output at the irregularly-spaced heights of the sigma levels. The MM5 uses a bulk microphysics scheme, so its precipitation output is a mass density for rain, snow, and graupel at each grid point. These are converted to rain rate, using fall speed to relate the two quantities, enabling particle size spectra computation via the MP and SS distributions. In both cases, output is stored in text format for use by succeeding modules. The profiles in Figures 4.1a, .2a, .3a, .5a, and .6a were generated by this module.

#### A.4.2. Mie Property Generation

The user controls the instrument characteristics--frequencies, sidebands, polarizations, and scan angles--used by this module. It uses these to compute complex refractive indices for rain, snow (modeled as a solid ice sphere), and each unique composition of graupel present (using the Bruggeman mixing formula) for each instrument frequency. Next, using the Mie solution as outlined in Bohren and Huffman (1983) Chapter 4, the module computes extinction and

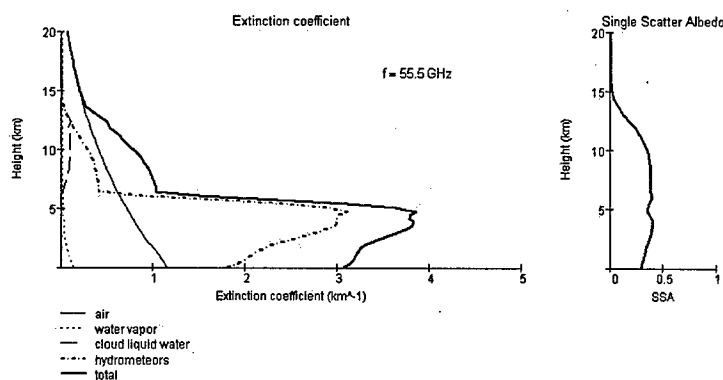


Figure A.1: Example extinction coefficient (left) and single-scatter albedo (right) profiles for AMSU-A channel 8 for the profile from Chapter 4 case 9 (Figure 4.3a). Each constituent's contribution to total extinction (bold line) is included.

scattering cross-sections and efficiencies, and Mueller matrix precursor coefficients used in module 4 for phase function generation for each instrument frequency and model level. Output arrays are stored in text format for use by the next two modules. Figures 3.1 through 3.3 were created using output from this module.

#### A.4.3. Extinction Profile Generation

This module uses the extinction and scattering coefficients to compute the extinction coefficient and single scatter albedo for each instrument frequency and model level. The Rosenkranz (1998) model is used for dry air and water vapor absorption. Cloud water absorption

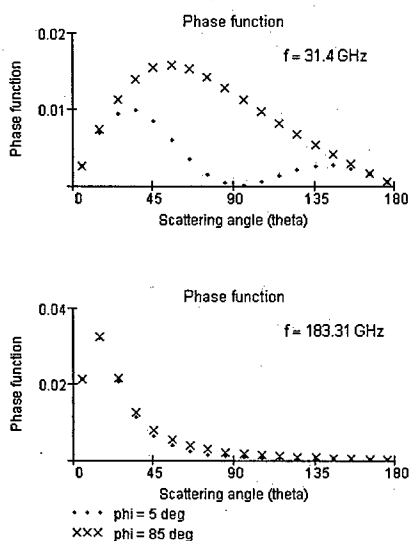


Figure A.2: Example phase function for AMSU-A channel 2 (top) and AMSU-B channel 18 (bottom) for a model level with large graupel content (and hence a large asymmetry parameter). Dots are for a photon polarized nearly vertically ( $5^\circ$ ) with respect to the scattering plane; crosses are for a photon polarized nearly horizontally ( $85^\circ$ ).

is computed using the Liebe et al. (1991) model. Cloud ice absorption and scattering in the microwave spectrum is negligible and is ignored. At each vertical level, the total extinction and scattering coefficients are computed by summing each size bin's extinction or scattering coefficient, weighted by its number density. After computing a layer's total absorption (dry air + water vapor + cloud liquid + rain + snow + graupel) and total scattering (rain + snow + graupel), the bulk single-scatter albedo follows.

#### A.4.4. Phase Function Generation

This module uses stored S1 and S2 coefficients for each instrument frequency and model level (see Bohren and Huffman 1983 Section 4.4.4) from the Mie

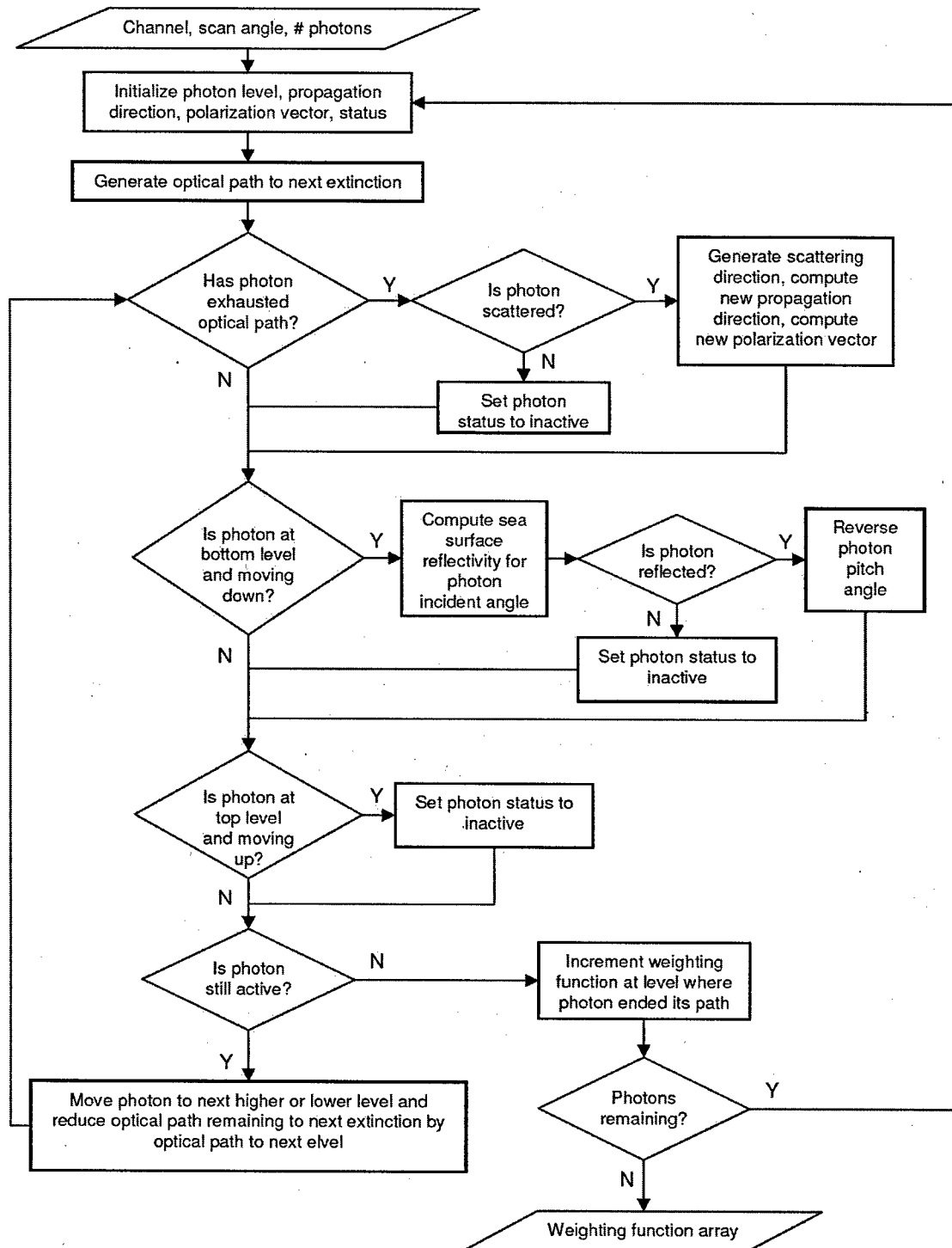


Figure A.3: Flowchart for reverse Monte Carlo radiative transfer model.

property module. In a manner similar to that used to compute bulk extinction and scattering efficiencies, it computes *effective* S1 and S2 from each precipitation size bin's number-density-weighted value. From the effective S1 and S2, the upper-left corner Mueller matrix elements follow. These are used, as described in Section A.3, with an incident unit-intensity photon rotated through all rotation angles to build the two-dimensional scattering direction probability distribution. For each scattering angle and rotation angle bin, the scattered intensity (weighted by the solid angle subtended by the bin's angular limits) is computed and normalized. Each solid angle bin, then, contains a value relating the scattered intensity in that bin to the incident intensity, or equivalently, the probability of the incident photon scattering into that bin. This scattering direction distribution array is stored as a text file for each instrument channel and model level. Figure A.2 shows an example scattering probability as a function of scattering angle,  $\theta$ , for rotation angles of  $5^\circ$  and  $85^\circ$ .

#### ***A.4.5. Reverse Monte Carlo Radiative Transfer***

The final module reads the temperature, extinction efficiency, single-scatter albedo, and scattering direction probability density, then performs the RMC radiative transfer for a user-specified subset of instrument channels and scan angles, and number of photons. Results are depicted graphically and output in text format. Figure A.3 is a flowchart outlining the RMC code.

#### **A.5. Future Work**

As discussed in Section A.3, several assumptions are inherent in the design of the RMC model. Several of these--the assumed particle size distributions, the spherical geometry inherent

to Mie theory, the graupel composition, and the dielectric mixing formula--are well beyond the scope of this work and are limitations affecting nearly all radiative transfer models.

One assumption, though, can be improved by further work: the treatment of polarization. While a full implementation of the Mueller matrix would be computationally prohibitive for a large 3-dimensional domain, a parameterization of individual matrix elements in terms of precipitation density may be possible. This would enable construction of the matrix elements via a look-up table instead of Mie calculations at each grid point. The photon's full polarization state, expressed via the Stokes vector, would then be tracked through the photon's path to its emission point. If the photon encounters the surface, the Fresnell scattering matrix would be employed. The underlying assumption of reciprocity remains in place, allowing the Mueller matrix to be used for scattering interchangeably in the forward and backward directions.

The results from Chapter 4 demonstrate the validity and utility of this version of RMC radiative transfer model, and the author looks forward to further developing it and employing it for additional applications in the future.

## References

- Alliss, R.J., G.D. Sandlin, S.W. Chang, and S. Raman, 1993: Applications of SSM/I Data in the Analysis of Hurricane Florence (1988). *J. Appl. Met.*, 32, 1581-1591.
- Atkinson, G.D., and C.R. Holliday, 1977: Tropical Cyclone Minimum Sea Level Pressure/Maximum Sustained Wind Relationship for the Western North Pacific. *Mon. Wea. Rev.*, 105, 421-427.
- Bauer, P., 2001: Over-Ocean Rainfall Retrieval from Multisensor Data of the Tropical Rainfall Measuring Mission. Part I: Design and Evaluation of Inversion Databases. *J. Atm. Ocn. Tech.*, 18: 1315-1330.
- Bauer, P., and A. Mugnai, 2003: Precipitation Profile Retrievals Using Temperature-Sounding Microwave Observations. *J. Geophys. Res.*, 108, 4730.
- Bennartz, R., 2000: Optimal Convolution of AMSU-B to AMSU-A. *J. Atm. and Ocn. Tech.*, 17, 1215-1225.
- Bennartz, R., and G.W. Petty, 2001: The Sensitivity of Microwave Remote Sensing Observations of Precipitation to Ice Particle Size Distributions. *J. Appl. Met.*, 40, 345-364.
- Bennartz, R., A. Thoss, A. Dybbrow, and D.B. Michelson, 2002: Precipitation Analysis Using the Advanced Microwave Sounding Unit in Support of Nowcasting Applications. *Met. Appl.*, 9, 177-189.
- Bennartz, R., and P. Bauer, 2003: Sensitivity of Microwave Radiances at 85-183 GHz to Precipitating Ice Particles. *Rad. Sci.*, 38, 8075.
- Bohren, C.F., and D.R. Huffman, 1983: Absorption and Scattering of Light by Small Particles. New York, Wiley, 530pp.
- Brueske, K.F., 2001: Satellite-Based Tropical Cyclone Intensity Estimation Using NOAA-KLM Series Advanced Microwave Sounding Unit (AMSU) Data. Ph.D. Dissertation, University of Wisconsin-Madison, 92pp.
- Brueske, K.F., and C.S. Velden, 2003: Satellite-Based Tropical Cyclone Intensity Estimation Using the NOAA-KLM Series Advanced Microwave Sounding Unit (AMSU). *Mon. Wea. Rev.*, 131(4), 687-697.
- Burns, B.A., X. Wu, and G.R. Diak, 1997: Effects of Precipitation and Cloud Ice on Brightness Temperatures in AMSU Moisture Channels. *IEEE Trans. Geosci. and Rmt. Sensing*, 35, 1429-1437.
- Cecil, D.J., 2002: Reflectivity, Ice Scattering, and Lightning Characteristics of Hurricane Eyewalls and Rainbands. Part I: Quantitative Description. *Mon. Wea. Rev.*, 130, 769-784.
- Chahine, M.T., 1970: Inverse Problems in Radiative Transfer: Determination of Atmospheric Parameters. *J. Atm. Sci.*, 27, 960-967.

- Chen, F.W., and D.H. Staelin, 2003: AIRS/AMSU/HSB Precipitation Estimates. *IEEE Trans. Geosci. Rmt. Sensing*, 41, 410-417.
- DeMaria, M., and J. Kaplan, 1999: An Updated Statistical Hurricane Intensity Prediction Scheme (SHIPS) for the Atlantic and Eastern North Pacific Basins. *Wea. and Fcstg.*, 14, 326-337.
- Demuth, J.L., M. DeMaria, J.A. Knaff, and T.H. Vonder Haar, 2004: Evaluation of Advanced Microwave Sounding Unit Tropical-Cyclone Intensity and Size Estimation Algorithms. *J. Appl. Met.*, 43, 282-296.
- Draine, B.T., and P.J. Flatau, 1994: Discrete-Dipole Approximation for Scattering Calculations. *J. Opt. Soc. Am.*, 11, 1491-1499.
- Dumas, J., and R. Tibbetts, 2004: Invited Presentations by Tropical Cyclone Warning Users. *United States Pacific Command Tropical Cyclone Conference*, Tokyo, Japan, 17-19 Feb 2004.
- Dvorak, V.F., 1973: A Technique for the Analysis and Forecasting of Tropical Cyclone Intensity from Satellite Pictures. NOAA Technical Memorandum NESS 45, 19pp.
- Dvorak, V.F., 1975: Tropical Cyclone Intensity Analysis and Forecasting from Satellite Imagery. *Mon. Wea. Rev.*, 103, 420-430.
- Dvorak, V.F., 1984: Tropical Cyclone Intensity Analysis Using Satellite Data. NOAA Technical Report NESDIS 11, 45pp.
- Emanuel, K.A., 1986: An Air-Sea Interaction Theory for Tropical Cyclones. Part I: Steady-State Maintenance. *J. Atm. Sci.*, 43, 585-604.
- Emanuel, K.A., 1988: Toward a General Theory of Hurricanes. *Amer. Scientist*, 76, 371-379.
- Emanuel, K.A., 2003: Tropical Cyclones. *Annu. Rev. Earth Planet. Sci.*, 31, 75-104.
- Ferraro, R.R., F. Weng, N.C. Grody, and L. Zhao, 2000: Precipitation Characteristics Over Land from the NOAA-15 AMSU Sensor. *Geophys. Res. Ltrs.*, 17, 2669-2672.
- Frank, W.M., 1977: The Structure and Energetics of the Tropical Cyclone I. Storm Structure. *Mon. Wea. Rev.*, 105, 1119-1135.
- Franklin, J.L., 2005: 2004 National Hurricane Center Forecast Verification Report. NOAA/NWS/NCEP Tropical Prediction Center, 46 pp.
- Gasiewski, A.J., 1993: Microwave Radiative Transfer in Hydrometeors. *Atmospheric Remote Sensing by Microwave Radiometry*, M.A. Janssen, ed. New York: Wiley, 572pp.
- Goldberg, M.D., 1999: Generation of Retrieval Products from AMSU-A: Methodology and Validation. *Preprints: 10th International TOVS Working Group*, 27 Jan-2 Feb 1999, Boulder, CO, 219-229.
- Goldberg, M.D., D.S. Crosby, and L. Zhou, 2001: The Limb Adjustment of AMSU-A Observations: Methodology and Validation. *J. Appl. Met.*, 40, 70-83.

- Grody, N.C., 1976: Remote Sensing of Atmospheric Water Content From Satellite Using Microwave Radiometry. *IEEE Trans. Ant. Prop.*, AP24, 155-162.
- Grody, N.C., 1991: Classification of Snow Cover and Precipitation Using the Special Sensor Microwave Imager. *J. Geophys. Res.*, 96, 7423-7435.
- Grody, N.C., 1993: Remote Sensing of the Atmosphere From Satellites Using Microwave Radiometry. *Atmospheric Remote Sensing by Microwave Radiometry*, M.A. Janssen, ed. New York: Wiley, 572pp.
- Grody, N.C., 1999: Application of AMSU for Obtaining Water Vapor, Cloud Liquid Water, Precipitation, Snow Cover, and Sea Ice Concentration. *Preprints: 10th International TOVS Working Group*, 27 Jan-2 Feb 1999, Boulder, CO, 230-240.
- Herndon, D.C., C. Velden, K. Brueske, R. Wacker, and B. Kabat, 2004: Upgrades to the UW-CIMSS AMSU-Based TC Intensity Estimation Algorithm. *Preprints: AMS 26th Conference on Hurricanes and Tropical Meteorology*, 3-7 May 2004, Miami, FL, 118-119.
- Hock, T.F., and J.L. Franklin, 1999: The NCAR GPS Dropwindsonde. *Bull. Amer. Met. Soc.*, 80, 407-420.
- Holland, G.J., 1980: An Analytic Model of the Wind and Pressure Profiles in Hurricanes. *Mon. Wea. Rev.*, 108, 1212-1218.
- Joint Typhoon Warning Center, 2005: 2004 Annual Tropical Cyclone Report. Naval Pacific Meteorology and Oceanography Center, 827 pp.
- Kabat, B.W., 2002: A Satellite-Based Multi-Channel Approach to Tropical Cyclone Intensity Estimation Using the AMSU Passive Microwave Sensor. M.S. Thesis, University of Wisconsin-Madison, 63pp.
- Katsaros, K.B., E.B. Forde, P. Chang, and W.T. Liu, 2001: QuikSCAT's SeaWinds Facilitates Early Identification of Tropical Depressions in 1999 Hurricane Season. *Geophys. Res. Ltrs.*, 28, 1043-1046.
- Kidder, S.Q., W.M. Gray, and T.H. Vonder Haar, 1978: Estimating Tropical Cyclone Central Pressure and Outer Winds from Satellite Microwave Data. *Mon. Wea. Rev.*, 106, 1458-1464.
- Kidder, S.Q., 1980: Tropical Cyclone Outer Surface Winds Derived from Satellite Microwave Sounder Data. *Mon. Wea. Rev.*, 108, 144-152.
- Kidder, S.Q., and T.H. Vonder Haar, 1995: *Satellite Meteorology*. San Diego, Academic, 466pp.
- Kim, M., G.M. Skofronick-Jackson, and J.A. Weinman, 2004: Intercomparison of Millimeter-Wave Radiative Transfer Models. *IEEE Trans. on Geosci. and Rmt. Sensing*, 42, 1882-1890.

- Knaff, J.A., M. DeMaria, C.R. Sampson, and J.M. Gross, 2003: Statistical, 5-Day Tropical Cyclone Intensity Forecasts Derived from Climatology and Persistence. *Wea. and Fcstg.*, 18, 80-92.
- Kummerow, C., 1993: On the Accuracy of the Eddington Approximation for Radiative Transfer in the Microwave Frequencies. *J. Geophys. Res.*, 98, 2757-2765.
- Kummerow, C., W.S. Olson, and L. Giglio, 1996: A Simplified Scheme for Obtaining Precipitation and Vertical Hydrometeor Profiles from Passive Microwave Sensors. *IEEE Trans. on Geosci. and Rmt Sensing*, 34, 1213-1232.
- Lander, M.A., 1994: An Exploratory Analysis of the Relationship Between Tropical Storm Formation in the Western North Pacific and ENSO. *Mon. Wea. Rev.*, 122, 636-651.
- Leary, C.A., and R.A. Houze, 1979: The Structure and Evolution of Convection in a Tropical Cloud Cluster. *J. Atm. Sci.*, 36, 437-457.
- Leary, C.A., 1979: Melting and Evaporation of Hydrometeors in Precipitation from the Anvil Clouds of Deep Tropical Convection. *J. Atm. Sci.*, 36, 669-679.
- Le Seur, N.E., and H.F. Hawkins, 1963: An Analysis of Hurricane Cleo (1958) Based on Data from Research Reconnaissance Aircraft. *Mon. Wea. Rev.*, 91, 694-709.
- Li, X., and F. Weng, 2002: Correction of Cloud Contamination on AMSU Measurements. *Proceedings: 12th International TOVS Study Conference, 27 Feb-5 Mar 2002, Lorne, Australia.*
- Liebe, H.J., G.A. Hufford, and T. Manabe, 1991: A Model for the Complex Permittivity of Water at Frequencies Below 1 THz. *Int. J. IR and MM Waves*, 12, 659-675.
- Liou, K.N., 2002: *An Introduction to Atmospheric Radiation*. San Diego, Academic, 583pp.
- Liu, G., and J.A. Curry, 1992: Retrieval of Precipitation From Satellite Microwave Measurement Using Both Emission and Scattering. *J. Geophys. Res.*, 97, 9959-9974.
- Liu, Q., C. Simmer, and E. Ruprecht, 1996: Three-Dimensional Radiative Transfer Effects of Clouds in the Microwave Spectral Range. *J. Geophys. Res.*, 101, 4289-4298.
- Martin, J.D., and W.M. Gray, 1993: Tropical Cyclone Observation and Forecasting With and Without Aircraft Reconnaissance. *Wea. and Fcstg.*, 8, 519-522.
- Merrill, R.T., 1995: Simulations of Physical Retrieval of Tropical Cyclone Thermal Structure Using 55-GHz Band Passive Microwave Observations from Polar-Orbiting Satellites. *J. App. Met.*, 34, 773-787.
- Mo, T., 1999: AMSU-A Antenna Pattern Corrections. *IEEE Trans. on Geosci. and Rmt. Sensing*, 37, 103-112.
- Mugnai, A., H.J. Cooper, E.A. Smith, and G.J. Tripoli, 1990: Simulation of Microwave Brightness Temperatures of an Evolving Hailstorm at SSM/I Frequencies. *Bull. Amer. Met. Soc.*, 71, 2-13.

- Mugnai, A., E.A. Smith, and G.J. Tripoli, 1993: Foundations for Statistical-Physical Precipitation Retrieval from Passive Microwave Satellite Measurements. Part II: Emission-Source and Generalized Weighting-Function Properties of a Time-dependent Cloud-Radiation Model. *J. Appl. Met.*, 32, 17-39.
- Nakazawa, T., 2001: Suppressed Tropical Cyclone Formation Over the Western North Pacific in 1998. *J. Met. Soc. Japan*, 79, 173-183.
- National Oceanographic and Atmospheric Administration National Environmental Satellite Data and Information Service (NOAA/NESDIS), 2000: *NOAA-KLM User's Guide*. G. Goodrum, K.B. Kidwell, and W. Winston, eds. <http://www2.ncdc.noaa.gov/docs/klm/>.
- Oguchi, T., 1983: Electromagnetic Wave Propagation and Scattering in Rain and Other Hydrometeors. *Proc. IEEE*, 71, 1029-1078.
- Olander, T.L., C.S. Velden, and J.P. Kossin, 2004: The Advanced Objective Dvorak Technique (AODT): Latest Upgrades and Future Directions. *Preprints: AMS 26th Conference on Hurricanes and Tropical Meteorology*, 3-7 May 2004, Miami, FL, 294-295.
- Ooyama, K.V., 1982: Conceptual Evolution of the Theory and Modeling of the Tropical Cyclone. *J. Met. Soc. Japan*, 60, 369-379.
- Panegrossi, G., S. Dietrich, F.S. Marzano, A. Mugnai, E.A. Smith, X. Xiang, G.J. Tripoli, P.K. Wang, and J.P.V. Poiars Baptista, 1998: Use of Cloud Microphysics for Passive Microwave-Based Precipitation Retrieval: Significance of Consistency Between Model and Measured Manifolds. *J. Atm. Sci.*, 55, 1644-1673.
- Panegrossi, G., 2004: Validation of Microphysics Parameterization in Cloud Resolving Models Using Passive Microwave Measurements. Ph.D. Dissertation, University of Wisconsin-Madison, 186pp.
- Petty, G.W., 1994: Physical Retrievals of Over-Ocean Rain Rate from Multichannel Microwave Imagery. Part I: Theoretical Characteristics of Normalized Polarization and Scattering Indices. *Met. and Atm. Phys.*, 54, 79-99.
- Petty, G.W., 1994a: Physical Retrievals of Over-Ocean Rain Rate from Multichannel Microwave Imagery. Part II: Algorithm Implementation. *Met. and Atm. Phys.*, 54, 101-121.
- Petty, G.W., 1994b: Reverse Monte Carlo Simulations of Microwave Radiative Transfer in Realistic 3-d Rain Clouds. *Preprints: AMS 7th Conference on Satellite Meteorology and Oceanography*, 6-10 Jun 1994, Monterey, CA, 185-188.
- Petty, G.W., 2001: Physical and Microwave Radiative Properties of Precipitating Clouds. Part I: Principal Component Analysis of Observed Multichannel Microwave Radiances in Tropical Stratiform Rainfall. *J. Appl. Met.*, 40, 2105-2114.
- Petty, G.W., 2001a: Physical and Microwave Radiative Properties of Precipitating Clouds. Part II: A Parametric 1D Rain-Cloud Model for Use in Microwave Radiative Transfer Simulations. *J. Appl. Met.*, 40, 2115-2129.
- Petty, G.W., 2004: *A First Course in Atmospheric Radiation*. Madison, Sundog, 444pp.

- Pielke, R.A., and C.W. Landsea, 1998: Normalized Hurricane Damages in the United States, 1925-1995. *Wea. and Forecasting*, 13, 621-631.
- Poe, G., K. St. Germain, S. Swadley, J. Wessel, B. Thomas, and J. Bohlson, 2002: Air Force/Navy SSMIS Cal/Val Plan. *Defense Meteorological Satellite Program MAXI Review*, 29-31 Oct 2002, Silver Spring, MD.
- Rappaport, E.N., 1993: Preliminary Report: Hurricane Andrew, 16-28 August 1992. National Hurricane Center, 38 pp.
- Reale, A.L., 2001: NOAA Operational Sounding Products From Advanced-TIROS Polar Orbiting Environmental Satellites. NOAA Technical Report NESDIS 102, 59pp.
- Roberti, L., J. Hafferman, and C. Kummerow, 1994: Microwave Radiative Transfer Through Horizontally Inhomogeneous Precipitating Clouds. *J. Geophys. Res.*, 99, 16707-16718.
- Roberti, L., and C. Kummerow, 1999: Monte Carlo Calculations of Polarized Microwave Radiation Emerging from Cloud Structures. *J. Geophys. Res.*, 104, 2093-2104.
- Rodgers, C.D., 1976: Retrieval of Atmospheric Temperature and Composition From Remote Measurements of Thermal Radiation. *Rev. of Geophys. and Space Phys.*, 14, 609-624.
- Rosenkranz, P.W., 1993: Absorption of Microwaves by Atmospheric Gases. *Atmospheric Remote Sensing by Microwave Radiometry*, M.A. Janssen, ed. New York: Wiley, 572pp.
- Rosenkranz, P.W., 1998: Water Vapor Microwave Continuum Absorption: A Comparison of Measurements and Models. *Rad. Sci.*, 33, 919-928.
- Simpson, J., E. Ritchie, G.J. Holland, J. Halverson, and S. Stewart, 1997: Mesoscale Interactions in Tropical Cyclone Genesis. *Mon. Wea. Rev.*, 125, 2643-2661.
- Simpson, J., J.B. Halverson, B.S. Ferrier, W.A. Petersen, R.H. Simpson, R. Blakeslee, and S.L. Durden, 1998: On the Role of "Hot Towers" in Tropical Cyclone Formation. *Meteor. Atmos. Phys.*, 67, 15-35.
- Smith, E.A., 1994: Design of an Inversion-Based Precipitation Profile Retrieval Algorithm Using an Explicit Cloud Model for Initial Guess Microphysics. *Met. and Atm. Phys.*, 54, 53-78.
- Smith, W.L., 1970: Iterative Solution of the Radiative Transfer Equation for Temperature and Absorbing Gas Profile of an Atmosphere. *Appl. Optics*, 9, 1993-1999.
- Spencer, R.W., 1986: A Satellite Passive 37-GHz Scattering-based Method for Measuring Oceanic Rain Rates. *J. Clim. Appl. Met.*, 25, 754-766.
- Spencer, R.W., and W.D. Braswell, 2001: Atlantic Tropical Cyclone Monitoring with AMSU-A: Estimation of Maximum Sustained Wind Speeds. *Mon. Wea. Rev.*, 129, 1518-1532.
- Tripoli, G.J., 1992: An Explicit Three-Dimensional Nonhydrostatic Numerical Simulation of a Tropical Cyclone. *Met. Atm. Phys.*, 49, 229-254.
- United States Pacific Command, 2002: USCINCPAC Instruction 3140.1X: Tropical Cyclone Operations Manual, 49pp.

- Van Burgel, J.L., 1999: The Study of Tropical Cyclones Using Satellite Microwave Data. M.S. Thesis, Curtin University of Technology, 122pp.
- Velden, C.S., 1982: *Monitoring Tropical Cyclone Evolution with NOAA Satellite Microwave Observations*. M.S. Thesis, University of Wisconsin-Madison, 1982.
- Velden, C.S., and W.L. Smith, 1983: Monitoring Tropical Cyclone Evolution with NOAA Satellite Microwave Observations. *J. Appl. Met.*, 22, 714-724.
- Velden, C.S., W.L. Smith, and M. Mayfield, 1984: Applications of VAS and TOVS to Tropical Cyclones. *Bull. Amer. Met. Soc.*, 65, 1059-1067.
- Velden, C.S., 1989: Observational Analyses of North Atlantic Tropical Cyclones from NOAA Polar-Orbiting Satellite Microwave Data. *J. Appl. Met.*, 28, 59-70.
- Velden, C.S., B.M. Goodman, and R.T. Merrill, 1991: Western North Pacific Tropical Cyclone Intensity Estimation from NOAA Polar-Orbiting Satellite Microwave Data. *Mon. Wea. Rev.*, 119, 159-168.
- Velden, C.S., T.L. Olander, and R.M. Zehr, 1998: Development of an Objective Scheme to Estimate Tropical Cyclone Intensity from Digital Geostationary Satellite Infrared Imagery. *Wea. and Fcstg.*, 13, 172-186.
- Weatherford, C.L., and W.M. Gray, 1988: Typhoon Structure as Revealed by Aircraft Reconnaissance. Part I: Data Analysis and Climatology. *Mon. Wea. Rev.*, 116, 1032-1043.
- Weatherford, C.L., 1988: Typhoon Structure as Revealed by Aircraft Reconnaissance. Part II: Structural Variability. *Mon. Wea. Rev.*, 116, 1044-1056.
- Weng, F., L. Zhao, R.R. Ferraro, G. Poe, X. Li, and N.C. Grody, 2003: Advanced Microwave Sounding Unit Cloud and Precipitation Algorithms. *Rad. Sci.*, 38(4), MAR33-1 - MAR33-13.
- Whitehead, J.C., 2000: One Million Dollars a Mile? The Opportunity Costs of Hurricane Evacuation. Working Papers, East Carolina University Department of Economics, 35 pp.
- Wilheit, T.T., A.T.C. Chang, M.S.V. Rao, E.B. Rodgers, and J.S. Theon, 1977: A Satellite Technique for Quantitatively Mapping Rainfall Rates over the Oceans. *J. Appl. Met.*, 16, 551-560.
- Willoughby, H.E., 1998: Tropical Cyclone Eye Thermodynamics. *Mon. Wea. Rev.*, 126, 3053-3067.
- World Meteorological Organization Tropical Cyclone Programme, 2000: Twenty Years of Progress and Achievement of the WMO Tropical Cyclone Programme (1980-1999). WMO/TD-No. 1039, 46 pp.
- Wu, R., and J.A. Weinman, 1984: Microwave Radiances from Precipitating Clouds Containing Aspherical Ice, Combined Phase, and Liquid Hydrometeors. *J. Geophys. Res.*, 89, 7170-7178.

- Yueh, S.H., B.W. Stiles, and W.T. Liu, 2003: QuikSCAT Wind Retrievals for Tropical Cyclones. *IEEE Trans. on Geosci. and Remote Sensing*, 41, 2616-2628.
- Zhu, T., D.L. Zhang, and F. Weng, 2002: Impact of the Advanced Microwave Sounding Unit Measurements on Hurricane Prediction. *Mon. Wea. Rev.*, 130, 2416-2432.
- Zipser, E.J., 1969: The Role of Organized Unsaturated Convective Downdrafts in the Structure and Rapid Decay of an Equatorial Disturbance. *J. Appl. Met.*, 8, 799-814.